TAMPEREEN TEKNILLINEN YLIOPISTO
TAMPERE UNIVERSITY OF TECHNOLOGY

Erkka Saukko

Studies of the Physical Phase State of Aerosol Nanoparticles

Julkaisu 1308 • Publication 1308

Tampere 2015

Tampereen teknillinen yliopisto. Julkaisu 1308
Tampere University of Technology. Publication 1308

Erkka Saukko

Studies of the Physical Phase State of Aerosol Nanoparticles

Thesis for the degree of Doctor of Science in Technology to be presented with due permission for public examination and criticism in Sähkötalo Building, Auditorium S2, at Tampere University of Technology, on the 26th of June 2015, at 12 noon.

Tampereen teknillinen yliopisto - Tampere University of Technology
Tampere 2015

Doctoral candidate: Erkka Saukko, M.Sc.
Aerosol Physics Laboratory
Department of Physics
Tampere University of Technology

Supervisors: Jorma Keskinen, prof.
Aerosol Physics Laboratory
Department of Physics
Tampere University of Technology

Annele Virtanen, prof.
Department of Applied Physics
University of Eastern Finland

Pre-examiners: Merete Bilde, prof.
Department of Chemistry
Aarhus University

Martin Gysel, Ph.D.
Laboratory of Atmospheric Chemistry
Paul Scherrer Institute

Opponent: Gordon McFiggans, prof.
School of Earth, Atmospheric and Environmental Sciences
The University of Manchester

ISBN 978-952-15-3544-4 (printed)
ISBN 978-952-15-3608-3 (PDF)
ISSN 1459-2045

ABSTRACT

Aerosol particles produced in the atmosphere have major effects on the life on Earth: cloud formation starts on seed particles, often formed by photochemical oxidation of biogenic volatile organic compounds; visibility, corrosion, and health problems are caused by anthropogenic hydrocarbon and sulfur emission processed into particles by the atmosphere and the sun.

Naturally occurring secondary organic aerosol (SOA) particles can produce up to a half of the non-refractory mass of aerosol particles of less than micrometer in size (Jimenez et al., 2009). This makes SOA a large contributing factor to the climate system of the Earth. The actual effect that these particles have is, however, not well known, compared to the other effects affecting the climate (Myhre et al., 2013). The research effort to increase the understanding and reduce the uncertainties around the climate effects of SOA encompasses an interdisciplinary research community.

The recent advance made by the observation of a solid phase of SOA by Virtanen et al. (2010) was the starting point for this thesis. The solid phase of SOA particles means that a long-held assumption of a partition equilibrium between the condensed phase and the gas phase of the semivolatile species may be wrong and produce too low a timescale for the particle chemical reaction rates and uptake coefficients.

This work consists of new developments in the instrumentation of particle properties as well as new observations of laboratory-generated secondary organic aerosol. The method development has two branches, one concentrates on finding more information from the measurement signal of an electrical low pressure impactor (ELPI) used in a somewhat unconventional way, whereas the other consists of a new detection method for particle bounce and response to different humidity and phase hysteresis induced by a carefully controlled humidity history.

The methods and observations made during this work are by no means the final word on the subject, but they are being used and further developed by the scientific community. Study of the particle phase and bounce as well as SOA mechanical properties and kinetics is well underway, and its results will be used to further refine the understanding of both aerosol fundamentals as well as the climate system.

PREFACE

This thesis is the result of years of persistent and sometimes stubborn work. It would have been impossible for me to achieve it by myself, let alone keep believing that it can be done. I am grateful to my supervisors, professors Jorma Keskinen and Annele Virtanen, for letting me work at the group of talents and giving me as much responsibility as I could bear. Special thanks to Annele for organizing the research visit of a lifetime, which proved to be the key factor for this thesis.

I thank everyone at the Aerosol Physics Laboratory for a pleasant work environment. Help, humor and friendship, combined with constructive criticism have been abounding.

I express my gratitude to all of the co-authors of the publications included: your expert input made the science possible. Heino Kuuluvainen and Anssi Arffman are acknowledged for sharing their wisdom of the impactors, among other things. Dr. Andrew Lambe is acknowledged for providing the outstanding expertise in laboratory work related to SOA and other aerosol production. Dr. Paola Massoli is acknowledged for AMS measurements and analysis as well as general organization. Thanks to Dr. MacKenzie Smith, Assistant Professor Mikinori Kuwata and Dr. Soeren Zorn for making the smog chamber measurements possible.

I thank Dr. Doug Worsnop, professors Paul Davidovits, Thomas Koop and Scot Martin for the opportunity and organization of the research visits in Boston.

I am grateful to Professor Merete Bilde and Dr. Martin Gysel for pre-examining the thesis and providing valuable insights and improvements. Financial support from Maj and Tor Nessling foundation is acknowledged.

I thank my friends and my family for the support that started long before this work. Finally, I thank my wife for all the help and support and believing in me more than I do.

Tampere, May 2015

Erkka Saukko

Contents

SYMBOLS AND ABBREVIATIONS

α	Material coefficient of bouncing
β	charge equalization coefficient of bouncing
λ	Mean free path of a gas molecule, 66 nm at NTP
ν	Frequency of electromagnetic radiation
η	Dynamic viscosity
χ	Particle shape factor
ρ	Density
ρ_0	Reference density, $1000\,kg/m^3$
A	Hamaker constant
AMS	Aerosol mass spectrometer
AS	Ammonium sulfate, $(NH_4)_2SO_4$
B	normalized material coefficient of bouncing
BF	Bounced fraction, not to be mixed with bounce factor
C_c	Slip correction factor
CCN	Cloud condensation nuclei
CPC	Condensation particle counter
C_R	Coefficient of restitution
$d_{50,n}$	Cut-off size for the impactor stage n
$v_{50,n}$	Impact velocity of the cut-off size.
d_a	Particle aerodynamic diameter
d	Particle diameter, for round particles also the mobility diameter
e	elementary charge
ELPI	Electrical low pressure impactor
F_D	Drag force
g	Gravitational acceleration
GF	Growth factor
h	Planck constant
H/C	Hydrogen to carbon ratio
HEC	Harvard Environmental Chamber
HONO	Nitrous acid
I	Electric current
k_B	Boltzmann constant
LG	Levoglucosan
LLPS	Liquid-liquid phase separation
MFC	Mass flow controller
n	Charge number

$(NH_4)_2SO_4$	Ammonium sulfate
NTP	Normal temperature and pressure, 10^5 Pa, 273.15 K
O/C	Oxygen to carbon −ratio
O(1 D)	Free oxygen radical
O_3	Ozone
$^*OH$	Hydroxyl radical
$\overline{OS_C}$	Oxidation state
P	penetration probability of a particle through charger
PAM	Potential aerosol mass reactor
PTFE	Teflon, polytetrafluoroethylene
q_0	Particle precharge before contact
q_c	Charge transfer upon impaction
q_{tot}	Total charge transfer
r	Effective radius of a diffusing particle
RH	Relative humidity
RH_I	Relative humidity in the impactor
SOA	Secondary organic aerosol
SOM	Secondary organic material
SMPS	Scanning mobility particle sizer
T	Temperature
UV	Ultraviolet radiation
V	Particle velocity
v_i	Impaction velocity
$v_{i,0}$	reference impaction velocity, 100 m/s
v_i^*	Critical impaction velocity
v_r	Rebound velocity
z_0	Atomic separation between particle and substrate (0.4 nm)
Z	Electrical mobility

List of publications

Paper 1 A. Virtanen, J. Kannosto, H. Kuuluvainen, A. Arffman, J. Joutsensaari, E. Saukko, L. Hao, P. Yli-Pirilä, P. Tiitta, J. K. Holopainen, J. Keskinen, D. R. Worsnop, J. N. Smith, and A. Laaksonen. Bounce behavior of freshly nucleated biogenic secondary organic aerosol particles. *Atmospheric Chemistry and Physics*, 11(16):8759–8766, 2011.

Paper 2 H. Kuuluvainen, A. Arffman, E. Saukko, A. Virtanen, and J. Keskinen. A new method for characterizing the bounce and charge transfer properties of nanoparticles. *Journal of Aerosol Science*, 55:104–115, 2013.

Paper 3 E. Saukko, H. Kuuluvainen, and A. Virtanen. A method to resolve the phase state of aerosol particles. *Atmospheric Measurement Techniques*, 5(1):259–265, 2012.

Paper 4 E. Saukko, A. T. Lambe, P. Massoli, T. Koop, J. P. Wright, D. R. Croasdale, D. A. Pedernera, T. B. Onasch, A. Laaksonen, P. Davidovits, D. R. Worsnop and A. Virtanen. Humidity-dependent phase state of SOA particles from biogenic and anthropogenic precursors. *Atmospheric Chemistry and Physics*, 12(16):7517–7529, 2012.

Paper 5 E. Saukko, S. Zorn, M. Kuwata, J. Keskinen and A. Virtanen. Phase state and deliquescence hysteresis of ammonium sulfate seeded secondary organic aerosol *Aerosol Science and Technology*, 49:531–-537, 2015.

Author's contribution

The publications constituting the scientific output of this thesis are results of a wide collaboration and group effort. The author's role is specified as follows:

Paper 1: The author participated in the planning and implementation of the experiments and in the writing process with a minor role. The lead author assumed the main responsibility for the planning, measurements and writing the paper.

Paper 2: The author participated in the development of the methods, designing of the experiments, and assisting with the measurements. The author participated in the writing process, while the lead author assumed the main responsibility of experiments and writing the paper.

Paper 3: The author participated in conceiving the leading idea. The author carried out the planning, construction and testing of the new device. The author performed the experimental part of the publication and assumed most of the responsibility for writing the publication.

Paper 4: The author planned and carried out the bounced fraction measurements and shared the main responsibility for writing equally with the last author of the publication.

Paper 5: The author planned and carried out the bounced fraction measurements and assumed the main responsibility for writing the publication.

1 Introduction

Aerosol particles formed or released in the atmosphere have different lifespans depending on their size, composition, temperature, humidity and weather (Hallquist et al., 2009). Atmospheric aerosols affect the climate and weather as well as the quality of life of a large fraction of the human population around the world.

Recently, the role of aerosol particles in the climate has been the topic of wide scientific interest. The effect of aerosol particles on the energy balance of the Earth is still the greatest source of uncertainty in the current view of the climate system (Myhre et al., 2013, Ch.8.5). While absorbing particles can induce the melting of snow and ice and local warming, different types of particles increase the amount and albedo of the cloud cover and thus reflect radiation thereby cooling the climate.

Secondary organic aerosol (SOA) is used to refer both to the particles formed from gaseous organic precursors through gas phase chemistry, as well as the particles and the carrier gas and vapors. Secondary organic matter (SOM) refers to the condensed organic matter in particles, to distinguish the material from inorganic matter.

The total effect is still somewhat uncertain because the net effect of any given particle on the energy budget of the planet depends very strongly on local conditions, most critically whether the particle grows large enough, can exist long enough and can enter suitable atmospheric conditions to act as a cloud condensation nucleus (CCN). The main factors affecting the CCN activity are the particle size and composition. A large fraction of the atmospheric aerosol loading is formed via secondary particle formation mechanisms. These mechanisms consist of a process whereby new particulate matter is produced as the gas phase reactions convert gaseous precursors into lower volatility condensable matter. This matter is condensed as particles and continue to react slowly with the oxidants absorbed into the condensed matter. The gas phase reactions generally dominate the reactions over reactions happening in the particulate matter due to the higher concentration of oxidants and more effective mixing.

The traditional understanding of these processes is based on steady state partitioning of the secondary material between the gas phase and the condensed phase. This assumption is based on rapid transport of material in the particle phase, that is, liquid matter. A new approach to the issue was taken by Virtanen et al. (2010), who identified biogenic secondary organic aerosol (SOA) particles as having a solid phase state. This state of the organic matter can significantly change the timescales of chemical processing and water interaction with particles.

The key method in Virtanen et al. (2010) was particle bounce measurement with electrical low pressure impactor (ELPI) (Keskinen et al., 1999). The ELPI is traditionally used such that the bounce of particles is inhibited by suitable substrate material or coating,

while flat substrate can be used for liquid particles. As the SOA particles do bounce, which is seen in the instrument as strong deviation from the conventional size distribution, Virtanen et al. (2010) were able qualitatively distinguish bouncing particles.

The finding of the solid SOA particles was based on a known property of the low pressure impactor measurements, particle bounce. This phenomenon is generally being suppressed by the choice of substrate material and coating. However, based on the assumption of liquid particles these measures were not used, which turned out to be useful for observing the solid phase state.

The fundamental difficulty in aerosol science is the small size of the particles, which leads to indirect measurement methods for different particle properties. Often the properties requiring the most sophisticated and convoluted measurements are those that for macroscopic subjects are trivial, such as size and mass. This thesis describes the development and application of methods to distinguish solid particles from liquid ones.

The techniques developed are applied to secondary organic aerosol (SOA). **Paper 1** applies the method used by Virtanen et al. (2010) but reaches into smaller particle sizes and thus to the early moments of a particle's lifetime. With this new approach, a deeper understanding of phase state measurement is developed with the same electrical measurement method in **Paper 2**. In the second part, a new, direct, quantitative method is developed to measure the bounce and infer the phase state of the particles (**Paper 3**). Finally, the direct method is used to probe into the water interaction, aging, and composition effects on the phase state of single- and multicomponent SOA particles (**Paper 4**, **Paper 5**).

This thesis is arranged as a compilation study. The first part compiles the background and experimental setting of the research, its most important results, and a summary of the combined results. The scientific achievements are described in detail in five original articles, reprinted in the appendices.

Aim and scope

The phase state of secondary organic aerosol particles was for long accepted to be low viscosity liquid, so much so that chemical reactions and water interaction in particles could be treated such that the transport from the gas phase to the particles were the limiting factor (Hallquist et al., 2009). This means that the diffusion of compounds from the surrounding gas is the rate-limiting step in particle chemical aging and water interaction processes.

With the observation of Virtanen et al. (2010), the chemical aging and the role and ubiquity of the solid phase in SOA particles had to be reconsidered. The scientific understanding at the moment – and the lack of it – led to the following seminal questions justifying this work:

- How can the phase state of very small particles be measured?
- What is the phase state of the pure and mixed SOA particles?
- What is the effect of the oxidation state, humidity and history on the phase state of particles?
- Do the different phase states require rethinking SOA behavior and interactions in atmospheric processes?

The aim of this thesis is to find answers to the first three questions by instrument development and laboratory studies and to approach the last question through the answers gained. The first goal of the publications constituting this thesis' scientific contribution is to find methods for measuring the physical properties of particles. After this instrumental step, the developed methods are used to constrain the properties of laboratory-generated particles.

The scope of the work is limited to experimental work on finding and using new methods to study the phase state of single and multicomponent particles and their interaction with the surrounding atmosphere, excluding field work and climate and aerosol interaction modeling.

The experimental studies consist of applying the bounce measurement method developed by Virtanen et al. (2010) and finding new ways of using the original method to extract more information on particle physical and electrical properties from the electrical measurement technique (**Paper 1**, **Paper 2**). An alternative, more direct approach to bounce measurement is developed in **Paper 3**.

From the atmospheric point of view, the observation of solid SOA is studied further with laboratory aerosols to establish whether the observation is a rare instance, or whether the solid phase is ubiquitous in SOA. The limits of the solid phase are studied with respect to SOA water content and the chemical composition of the precursors (**Paper 4**,**Paper 5**) and the effect of crystalline seed particles in SOA (**Paper 5**). The implications of these studies extend to a better understanding of the climate system and cloud formation, but they are beyond the scope of this thesis.

2 Secondary organic aerosol: formation and role in the atmosphere

Atmospheric aerosol can be roughly divided into primary and secondary particles. Primary particles are formed or released into the air by mechanical or physical processes. These processes include sea sprays, wind entrainment, and, for example, pollen release. Secondary particles are formed via gaseous precursor chemical transformation and subsequent condensation. Aerosol emissions from combustion processes are considered primary exhaust, since particle formation after the release of the exhaust is not a result of chemical transformation. The secondary emission, however can be much higher than the currently regulated primary emission (Robinson et al., 2007; Shrivastava et al., 2008). Atmospheric aerosol can thus contain both primary and secondary components because secondary matter can condense on a primary particle, which in this case is called seed.

Secondary organic aerosol is ubiquitous in the atmosphere (Murphy et al., 2006; Jimenez et al., 2009; Zhang et al., 2007). Despite their small size, SOA particles have a substantial effect on the hydrological cycle of the atmosphere as a catalyst for water cloud formation. As the hydrological cycle all but determines the climate of the Earth, the importance of its effect on the climate is of consequence on a global scale. SOA also has direct climate effects Myhre et al. (2013).In addition to biogenic SOA and its global effects, anthropogenic SOA has massive effects on the local scale in the form of air quality and related health effects. Understanding the processes during the life cycle of SOA particles enables effective countermeasures against harmful smog events.

2.1 Formation of SOA particles

The first observation of particles forming in the atmosphere were made at the end of the 19th century by J. Aitken, who pushed atmospheric sciences further than perhaps any other single scientist in the field. The birth of atmospheric aerosol physics is marked by a treatise on the number of particles in different types of air (Aitken, 1889) and later the formation of new particles in the atmosphere (Aitken, 1912).

The formation and growth of secondary organic aerosol starts often with nucleation of small, sulfuric acid containing clusters (Almeida et al., 2013) in the nanometer range, over which the secondary organic matter condenses. These nucleation mode particles, on the order of 10 nm then grow into larger sizes into the accumulation mode, which consists of older particles, over which secondary organic matter is condensed. This accumulation mode resides around 100 nm in diameter Seinfeld and Pandis (1998).

The sources of the secondary organic aerosol mass in the atmosphere are volatile organic compounds, VOCs. VOCs are emitted by vegetation, industry, traffic, biomass burning

and use of fossil hydrocarbon reservoirs (Hallquist et al., 2009). Secondary aerosol formation occurs when gaseous precursors and a source of oxidant meet to react with the result that carbon – carbon bonds are broken and hydrogen is replaced by hydroxyl or other oxygenated functional groups. The main and most efficient oxidation pathway starts with ozone, which in the lower troposphere is produced mainly by solar UV-radiation, the production driven by the $NO-NO_2$ -cycle (Seinfeld and Pandis, 1998):

$$NO_2 + h\nu \longrightarrow NO + O \tag{2.1}$$
$$O + O_2 + M \longrightarrow O_3 + M \tag{2.2}$$
$$O_3 + NO \longrightarrow NO_2 + O_2 \tag{2.3}$$

The steady state of the system is dependent on the UV intensity available to dissociate the nitrogen dioxide.

Hydroxyl radicals are produced by UV-photodissociation reactions of ozone (Seinfeld and Pandis, 1998):

$$O_3 + h\nu \longrightarrow O(^1D) + O_2 \tag{2.4}$$
$$O(^1D) + H_2O \longrightarrow 2\,OH \tag{2.5}$$

The ·OH radical is the most potent oxidant attacking the VOCs during the daytime, although ozone (O_3) is strongly reactive towards double bonds of hydrocarbons(Hallquist et al., 2009; Seinfeld and Pandis, 1998). During nighttime the NO_2 does not photolyze (Equation 2.1), which leads to production of nitrate radical with ozone reaction:

$$NO_2 + O_3 \longrightarrow NO_3 + O_2 \tag{2.6}$$

Secondary aerosol can also be formed from inorganic precursors such as iodine, sulfur dioxide and ammonia. These precursors readily oxidize to form iodine oxides, sulfuric acid and nitrate (Seinfeld and Pandis, 1998).

First or later generation products from the oxidation reactions are then condensed on pre-existing particles or molecular clusters, because their saturation vapor pressure is too low to keep all the products in gaseous form (Sipilä et al., 2010; Ehn et al., 2014). These precursors may, in addition to being of organic origin, be also of inorganic origin. Most commonly, they are organic terpene derivatives released by vegetation. Biogenic secondary organic aerosol formation covers almost all land and some marine areas with SOA forming up to a half of all submicron non-refractory atmospheric aerosol mass (Jimenez et al., 2009).

Typical precursors for SOA formation are terpenes, in the order of increasing number of isoprene units: isoprene, α- and β- pinene and limonene (monoterpenes), longifolene, α-caryophyllene (sesquiterpenes). Larger terpenes exist, but their high molecular mass and thus very low saturation vapor pressure preclude them from being emitted into the gas phase for further atmospheric processing, thus making them unimportant for SOA formation. Conversely, when smaller terpenes are oxidized into heavier molecules, they are readily condensed on seed or larger particles. A schematic presentation of the molecular structures of some relevant terpenes is given in Figure 2.1.

Typical oxidation reactions are the saturation of one of the double bonds of the isoprene unit and the opening of carbon rings in mono- and sesquiterpenes. The main primary

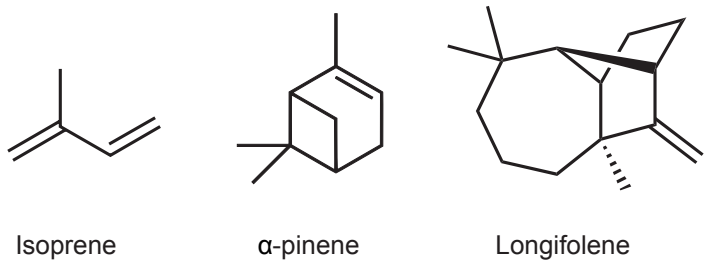

Figure 2.1: Common biogenic terpene precursors for SOA formation. Note the structural reorganization of cyclic components of the larger compounds.

oxidation reactions and sample oxidation products of α-pinene are given in Figure 2.2. The preferential reaction target for ozone is the double bond of the terpene unit, whereas the hydroxyl radical is more ambivalent and can extract hydrogen from an alkane chain (Calogirou et al., 1999; Seinfeld and Pandis, 1998).

In the case of ozone oxidation, the effect can either increase the molecular mass of the precursor compounds or decrease it through dissociative oxidation. In this bond cleavage, ozone oxidation breaks an acyclic molecule in two whereas a cyclic compound just reorganizes, and the mass of the molecule increases (Hunter et al., 2014).

The level of oxidation of organic matter in particles is usually given as the oxygen to carbon ratio (O/C), or the oxidation state ($\overline{OS_C}$) of the organic matter in particles (Kroll et al., 2011). Another commonly used metric is the hydrogen to carbon ratio (H/C), which is a proxy for the saturation state of organic matter. The two ratios are not independent but occupy a area in the Van Krevelen plot, in which most naturally occurring SOM resides and moves while aging in the atmosphere (Heald et al., 2010). The O/C ratio and the $\overline{OS_C}$ are proxies for the aging of organic compounds and are higher, the older the SOA (Jimenez et al., 2009).

Associative oxidation increases the molar mass of SOM compounds. This decreases the saturation vapor pressure and diffusion constant of the molecules. At the same time, increasing polarity, as shown in Figure 2.2, caused by oxygen diminishes the saturation vapor pressure further, because molecules are bound together more easily through Van der Waals forces. The effect on the physical phase state of SOM is increasing viscosity through the increasing interaction between constituent molecules and increasing molecule size.

The nitrate radical (NO_3) can also participate in oxidation, especially during nighttime, when UV radiation is not available for NO_2 dissociation. The oxidation reaction with NO_3 is similar to *OH oxidation. These oxidants can further increase the mass of organic molecules by funtionalization and oligomerization reactions, or decrease by decomposition (Calogirou et al., 1999). As oxidation proceeds, the acidity and polarity of the organic molecule, such as α-pinene oxidation into pinonic acid, increases along with the mass, which decreases the volatility of the substance. This is the driving mechanism of particle formation, which happens as the molecules, now in supersaturation, condense upon small seed particles or clusters and form stable particles. Typical nuclei in atmospheric SOA formation are sulfuric acid and amine clusters together with extremely low volatility organic compounds (Sipilä et al., 2010; Almeida et al., 2013; Kirkby et al., 2011; Ehn

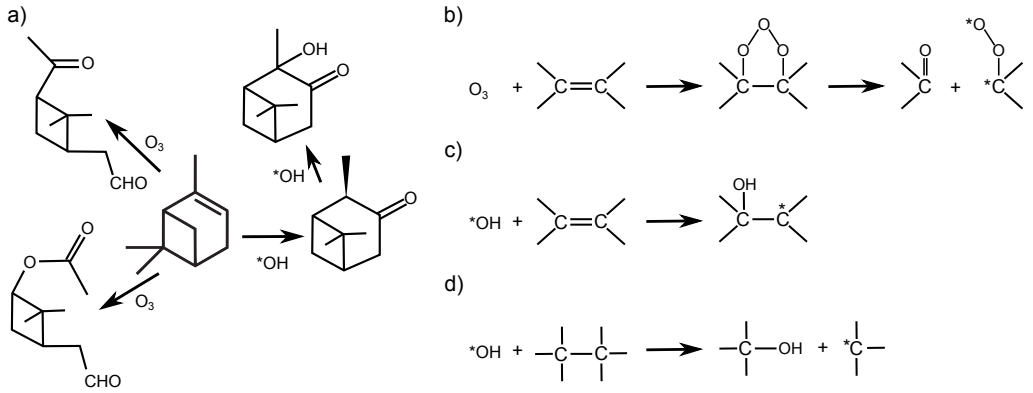

Figure 2.2: a) α-pinene and some of its oxygenated reaction products. Note the change from alkene to more polar as the oxidation is increased. (Calogirou et al., 1999) b) Ozone dissociative oxidation with an alkene chain. c) Associative oxidation of alkene chain by a hydroxyl radical. Note the methyl radical left on the product. d) Alkane oxidation by *OH causes dissociation of acyclic alkanes and ring opening of cyclic alkanes.

et al., 2014). The concentration of sulfuric acid and amines is, however, too small in most places to explain the growth of the particles (Kulmala et al., 2004). Thus most SOA particles are secondary organic matter grown onto existing larger particles such as soot or dust, or small sulfuric acid nucleation mode particles.

The process of α-pinene oxidation and formation of particles is shown schematically in Figure 2.3, where the precursor molecules lose their volatility upon oxidation. The saturation vapor pressure drops with increasing oxidation. The vapors are absorbed into existing particles and when the saturation vapor pressure decreases, the larger the condensed fraction becomes.

The main biogenic precursors are the isoprene (2-methyl-1,3-butadiene, C_5H_8), α-pinene ($C_{10}H_{16}$) and longifolene ($C_{15}H_{24}$) shown in Figure 2.1, which belong to the terpene series, consisting of multiples of the isoprene unit. All the terpenes are emitted into atmosphere by vegetation, α-pinene typically by pines. Seinfeld and Pandis (1998) n-heptadecane ($C_{17}H_{36}$) is a model anthropogenic alkane hydrocarbon precursor. Sulfur dioxide (SO_2) was also used as sulfuric acid precursor.

Test aerosols used in the impactor characterization were ammonium sulfate ($(NH_4)_2SO_4$), sodium chloride (NaCl) and levoglucosan (1,6-Anhydro-beta-glucopyranose, $C_6H_{10}O_5$), of which the two first represent crystalline particles, while levoglucosan is used to test amorphous material behavior instead of SOA. Comprehensive characterization for ammonium sulfate and levoglucosan is given in Mikhailov et al. (2009).

2.2 Particle processes in the atmosphere

After the formation of SOA in the atmosphere, the oxidation of organic matter continues. The compounds are emitted into the gas phase, oxidized and returned to the condensed phase. At the same time oxidants are formed in the gas phase and transported by diffusion to the particle surface and even into the bulk. The reaction rates on the surface and in the bulk are much slower, since the oxidant needs to move first to the surface, where it

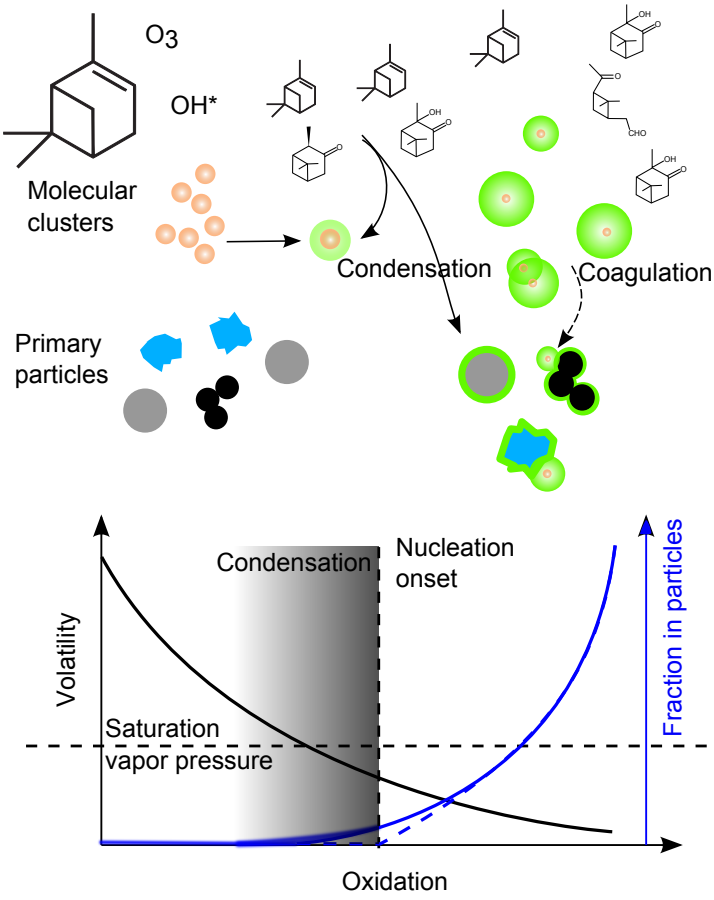

Figure 2.3: Schematic representation of SOA formation and growth through oxidation of α-pinene. The supersaturation of the compounds increases because of the drop in critical vapor pressure as the oxidation continues. If there is no condensation surface, such as existing secondary or primary particles available at the condensation onset, the vapor starts to form new particles at a higher degree of oxidation. In natural environment the sulfuric acid and amines provide condensation seeds in the absence of other particles.

is quickly used and even less is diffused into the bulk of the particle. Even though any oxidant transported to the particle reacts quickly, the oxidation rate of the particle matter as a whole is slow. On the contrary, oligomerization reactions may be more probable, since the likelihood of an organic radical meeting another organic molecule is greatly enhanced in condensed matter. Organic molecules in a highly viscous or even solid matter have virtually no access to the oxidizing species.(Shiraiwa et al., 2011)

Aerosol climate effects are complex and have both cooling and warming components (Myhre et al., 2013, see Figure 8.17). Organic aerosols cool the climate directly by scattering incoming solar radiation. Larger effect, though is the cloud interaction of the particles. There is always a rather large amount of water in the air, readily condensable on a pre-existing particle at a rather modest drop in temperature. This makes the cloud condensation nucleus (CCN) capability of SOA the primary mechanism for climate effects (Andreae and Rosenfeld, 2008). The CCN capability strongly correlates with the particle size, material and water attraction (hygroscopicity) of the particle matter.

A particle forming in the atmosphere has a low probability of acting as a cloud condensation nucleus. Newly formed particles are in danger of getting trapped onto the surface of pre-existing larger particles. Particles can also be oxidized away or removed from the atmosphere by other mechanisms. Even when reaching a suitable size, the cloud condensation process favors the best CCN particles: water preferably goes into large rather than small particles. This is due to the increased effective vapor pressure above a curved surface, the Kelvin effect. The CCN viability of a particle has chemical and physical factors. The chemical composition of the particles determine the hygroscopicity, which sets the minimum particle size of deliquescence and initial particle growth. Of physical factors, particle size determines the early growth rate and threshold through Raoult and Köhler (Seinfeld and Pandis, 1998) mechanisms, a combination of size and equilibrium effects. Water diffusion into a high viscosity particle may lead to diluted surface layer of the particle and thus reduce the particle growth rate. This kinetic effect is inherent for high viscosity materials, such as highly oxidiced organic material. Finally, high concentration of particles mean more competition over the available water, meaning that largest and most hygroscopic particles will act as CCN and once activated keep the interstitial particles in the cloud from absorbing water.

3 Physical properties of aerosol particles

3.1 Fundamental mechanical properties of particles

The most important and obvious aerosol particle property is the particle diameter. Aerosol particles are often too small to measure with contact measurement and usually the population size statistics are more interesting than single particle size. Indirect measurement methods are used to measure particle size and size statistics. Since indirect measurements use different methods, also the particle diameters can differ. The relevant diameters used in this work are the mobility diameter d and aerodynamic diameter d_a. These suffice for treatment of spherical particles. The shape of the particle is taken into account in the calculation by the shape factor χ (Hinds, 1998). In this work, the particles are assumed to be round.

Mobility diameter Stokes' law is derived to describe the response of a rigid sphere to a continuous fluid flow with zero fluid velocity at the particle surface. In its simplest form:

$$F_D = 3\pi\eta V d_m \tag{3.1}$$

where F_D, V, η and d_m are the force needed to sustain the velocity V, the dynamic viscosity of the fluid and the particle mobility diameter, respectively Hinds (1998). At small particle sizes, the mean free path of gas molecules between collisions [1] is of the same scale or smaller than the particle size. With small particles, zero fluid surface velocity ('no-slip') is not met, and Equation 3.1 needs a correction factor called the slip correction factor C_c, defined for the use in this thesis as

$$C_c = 1 + \frac{\lambda}{d}\left[2.34 + 1.05 \cdot exp\left(-0.39\frac{d}{\lambda}\right)\right] \tag{3.2}$$

where λ is the mean free path of the surrounding gas molecules. The corrected Stokes' law is

$$F_D = \frac{3\pi\eta V d}{C_c(d)} \tag{3.3}$$

The mobility diameter can be solved if the force F_D is known. F_D can be gravitational or electrostatic force, for example. In this work the particle selection is done based on their mobility size using electrostatic force of the form

$$F_E = neE \tag{3.4}$$

[1] 66 nm at NTP conditions in air

where the particle is moved by an electrostatic force on the n elementary charges e carried by the particle in the electric field E. The particle will then accelerate, until the drag force is equal to the electrostatic force and the velocity is constant. In practice, this is achieved with a differential mobility analyzer (DMA), which utilizes laminar flow between two coaxial tubes and an orthogonal electric field set by potential difference between the tubes. This arrangement can be used to extract particles of known electrical mobility from the sample. (Hinds, 1998)

Aerodynamic diameter is defined as the diameter of a reference density sphere falling through a gas at the same terminal velocity as the measured particle. Thus the viscous drag force of the air and the mass of the particle are used to define the particle equivalent size. Gas composition, temperature, and pressure affect terminal velocity and the aerodynamic diameter, but generally equivalent terminal velocities are given at normal temperature and pressure (293.15 K and 101325 Pa, before 1982) (IUPAC, 1997). This size depends on the particle shape and density. The density is important because the force for falling velocity depends on the mass of the particle.

When the drag force is set equal to the gravitational force, we get

$$\frac{\pi}{6} d^3 \rho g = \frac{3\pi\eta V d}{C_c(d)} \tag{3.5}$$

And solving for the velocity V

$$V = \frac{C_c(d)\rho d^2 g}{18\eta} \tag{3.6}$$

To calculate the aerodynamic diameter, the unit density particle size for which the velocity is equal to the measured particle is solved from Equation 3.5 by substituting the same velocity for a particle of diameter d_a and solving for d_a:

$$d_a = d\sqrt{\frac{C_c\left(d\right)\rho}{C_c\left(d_a\right)\rho_0}} \tag{3.7}$$

where ρ_0 is the reference density. The slip correction factor renders this equation analytically unsolvable, which calls for iterative solutions and tabulated values for solutions (Hinds, 1998). Further modification arises from the particle shape, which affects the drag force.

A complication with electrostatic measurement is the charge state of particles. A particle needs a charge to be moved for classification, and the amount of the charge must be known.

Charge state of a particle is denoted by the number of surplus elementary charges the particle has, n. Because the charge – particle system behaves like a Boltzmann system, a particle population can be brought into a known charge state distribution by letting the particles into a well-defined charge environment. An often used system is the bipolar neutralizer, which produces an almost symmetrical amounts of negative and positive, weakly charged particles. Increasingly common bipolar charge sources are ultraviolet or x-ray chargers. Another often used system is the unipolar charger, either a diffusion charger with thermal positive or negative ions or field charging with electric field -driven ions. Bipolar chargers typically have much lower mean charge numbers than unipolar chargers due to the recombination of the ions. Hinds (1998).

In addition to charging particles with ions or radiation, the particle charge state can change with mechanical and electrochemical interaction by impacting on a substrate with a different chemical or electrical potential. Dahneke (1971). This charge transfer at impaction is used to study particle mechanical and electrical properties in **Paper 1** and **Paper 2**.

Morphology of a particle, such as its internal structure, is also of interest in addition to the particle external shape. A particle can have a morphology consisting of different phases and materials and thereby affect its apparent physical properties as well as the measured diameter. Particle composition and formation history may dramatically affect particle shape, composition, and structure; for example, SOA formation often produces secondary organic material on sulfate-containing seed (Smith et al., 2012, **Paper 1**),which can either mix with condensing SOM or produce a shelled structure. Another, extreme, example is the formation of fractal-like particles via rapid agglomeration of very high concentration soot particles in a combustion process; the primary particles are well defined and of narrow size distribution, but the rapid agglomeration process turns the particles into lightweight material with the density dependent on the particle size (Maricq and Xu, 2004).

Multicomponent particles can form a shelled structure, if the components are non-miscible. The ordering of he layers can have an effect in the reactivity of the particle, for example a nonpenetrable barrier layer may isolate the inner layer from the surrounding atmosphere.

The material properties of aerosol particles are dominated by their surface. Any interaction with the surroundings is necessarily with or through the surface, and as SOA is generally in the nanometer range, the amount of surface for a given amount of material is so large that it fully dominates the interaction.

However, if the particle is in a reactive environment, the depth of the reactive layer is limited by the rate of transport of the reactive precursors from the surroundings. For liquid particles, this is often not relevant: for example 100 nm liquid particles have characteristic mixing time less than one second (Shiraiwa et al., 2011) and partitioning equilibration timescales less than a minute at mass concentrations above 2 μg Shiraiwa and Seinfeld (2012).

Cappa and Wilson (2011) and Perraud et al. (2012) studied the non-equilibrium nature of the interaction between the gas phase and the condensed phase of secondary organic aerosol. Their experiments showed that the hindered diffusive transport within the particles has a real effect on the partitioning of material between particle and surrounding gas.

Evaporation kinetics experiments of SOA (Vaden et al., 2011) concluded that transport from condensed to gas phase is two orders of magnitude slower than expected with fast equilibrium evaporation models. A direct evaporation aging experiment showed that the flux of material from the particle phase of SOA is constrained by a low diffusion constant in the bulk of the particulate matter.

The material transport and morphology was further investigated with a multicomponent system, for which it was shown that secondary organic material from two different precursors forms at least partially shelled structures and has different evaporation behavior consistent with at least one of the components forming SOA with a semisolid phase (Loza et al., 2013). The effect of phase on diffusive transport, particle structure, and reactivity is

shown schematically in Figure 3.1. There are, however, indications that diffusion limitation in viscous particles is not significant for low saturation vapor pressure compounds. For these very low vapor pressure compounds, more relevant is the kinetic limitation of the gas phase transport (Saleh et al., 2013), however, further heterogeneous processing can still be slowed down by the low diffusion.

From the mechanical point of view, low viscosity corresponds to a high elastic modulus. This means that though measuring diffusion and viscosity in nanoparticles is difficult, mechanical properties may be used as proxies to gain information of the viscosity of the particle matter. This is the crucial reason in this thesis, why particle bounce was measured.

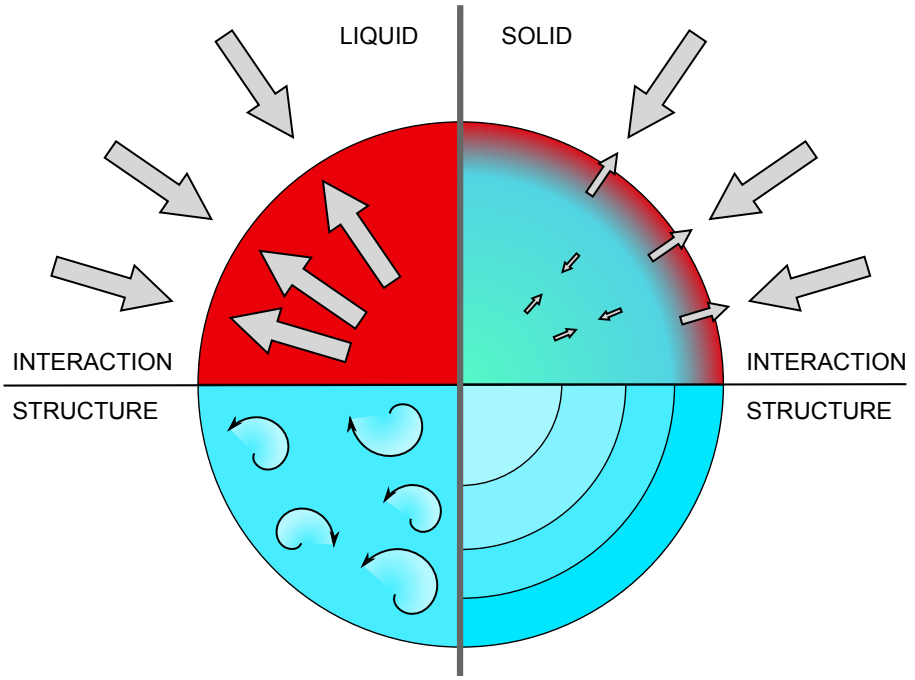

Figure 3.1: Particle interaction with the surrounding gas with liquid and solid particles. Faster diffusion and mixing provide near instantaneous exchange with the surroundings, keeping the particle homogeneous, whereas high viscosity induces lower interaction and structured shells. Through reaction rates and location, diffusion rates affect also the chemistry. Red denotes chemical reactivity.

3.2 Elasticity, viscosity, and diffusion

The diffusion of water, ozone and other chemicals from the gas phase to the bulk of particles is linked to the viscosity of the particles through the Stokes–Einstein equation (Hinds, 1998):

$$D = \frac{k_B T}{6\pi\eta r} \tag{3.8}$$

where D, k_B, T, η and r are the diffusion constant, Boltzmann constant, temperature, viscosity and the effective radius of the diffusing particle or molecule, respectively.

Viscosity is also closely related to the mechanical moduli of matter, especially shear modulus (Vincent, 2012). The shear modulus is defined as the coefficient between a shear stress and strain, whereas diffusion is defined as the coefficient between shear stress and shear rate. However, for crystalline material, a constant shear rate cannot be maintained with a constant stress, and for a liquid, a constant shear strain does not produce any stress. With a slightly different approach of taking into account the time evolution of stress and strain, amorphous or liquid materials can exhibit mechanical stress. This behavior is called viscoelasticity, and it is very common with amorphous materials. The fundamental cause of viscosity and shear modulus is the same: forces between the microscopic constituents of the matter. Viscoelasticity is both a name for the general phenomenon of a mixture of plasticity and elasticity and a specific type time-dependent material response to a stress.

The extreme ranges of the strain modulus can be used to estimate the relevance of discussion about diffusion in the oxidation and water uptake of particles. The simplest form of the idea is that if the particles behave like solids, their diffusion is severely limited such that only the particle surface is reactive, whereas particles of very low viscosity have no kinetic limitations with respect to material transport for chemical reactions. For very large particles there will be kinetic limitations, but these likely stay in the atmosphere for a very short time due to settling.

The viscosity of an amorphous material can vary over ten orders of magnitude when moving from a watery to a glassy state (Zobrist et al., 2008; Shiraiwa et al., 2011). Since the diffusion constant is inversely proportional to viscosity, a similar range in diffusion constants is to be expected with a change from water-activated cloud droplets to dry, glassy particles.

It is intuitive that going from watery droplets to glassy particles means also a change in the mechanical properties of the particles. An explicit connection between elasticity, viscosity, and other properties is, however, elusive, though being actively researched. The study of Dahneke (1971) has been used as a starting point for many efforts to understand the phenomenon of particles bouncing in an impactor.

Bateman et al. (2014) explored the bounce of particles in an impactor apparatus to further expand the notions Dahneke (1971) established for the bounce of supermicron particles. The role of surface effects on the bounce in the case of small particles is greater due to their high surface-to-volume ratio. The adsorption of water on surfaces changes the surface energy of particles and their substrate, which causes also latex and ammonium sulfate particles to change their bounce behavior, not because of the change in elasticity but because of enhanced adhesion. This is a factor that makes calibration between the bounce characteristics and mechanical properties of particles more difficult and prone to an artifact. This behavior is, however, less pronounced with amorphous substances because of water absorption into the bulk matter rather than adsorption.

3.3 Hygroscopicity and hydrophilicity of particles

The interaction between organic compounds in the gaseous and condensed phase affects the lifetime and chemical evolution of SOA. Another important factor for atmospheric implications is water interaction with particles.

The humidity of the particle surroundings affects the physical properties of the particles. When the relative humidity (RH) humidity is increased, water can adsorb on the particle

surface, such particles are called hydrophilic. Alternatively, the water can absorb into the particle bulk, such particles are called hygroscopic. Hygroscopic particles can be dissolved gradually with increasing RH or suddenly at a certain threshold relative humidity, called deliquescence relative humidity (DRH). When the water content in the particle is increased, the physical properties, such as viscosity and elasticity, are changed due to the dissolving and plasticizing effect of the small water molecules.

Crystalline particles usually have a deliquescence–efflorescence hysteresis, while amorphous single component particles exhibit no hysteretic behavior. Crystalline material is typically hydrophilic at low RH and have a distinct DRH at which they deliquesce completely. When drying, dissolved particles with a distinct deliquescence relative humidity also have a typical sudden drying point, called efflorescence relative humidity (ERH), at which the point the particle gives off all the water and forms a crystal again. DRH and ERH are typically quite far from each other (more than 20 %) (Seinfeld and Pandis, 1998). The hysteresis is a result of an energy barrier between the dissolved and dry state of the matter and this energy barrier is a result of a high order and associated well defined low energy configuration, which is difficult to achieve with heterogeneous or large molecule matter.

The level of oxidative aging in organic matter determines its hygroscopicity along with the original chemical composition of the precursors. An addition of polar oxygen atoms increases the polarity and thus the interaction potential between organic molecules and water. Any acidic groups in the molecules also increases the hygroscopicity of particles.

The standard ways of comparing the hygroscopicity of aerosol particles are to measure either the CCN activation threshold of the particles (Roberts and Nenes, 2005) or their growth factor (Rader and McMurry, 1986; Liu et al., 1978). Both methods can be used to parametrize the CCN behavior, but the choice of the method depends on the application. In this thesis the experiments are done at subsaturation levels, so growth factor is the more relevant here.

Bones et al. (2012) studied the uptake and release of water into 3-4 μ m organic particles and concluded that uptake is limited by the slow solubility of SOA material. This is relevant for the CCN activation of particles: if its water uptake is slow compared to the supersaturation depletion in the cloud, the particle is less likely to act as a CCN. This is due to the extreme nonlinearity of the cloud formation process. The first and fastest nuclei to be activated will take up water ever faster as they increase in size due to their higher condensation surface area.

The growth factor (GF) of a particle is measured as the ratio of particle diameters after and before exposure to a humid, usually between 80 and 95 % RH atmosphere. Soluble particles can take up gases, or water vapor in this case, according to Raoult's law, simplified as

$$p = p^o x \tag{3.9}$$

where p is the vapor pressure in the gas phase in case of water and p^o is the pure component vapor pressure and x is the component mole fraction in the solution. This means that if the particle is soluble in water, the effective water partial pressure is lower in particle, even though it is dissolved in water (Seinfeld and Pandis, 1998). As more water is absorbed in the particle, the water is diluted and the system equilibrates. This balance point is measured by the growth factor measurement.

The hygroscopicity tandem DMA (HTDMA) method is often considered the method of greatest finesse because it allows study of very small differences between particles.

With the GF method also hysteresis and other subtle properties of particles can be studied.(Rader and McMurry, 1986; Liu et al., 1978; Mikhailov et al., 2009)

The CCN method aims find the activation supersaturation of the sample particles, and it gives the percentage of particles that grow into actual cloud droplet size at certain supersaturation, often in the range of a few micrometers and above. Since the particle growths beyond the solute effect growth needs condensing water, the condition required for cloud droplet activation is supersaturation, s. Because the range of supersaturation in the atmosphere is very limited, information on cloud formation is very relevant and of direct use for modeling cloud physics (Roberts and Nenes, 2005).

The interaction of water with SOA has the most dramatic effect at the point of water activation of a SOA particle. When the particle has grown by condensation of SOM into a relevant size to act as CCN (dry mobility diameter approximately 100 nm) Hammer et al. (2014), water activation changes the particle from highly concentrated organic matter into a dilute water droplet. This practically releases the kinetic constraints for oxidant transport to the bulk material and this is expected to considerably increase the rate of oxidation. The increased condensation surface and dilute solution also brings additional vapors from gas phase to the solution.

3.4 Phase state of nanoparticles

well-defined phase states of condensed matter are solid and liquid. This distinction hold for crystalline materials. Liquid state has no spatial long term order, while solid, crystalline matter has very high symmetry and order, the crystal structure, which gives the macroscopic rigidity for the solid matter. For amorphous materials there is a continuum of states between solid and liquid, and even glasses have no long term structure. The viscosity of a glass is often defined to be 10^{12} Pa·s, whereas the viscosity of a common liquid, water, is 10^{-3} Pa·s. Semisolid phase state is defined to be in the range of 10^{2} – 10^{12} Pa·s (Shiraiwa et al., 2011). This gives a glassy substance dissolving in water 15 orders of magnitude range of viscosity.

However, for a matter to have a crystalline form, its molecules, atoms, or ions must have a conformational energy minimum, and the molecules must have enough time at the freezing event to move to those locations. Secondary organic material (SOM) is a very complex material. It is typically formed from a mixture of precursors molecules to of a mixture of molecules; each of which can be converted to tens or hundreds of different compounds by the oxidation process. Even though a crystal structure would exist for a large oxidized molecule, the time needed for the arrangement of the sample is not enough, and even a single -component SOM is likely to form amorphous solid. In the case of mixtures, the minimum energy structure is more complex, so it is even more unlikely to form crystals. The analogous solid phase in for amorphous substance is the glassy phase. Glass is often defined by the glass transition, which has characteristic exponential viscosity increase and freezing of the molecular diffusion Zobrist et al. (2008).

Atmospheric SOA particles are usually a mixture of compounds and these mixtures may have mixed or separate phases. SOM condensing over a crystalline seed particle has separate phases, but when deliquesced, the phases can become miscible and upon efflorescence either separate again or remain mixed (Smith et al., 2011, 2012; Bertram et al., 2011). The particle morphology in mixed cases can be a shelled structure, with the surface energies between the (liquid) phases determining the shell order. SOM condensation on dry seed results in a SOM shell, but deliquescence and possible phase

mixing can lose at least part of the formation history. It is also possible to have solid shell over liquid core, or vice versa. This can be achieved by, for example, deliquesced ammonium sulfate seed, and solid alpha-pinene SOA (**Paper 4**.

Amorphous matter has no distinct solidification or melting point but continua of property changes and glass transition temperatures. At a glass transition point, amorphous matter changes from glassy to something softer, yet the transformation does not mean melting of the matter.

The same gradual softening that can happen through a change in temperature can also happen through water uptake and dissolution. Because studying the phase state of nanosized material is rather challenging with traditional methods of materials science, a novel quantitative approach was needed to study SOA.

4 Experimental methods and development work

The main instrumental approaches applied in this work to study the phase state of SOA were different low pressure impactor setups, where either optical (**Paper 3**,**Paper 4**,**Paper 5**) or electrical (**Paper 1**,**Paper 2**) methods were used to detect high viscosity SOA particles using a proxy of particle bounce from a polished impaction substrate. In this thesis, two main approaches were taken to develop the above. The first was an algorithmic method based on a theoretically and experimentally sound background to discern particle bounce and charge transfer based on their behavior in a commercial measurement instrument. The second approach was a direct measurement method to detect particle bounce and use carefully controlled humidity pretreatment of particles to study their phase transitions in detail.

The governing principles of an impactor are shown in Figure 4.1. A two-stage humidity control system was used to study the effect of the humidity and humidity history of the aerosol. With the system the effective humidity of particles at the moment of bounce could be adjusted between 0 and 65 % RH and the maximum humidity up to 95 % RH.

The difference in particle mechanical properties is not as abrupt as the difference in the concepts of solid and liquid, which also causes particle bounce upon impaction to be a process of distributed bouncing and sticking particles. The causes for different bounce probabilities are the distribution of impaction speeds, particle sizes and morphologies, and distributions in the composition and history of temperature and relative humidity. As a consequence, two terms regarding particle bounce probability are defined as *bounced fraction* – particle bounce probability minus the losses of particles caused by their recapture by the impaction substrate (**Paper 3**) and *bounce factor* – the difference in the electrical response of the electrical low pressure impactor compared with a modeled response based on a known particle size distribution measured with the impactor (**Paper 1**).

4.1 Particle impaction

A low pressure impactor is an instrument to separate particles from the aerosol gas phase by aerodynamic separation. This is achieved by highly accelerating the carrier gas of the aerosol with a large pressure difference. The common method is to let the aerosol through a nearly critical orifice, give it near sonic velocity, and provide a perpendicular impaction plate close to the orifice so that the flow turns sharply at the impaction plate. This sharp turn gives the carrier gas a very high acceleration, while particles continue nearly straight line and hit the impaction plate (see e.g. Hinds (1998)) (arrangement is

shown in Figure 4.1). When using a lower pressure, the aerodynamic force is also smaller, which means that at lower pressure it is easier to decrease the cutoff aerodynamic particle size of the impactor. The finite dimensions of the flow and non-ideal flow behavior, such as a turbulence and radial velocity profile within the jet (Arffman et al., 2011, **Paper 2**) cause some particles with the same aerodynamic diameter to reach the substrate and others to avoid it. This causes finite slopes in the collection efficiency curves (see Figure 4.4 for an example of a typical collection efficiency curve).

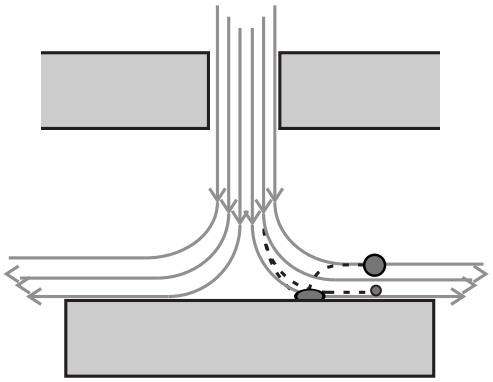

Figure 4.1: A simplified schematic of an impactor. Particles larger than the cutpoint cannot follow the airstream and hit the substrate. Large particles can escape from the impactor if they bounce off the substrate.

4.2 Particle bounce

As the phase state of very small particles of the order of 100 nm is difficult to determine by traditional methods such as optical observation of shape transformation upon stress and differential scanning calorimetry (Höhne et al., 2003), a conceptually simple bounce test is used. The underlying idea is that particles with a high enough elastic modulus compared with viscous losses are able to store the impact energy as elastic deformation and release it into kinetic energy instead of viscous losses (Dahneke, 1971, **Paper 2**). If the stored energy is high enough to overcome the adhesion between particle and substrate, the particle is able to bounce. The term describing the velocity change after adhesion and viscous losses at rebound is defined as the coefficient of restitution:

$$C_R = \frac{v_r}{v_i} \tag{4.1}$$

where v_r and v_i are the rebound and impaction velocities, respectively.

The theoretical work by Dahneke (1971) defines the critical velocity, perpendicular to the surface, v_i^* at which the particle is just able to bounce

$$v_i^* = \frac{\alpha}{d} \tag{4.2}$$

The particle size here re The critical velocity is dependent on the particle mass, size and material constants, which can be formulated in the material coefficient of bouncing (α) (Dahneke, 1971):

$$\alpha = \left(\frac{A\left(1 - C_R^2\right)}{\pi z_0 \rho_p C_R^2} \right)^{1/2} \tag{4.3}$$

where A is the Hamaker constant (Bergström, 1997), z_0 is the atomic separation between particle and substrate[1], and ρ_p is the particle density. More detailed analysis is given in **Paper 2**.

Empirical study by Cheng and Yeh (1979) gives a simplified experimental form of

$$\alpha = \sqrt{\frac{\rho_0}{\rho_p}} B \times 10^{-6} \frac{m^2}{s} \tag{4.4}$$

Where ρ_0 is the reference density of 1000 $\frac{kg}{m^3}$, and B varies from 2.5 to 9.2 depending on the particle and surface materials and the type of impactor. In this form, the experimental coefficient B contains all the material mechanical effects, such as elasticity, viscosity and the particle–substrate interaction for bouncing, whereas the density is normalized out of B.

4.3 Charge transfer

During a brief contact with substrate, particles transfer charge to or from the substrate. The charge transfer during a bounce event can be divided into two independent processes: contact charge separation, depending only on the material properties of particle and substrate, and charge equalization, depending on the previous charge of the particle. The charge on a particle after an impact is given as (John et al., 1980):

$$q_{tot} = q_c + \beta q_0 \tag{4.5}$$

Where q_{tot} is the total charge transfer, q_c the contact charge, q_0 the precharge of the particle before contact and β is precharge sensitivity constant. Charge equalization, βq_0 is assumed, and also shown in **Paper 2** for a good approximation, to be zero.

Contact charge depends on the contact surface area and a change in the dipole moment of the material during compression, in addition to the impact velocity and material properties of the particle and substrate. For dielectric materials, the change in the dipole moment is linearly proportional to size, thus contact charge is proportional to the third power of particle size. Contact charge is also experimentally shown to be proportional to the first power of velocity (John et al., 1980):

$$q_c\left(d, v_i\right) = q_{c,0} \frac{d^3}{d_0^3} \frac{v_i}{v_{i,0}} \tag{4.6}$$

where the reference particle size d_0=100 nm has the impaction velocity $v_{i,0}$ =100 m/s. For further elaboration, see **Paper 2** and John et al. (1980).

4.4 Electrical low pressure impactor

The electrical low pressure impactor (ELPI) (Keskinen et al., 1999) is a cascaded impactor, which measures the electrical current brought to the impactor stages by unipolarly charged particles. The current is used to count the particles deposited in each stage and corrected with the charge state of the particles. When the particles are liquid or sticky, or when the substrates have a bounce –inhibiting vacuum grease layer, the particles are deposited

[1] usually 0.4 nm

on the stages according to their aerodynamic size. The electric charge deposited by the particles onto the impactor is measured in typical applications with sensitive electrometers in the femto- or picoampere range.

Because the particle number is calculated based on the charge they carry, it is of vital importance to bring the aerosol into a well defined, non-net-neutral state. This is done with a corona charger that is characterized for the particle size range of the cascaded impactor. The characteristic curve is called the Pn -curve (Marjamäki et al., 2000). P is the particle penetration through the charger, while n is the mean charge number per particle of a given size. The Pn -curve is the product of the two terms.

The current is measured for each of the stages, and for a backup filter. Each current represents a size bin between the stage's cutpoint and the cutpoint of the previous size (with larger cutoff). The particle size distribution can be calculated from the known charger Pn -curve and the impactor currents when the cut-off sizes are known.

With the simplified form in Equation 4.4, it is possible to have qualitative information about the particle bounce process with the electrical low pressure impactor with particle bounce. When a particle bounces from the impaction substrate at any impaction stage of the ELPI, the impaction velocity is much higher at a subsequent stage. Based on the critical velocity concept, bounce probability at lower stages is thus much higher. The critical velocity is a strict measure, but the distribution in impaction velocities give it a more probabilistic nature in practical impactor applications. Consequently, bouncing particles continue bouncing to the backup filter of the ELPI. When compared to simulated ELPI currents based on the mobility size distribution measured by different methods not susceptible to bounce, a number describing the distortion of the currents, the bounce factor (BF), can be defined as (**Paper 1**):

$$BF = \frac{I_{filter} - I^{id}_{filter}}{\sum I^{id}_{n}} \tag{4.7}$$

where I_{filter} is the measured current on the backup filter, I^{id}_{filter} is the simulated current based on the known size distribution and $\sum I^{id}_{n}$ is the total current to normalize the bounce factor.

This approach is sensitive to any bouncing of particles and can be used to compare different particle materials, but it cannot distinguish differences in particle bounce and charge transfer effects. Thus a low particle bounce probability with a high charge transfer can result in the same bounce factor as a high bounce but a low charge transfer. In theory, particles which give their charge to the first impactor stage and have no further charge transfer upon bounce can be hidden from the method. The sensitivity of the method to bounce is good, however, because large particles have much higher Pn values, leading to very distinct signal at the lower stages and especially at the filter stage. The bounce factor method was first described in Virtanen et al. (2010) and also used in **Paper 1**. It is possible to address the interference from charge transfer on bounce measurements by combining two measurements with different charging state of the aerosol and an independent measurement of the particle size distribution. This has been done in **Paper 2**.

The ELPI is used as the method to impact particles on a substrate in a controlled manner. Impaction velocity in the impactor was calculated by extensive modeling by Arffman et al. (2011), and the results were used to get the last missing piece for the bounce model,

the impaction velocity $v_{i,n}$ of a particle with a size d_a

$$v_{i,n} = v_{j,n} - \frac{d_{50,n}\,(v_{j,n} - v_{50,n})}{d_a} \tag{4.8}$$

where $v_{j,n}$ is the jet velocity, $d_{50,n}$ is the cut-off size of the impactor stage n and $v_{50,n}$ is the impact velocity of the cut-off size.

Calculated impaction velocity distributions can be used to calculate bounce probabilities for given particles entering the impactor. The necessary key parameters are the particle aerodynamic size d_a, particle density ρ_p, and the α coefficient. The charge transfer q_c can then be calculated from Equation 4.6. In addition to the theoretical model, some experimental adjustments were made to increase the agreement between the model and empirical collection curves also given by Arffman et al. (2011).

For inversion of the parameters (α, ρ_p and $q_{c,0}$), it is necessary to know the particle mobility size, bounce probability, the total current, and the current carried to the impactor by the particles with no charge transfer (the bounce current). The mobility size distribution can be measured, for example, with a scanning mobility particle sizer (SMPS). The charge transfer can be obtained by measuring the aerosol at two known charge states, from which the charge transfer effect can be eliminated. In practice this is achieved by measuring the same aerosol with a corona charger on and off. From the measured currents on all the stages and the backup filter, the charge transfer can be eliminated (see Equation 4.5), provided that the charge equalization factor β is zero:

$$I_{b,n} = I_{ch,on,n} - I_{ch,off,n} \tag{4.9}$$

After this, the simulated bounce current is fitted by iteration with the particle density and the α coefficient:

- computation of the aerodynamic particle size distribution from the mobility size distribution (Figure 4.2 d) with a density estimate
- computation of bounce probabilities for each particle size with aerodynamic sizes, ρ_p and α
- computation of the simulated $I_{b,n}$ (Figure 4.2 c) for the aerodynamic particle size distribution, using bounce probability calculated in previous steps and the Pn curve. Note that for the computation of $I_{b,n}$, the $I_{ch,on,n}$ can be used if the charge transfer is assumed zero and the aerosol is net neutral when charger is off.

This computation produces the density ρ_p and the coefficient $alpha$, which are independent of the charge transfer $q_{c,0}$. Using $alpha$ and the particle aerodynamic size distribution obtained from the density and the measured mobility size distribution, $I_{ch,off,n}$ is then simulated and iterated until optimal charge transfer is found.

The result is iterated with a suitable multivariable search algorithm until a minimum square root difference between the currents is found. The particle density is assumed independent of the particle size and most importantly the β factor is assumed zero such that the charge transfer is not dependent on the charge of the particle. If the size distribution is externally mixed or have strongly size-dependent properties, the results will be averaged over the population and some error in for example in the particle impaction velocity is expected, which results in errors for the charge transfer and α parameters.

Increasing the density moves the peak of the non-filter stage currents to larger sizes. Increasing the material coefficient of bouncing (α) decreases the filter current in $I_{b,n}$. Finally, adjusting the contact charge set $I_{ch,on,n}$ and $I_{ch,off,n}$. The resulting three parameters give the mechanical and electrical bounce characteristics as well as the density. The density is a suitable validation parameter with known test aerosols. The fitting process result is given in Figure 4.2.

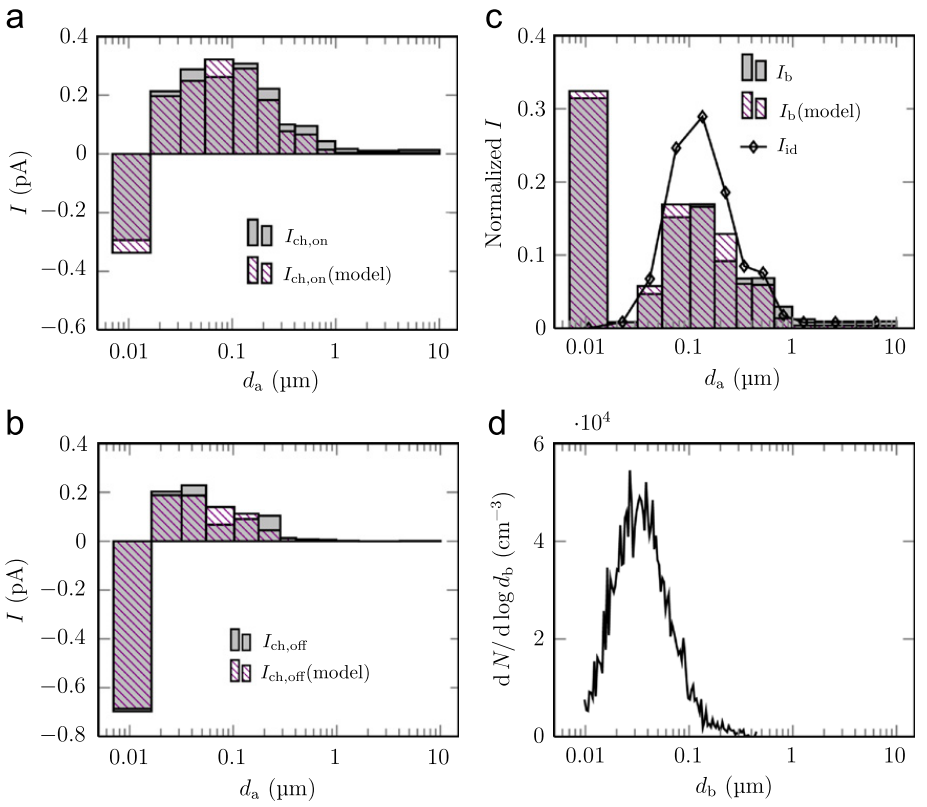

Figure 4.2: a) Measured and modeled ELPI currents with a charger on, based on the mobility size distribution in panel d. b) Measured and modeled current distributions for measurement with net-neutral particles. c) The bounce current, modeled bounce current and an ideal response of non-bouncing particles. Figure from **Paper 2**

The method has some drawbacks, which need to be acknowledged in the experiment design and data analysis. Low pressure inside the instrument precludes experimentation at ambient humidity level. This may be overcome by adapting the method to higher pressure system. The system measures the bounced fraction of the particles, which means that external mixtures can hide minority behavior in the particle population. Furthermore, behavior of internally mixed particles with separate phases can be dominated by the lowest viscosity phase in the particles.

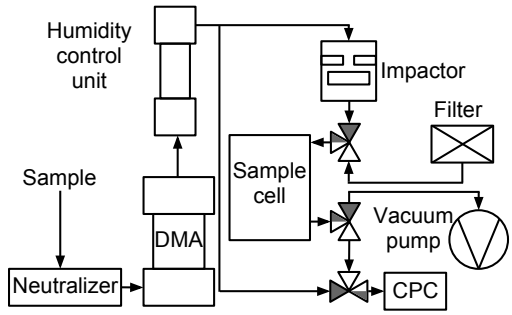

Figure 4.3: The optical detection bounce measurement setup, with a humidity control unit prior to the bounce measurement unit. Figure from **Paper 3**

4.5 Low pressure impactor with optical detection

To overcome the effect of charge transfer, a measurement setup was developed, based on a single impactor stage of the ELPI (**Paper 3**). In this setup, particles were counted using a condensation particle counter (CPC), which instead of electrical charge measurement detects particles optically.

Since the particle size range for SOA is often limited to the order of 100 nm, direct optical detection is very difficult. To secure single particle detection efficiency also for small particles, a condensation particle counter can be used (instrument shown in Figure 4.3). The system is a batch process measurement, in which after mobility size selection aerosol is passed through the impactor. After the flows have been stabilized, a sample is captured in a low pressure sampling cell, which is then brought up to the operating pressure of the CPC and measured for count of bounced particles.

The collection efficiency curve of the impactor is given in Figure 4.4. The aerodynamic sizes of the test particles used are marked in the figure, where it can be seen that the collection efficiencies for the ammonium sulfate and levoglucosan particles are different. This deviation from the collection efficiency must be taken into account when calculating the bounced fraction of the particles. As some of the particles get through the impactor without a bounce test, the corrected bounced fraction is given as:

$$B = \frac{B' - (1 - C_E(d_a))}{C_E(d_a)} \tag{4.10}$$

where $B\prime$ is the measured, uncorrected bounced fraction and $C_E(d_a)$ is the calibrated collection efficiency at the aerodynamic particle diameter d_a that was used.

4.6 Humidity control and hysteresis

Additional phenomenon related to SOA is the liquid–liquid phase separation (LLPS), which is relevant to multicomponent particles that have chemically very distinct fractions, such as secondary organic matter and inorganic salts. Even though both of the chemical phases are miscible with water, the phases separate if, for example the other phase is prone to efflorescence while the other is not (Bertram et al., 2011).

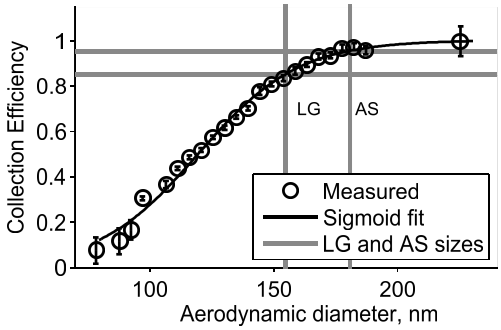

Figure 4.4: Collection efficiency curve of a single-stage optical detection impactor as measured with di-octyl sebacate (DOS). Aerodynamic sizes of the phase change test substances (ammonium sulfate (AS) and levoglucosan(LG)) are marked in the figure. Figure adapted from **Paper 3**.

To study the effect of humidity on the particle physical properties, a modular system was used to set the relative humidity at a desired value and also to have control over its relative humidity history. The possibility to control the history of the particles, enables the study of hysteresis on the humidity effects.

A recent study by Bateman et al. (2014) describes the fundamentals of particle bounce in impactors and the effect of humidity. They concluded, in agreement with **Paper 3** and **Paper 4**, that increasing humidity lowers the bounced fraction even for solid particles. This decreased bounce is due increased adhesion between particle and substrate caused by the surface energy modification by adsorbed water. The magnitude of this effect depends on the hygroscopicity of the substrate and the particle. For SOA particles, the effect is not very large. The SOA, which has no deliquescence energy barrier is less likely to have a surface layer of water, which explains the less pronounced gradual drop at low humidities. For example, ammonium sulfate and latex particles exhibit a large drop in the bounced fraction during a humidity increase from 20 to 70 % RH (Bateman et al., 2014, **Paper 3**).

Crystalline and mixed particles with phase separation behavior exhibit a memory in their physical phase state. This phase state is affected by their formation and humidity history. These hysteresis effects can be studied by exposing particles to carefully controlled humidity cycles. The hydration of particles can be studied simply by exposing them to an increasing humidity and by recording their bounce or water uptake. Hysteresis is measured by similar measurement but at a high-RH prehydration stage followed by a controlled drying stage.

A schematic of the humidity history cycles used in the phase hysteresis studies is shown in Figure 4.5. The left panel describes the phase state of a crystalline hydrophilic particle (red), which upon increasing relative humidity deliquesces when reaching the deliquescence relative humidity. The deliquesced particle remains deliquesced even after the RH drops below the DRH when the sample enters the impactor and pressure drop of Δp reduces the RH. Amorphous particle (green) gradually absorbs water and releases it, following the RH of the sample and exhibiting no hysteresis. This is why for particles with hysteresis the relevant humidity for the deliquescence is the maximum humidity of the system and for amorphous substances the actual RH at the measurement moment.

The system schematic is presented in Figure 4.6. The sample humidity is adjusted with

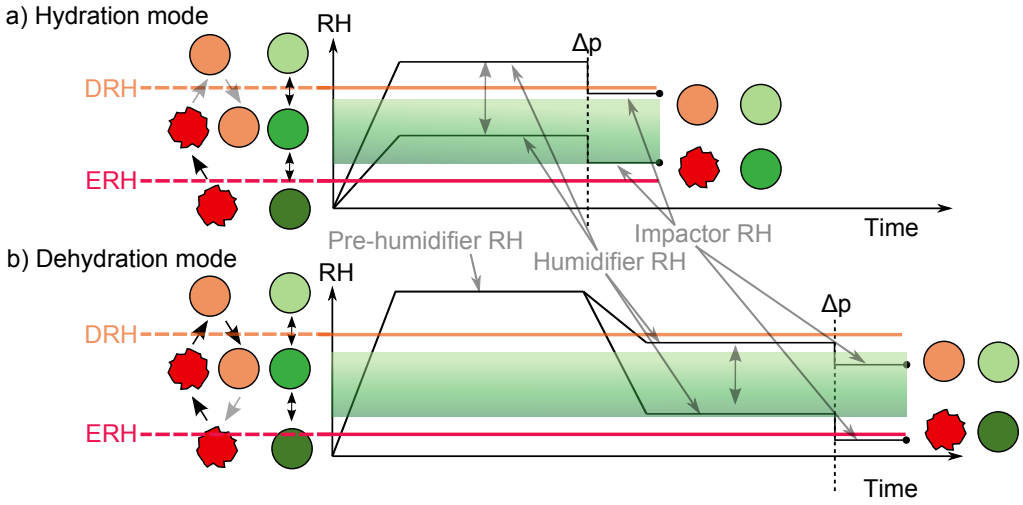

Figure 4.5: Humidity history with a hydration control setup and a deliquescence – dehydration cycle setup for hysteretic and amorphous particles. The green band describes the deliquescence range of amorphous matter and the magenta lines the efflorescence and deliquescence limits of a crystalline particle. Figure from **Paper 5**

two Nafion humidity exchangers, the first one filled with liquid water and heating provided either with a circulating water sheath or electrical heating. The heating is required to compensate for the enthalpy of vaporization, when water is transferred from the liquid phase to the gas phase. Adequate heating is used to keep the dew point of the system high enough to provide slightly over 90 % RH. The second humidity exchanger is a counter-current gas phase exchanger, which can dry the sample in the dehydration mode and increase the humidity in the hydration mode. The gas flow (10 lpm) providing the set RH is mixed from close to saturated air from a heated water-filled Nafion exchanger and dried air mixture. Humid air flows through a condensation trap and a restriction to maintain minimum water leakage from the high capacity humidifier. A second function for the flow restriction is to provide a small pressure drop to produce a similar drop in RH to prevent further condensation. By adjusting the mixing ratio of humid and dry air, the sample humidity can be quickly and accurately adjusted. After both of the sample conditioners there is a three second residence time tube to allow some time for the particles to equilibrate. When running in the hydration mode, only the latter (gray) humidity exchanger is used.

The particle behavior in the dehydration more is depicted in Figure 4.5b. The crystalline particles (red) deliquesced by the first humidifier and dried with the second one until the efflorescence relative humidity is reached. The impactor RH after the pressure drop Δp is the relevant humidity in the dehydration mode for both the amorphous and crystalline cases. From the point of view of the end state of the amorphous particle the dehydration and hydration modes are the same, since there is no hysteresis.

The system RH response was tested with two notably different but atmospherically relevant materials: ammonium sulfate and levoglucosan, the latter being an amorphous material commonly released into air during biomass burning (Mikhailov et al., 2009). The phase transition of an amorphous material is expected to be gradual upon increasing

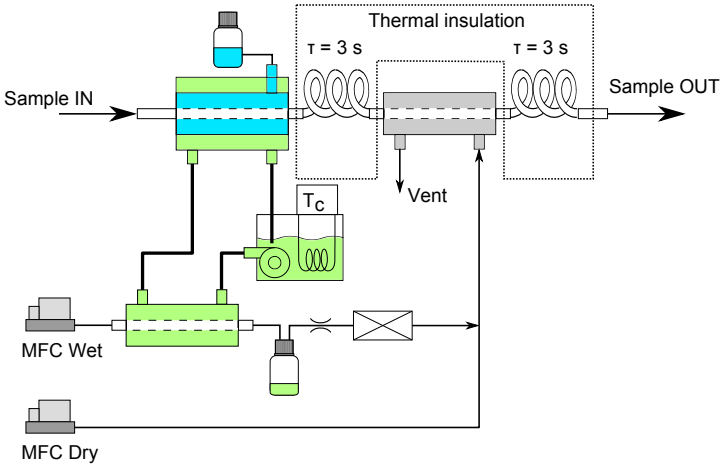

Figure 4.6: Schematic representation of a two-stage humidity setup with a stable first-stage, water-filled, high-RH humidifier and a fast counter-current, gas exchange second-stage humidifier.

relative humidity. Conversely, the sharp deliquescence and efflorescence distinctive to hydrophilic crystalline compounds are due to an energy barrier in the water absorption free energy (Seinfeld and Pandis, 1998).

The bounced fraction of ammonium sulfate is shown in Figure 4.7. The bounced fraction drops steadily due to the water adsorption on the ammonium sulfate, which increases the capillary force between the particle and the substrate (Romakkaniemi et al., 2001; Biskos et al., 2006; Mikhailov et al., 2009). Between 82 and 84 % humidifier RH the bounced fraction drops sharply, corresponding to deliquescence RH of the ammonium sulfate (Mikhailov et al., 2009). As explained previously, the maximum RH determines the deliquescence RH, as long as the subsequent RH does not drop below efflorescence limit.

The efflorescence RH is determined with the dehydration branch, where the lowest RH after deliquescence sets the efflorescence. Bounced fraction increases at 30 % impactor RH during the dehydration branch for ammonium sulfate, in agreement with Mikhailov et al. (2009). The grey symbols in Figure 4.7 denote downscan points after measured RH upscan. These show the loading effect of the substrate to be minimal.

Furthermore, as the particles deliquesce, their size increases by factors of 1.2 and 1.3 (Mikhailov et al., 2009). This size increase changes the aerodynamic particle size, but not very much, since the density of the particle decreases as the density of water is much lower than that of the seed particle. When the particles are hydrated, the new diameter is $d_p \cdot GF$ and the effective density, assuming a volume additivity of the mixture:

$$\rho_p = \frac{\rho_p + \rho_0 \left(GF^3 - 1\right)}{GF^3} \tag{4.11}$$

When the deliquesced density and mobility diameter is substituted to Equation 3.7, the deliquesced aerodynamic diameters are 162 nm and 188 nm, respectively. This results in a maximum error of 3.2 % of the collection efficiency. From the slope of the collection

efficiency curve the maximum error on corrected bounce to be:

$$\Delta B = \frac{1 - B'}{C_E} \Delta C_E \tag{4.12}$$

At the maximum condition i.e. lowest used collection efficiency and lowest bounce fraction (zero), the error is 3.8%, which is within experimental noise.

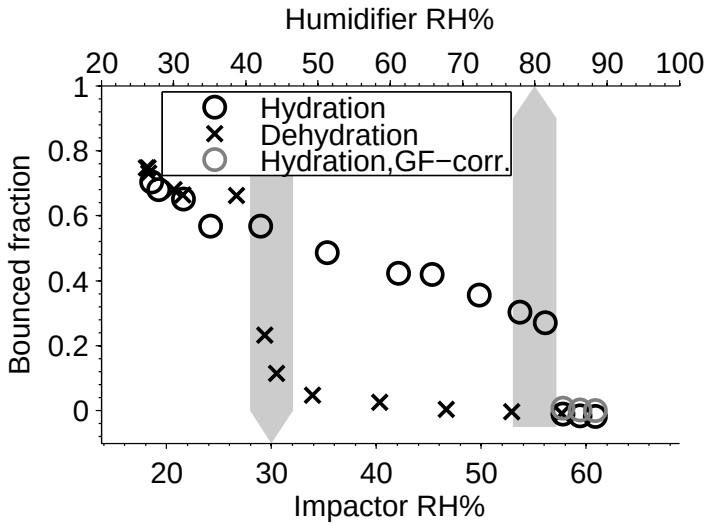

Figure 4.7: Bounce fractions of ammonium sulfate aerosol at hydration and dehydration experiments. The GF-corrected points denote hydration points corrected for water uptake induced change in aerodynamic particle size as discussed previously. The first humidifier was kept at 90 % RH for the ERH run. The arrows point at the efflorescence and deliquescence relative humidities reported in Mikhailov et al. (2009). Bounced fraction is corrected according to 4.10. The gray symbols denote downscan points, to show the effect of loading of the substrate. Figure from **Paper 3**

The bounced fraction of levoglucosan is shown in Figure 4.8. The bounced fraction reduces gradually upon increasing humidity from 30 % RH to 60 % corresponding very well to the HTDMA results by Mikhailov et al. (2009). There is very little hysteresis, and from theoretical standpoint, the amorphous matter should only exhibit hysteresis by kinetic limitations of the water absorption and desorption. Some hysteresis effects can also be cause by the morphology change due to the deliquescence in the first stage humidifier in the dehydration mode.

The remainder of the 10 lpm is mixed with the humid flow, and the flow is directed counter to the aerosol sample in a secondary, Nafion multitube humidifier. This arrangement provides a very fast setting and a stable and predictable sample humidity. The parameter for humidity adjustment is the ratio of the humid and dry air flows. The RH is nearly linear with the set ratio from almost dry to more than 90 %.

After both humidifiers, residence time of 3 s is provided by two coils of tubing enclosed in the same insulated enclosure as the impactor system. The residence time is chosen to provide some time for any humidity-induced phase changes. Three second settling provides total equilibrium for particles with viscosity less than approximately 1 Pa·s, viscosity of about thousand times that of pure water at room temperature. This phase

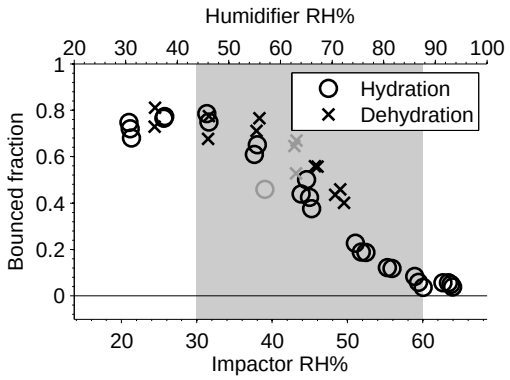

Figure 4.8: The bounced fraction of levoglucosan, measured with both the hydration and dehydration branches of the optical detection impactor setup. The humidity axes denote the RH in the adjustable humidifier, and the corresponding lower RH at the reduced pressure in the upstream of the impactor. Figure from **Paper 3**

change may have equilibration time scale up to one year for extremely highly viscous materials (Shiraiwa et al., 2011). The temperature and RH are measured and logged after each residence time tube.

4.7 SOA generation

To study the phase state of SOA, laboratory generated aerosol was used. The production of SOA calls for oxidation of volatile organic compounds, which are oxidized with ozone or hydroxyl radical to turn into less volatile species, which condense to form particles. The tools used for test SOA generation were two different smog chambers and a photochemical flow tube reactor. The oxidation condition in smog chambers are closer to ambient conditions than small flow tube reactors, but flow tube reactors can achieve oxidation ages comparable to up to ten days of atmospheric aging (Lambe et al., 2011a).

4.7.1 Smog chambers

The general idea of a smog chamber is to mimic atmospheric oxidation in well controlled conditions. The relevant issues are the particle losses, since atmosphere has no walls, so wall losses must be compensated or taken into account. The radiation, NOx and other oxidant levels in addition to humidity and temperature must be carefully controlled to produce SOA with repeatable properties and known conditions. A characterization of a typical chamber design is given in Takekawa et al. (2007). Smog chambers have been used for atmospheric research for decades, e.g. Leone et al. (1985).

The chamber used for α-pinene and pine SOA production in **Paper 1** was the smog chamber of the Aerosol Research Group of the University of Eastern Finland, soft fluorinated ethylene propylene (FEP) film chamber, operated in a batch mode for experiments lasting typically for 4-6 hours. The particles produced in **Paper 1** were formed by nucleation, no seeds were used, although sulfur dioxide (SO_2) was used to enhance the nucleation with the hydroxyl radical oxidation case. The air in the chamber was humidified to 25-35 % RH,

and ozone was injected as the oxidant for ozonolysis experiment and tetramethylethylene (TME) was added to produce additional hydroxyl radicals.

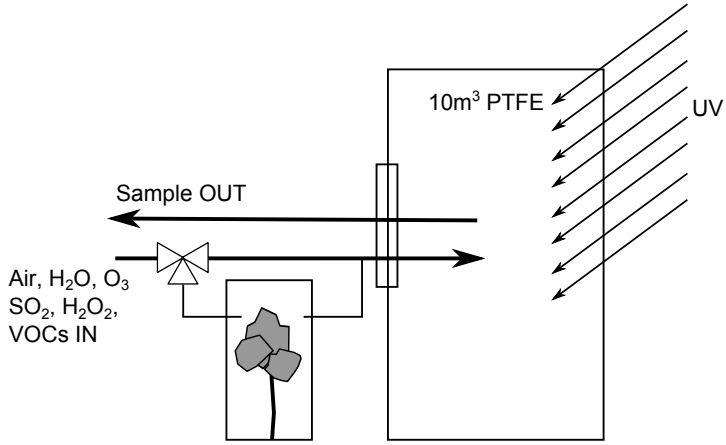

Figure 4.9: A simplified schematic of the Aerosol Physics Group smog chamber at the University of Eastern Finland with a separate plant VOC collection chamber. Plant VOCs can be flushed from the VOC collection chamber into the actual oxidation chamber.

The smog chamber used in the multicomponent particle studies (**Paper 5**) was the Harvard Environmental Chamber (HEC), a 5 m^3 PTFE film chamber with 254 nm UV lighting and an RH and temperature control. The chamber has a mean residence time for an air parcel of 4 hours and a typical experiment lasts for a day or more. The inlet gas flows are used to mix the chamber. Ozone was injected as the oxidant for dark ozonolysis experiment, while hydrogen peroxide (H_2O_2) was injected and dissociated with UV lights for *OH experiments. The seeds used in the experiments were ammonium sulfate generated with a Collison atomizer.

4.7.2 Potential aerosol mass reactor

The Potential aerosol mass (PAM) concept and a method to approximately measure it was introduced by Kang et al. (2007). The PAM is defined as the maximum aerosol particle mass that can be produced with oxidation of an aerosol, containing both primary particles and gaseous precursors. Reactors used for PAM studies are developed especially to produce SOA formation and aging at much higher oxidative aging on much shorter timescales than can be achieved with large smog chambers. The PAM reactor of the Davidovits Group at Boston College was used for SOA studies in **Paper 4**. The reactor is shown in Fig 4.11 and thoroughly characterized (Lambe et al., 2011a). A PAM chamber is considerably smaller than a smog chamber, but significantly higher oxidant levels and thus oxidation exposure can be achieved on much shorter timescales. (Lambe et al., 2011a)

The core components of a PAM reactor are the oxidant production system, the flow tube itself, and typically an ozone scrubber before aerosol measurement instrumentation (a schematic of a PAM setup is shown in Figure 4.10). The oxidants used are usually ozone and/or hydroxyl radicals. Ozone was produced in a separate UV production unit and mixed with a humidified carrier gas. The considerably more reactive hydroxyl radical is

produced via photo-dissociation of O_3 with in-chamber UVC lights of wavelength 254 nm, according to Equations 2.4 and 2.5.

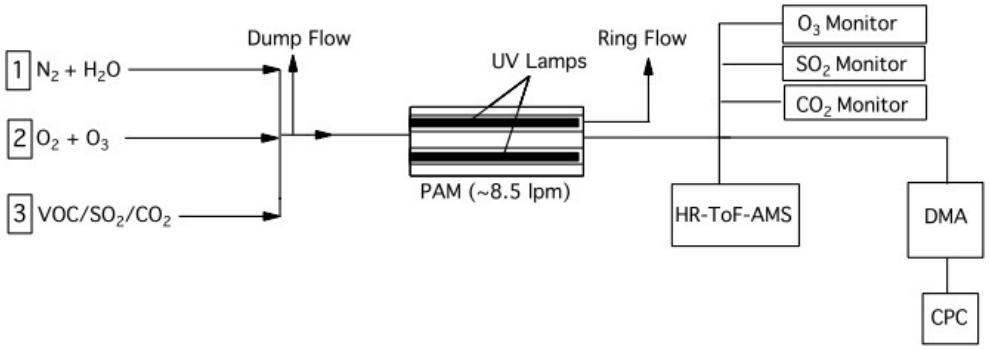

Figure 4.10: A schematic of a typical PAM reactor setup with measurement instrumentation. Adapted from (Lambe et al., 2011a)

OH^* production rate in the reaction was variable and very high, giving OH^* exposures of between $2{\cdot}10^{10}$ molec·cm^{-3}s and $1.8{\cdot}10^{12}$ molec·cm^{-3}s. The residence time in the chamber was approximately 1 min 45 s which compared to an atmospheric OH^* concentration of $1.5 \cdot 10^6$ molec·cm^{-3}, corresponds to an atmospheric aging of 0.2 to 14 days (Lambe et al., 2011a; Mao et al., 2009).

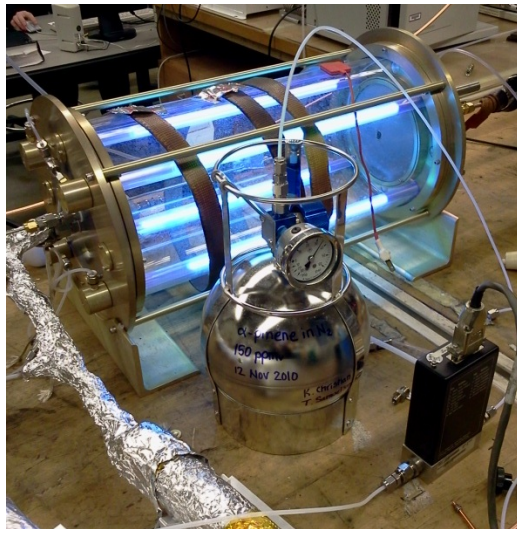

Figure 4.11: The Boston College PAM, photochemistry UV lights active and a bomb of α-pinene in use.

The correspondence of SOA produced with smog chambers and PAM reactors with natural SOA has been thoroughly probed with extensive measurements. Though it is impossible to get full molecular information of the SOA, and while there are some differences, the similarities are more striking than the differences, especially in properties that are most commonly used to describe the state of natural aerosols, though the much higher oxidant

concentrations and faster reaction rates may lead to chemistry not found in the atmosphere (Kroll and Seinfeld, 2008). With respect to, for example, O/C and H/C ratios, PAM SOA falls within the natural deviation of natural aerosols (Lambe et al., 2011b; Ng et al., 2010; Heald et al., 2010). The biggest unknown territory lies in the molar masses of the compounds making up SOA.

5 Factors affecting the phase state of secondary organic aerosol particles

In this chapter the results from the SOA experiments are presented mixed with the interpretation and discussion. Since most the measurements included response to humidity and oxidation level, the results are divided between pure SOA particles and seeded and multicomponent particles. The single precursor SOA experiments studied in **Paper 4** with different precursors answer to the question whether the solid phase of SOA is common or only seen in unrealistic atmospheric conditions. These experiments were performed with a range of RH up to 63 % RH with oxidation levels corresponding 2 to 17 days of aging.

To find out the effect of humidity cycling on the particle phase state, the effect of ammonium sulfate seed for SOA phase and the effect of RH, ammonium sulfate seeded SOA was studied in **Paper 5**. Sulfuric acid – SOA mixed particles were also studied in **Paper 4** and in dry impaction conditions in **Paper 1**.

5.1 Pure SOA particles

The starting point for the precursor study was the set of experiments by Virtanen et al. (2010), where pine-VOCs and α-pinene produced solid SOA, when measured in dry conditions. The phase state of SOA produced from different precursors was probed with the impactor with optical detection, up to RH of 63 %. The flow tube (PAM) reactor described in previous chapter was used to provide different oxidation levels for various precursors.

Even though the precursor molecules of biogenic SOA are typically of the terpene group, significant differences occur in the phase state of SOA, as well as the oxidation response. Depending on the structure of the precursor, varying ·OH exposure gives different O/C response, as seen in Figure 5.1. The exact oxidant exposures are given in **Paper 4**. The simplest terpene, isoprene, yields a solid SOA, but the bounced fraction drops steeply when the relative humidity increases above 55% RH as shown in the top panel of Figure 5.1.

The bounce measurement of SOA produced by n-heptadecane ($C_{17}H_{36}$) oxidation shows a very clear progression of oxidative hardening of SOA particles (**Paper 4**) as seen in Figure 5.2. The precursor is a liquid in normal conditions with high enough vapor pressure to be evaporated if formed into particles in concentrations used in the experiment. The highest bounced fractions are higher than that of levoglucosan, which is considered to be glass at relative humidity of 30 %, indicating viscosity change at least several orders of magnitude.

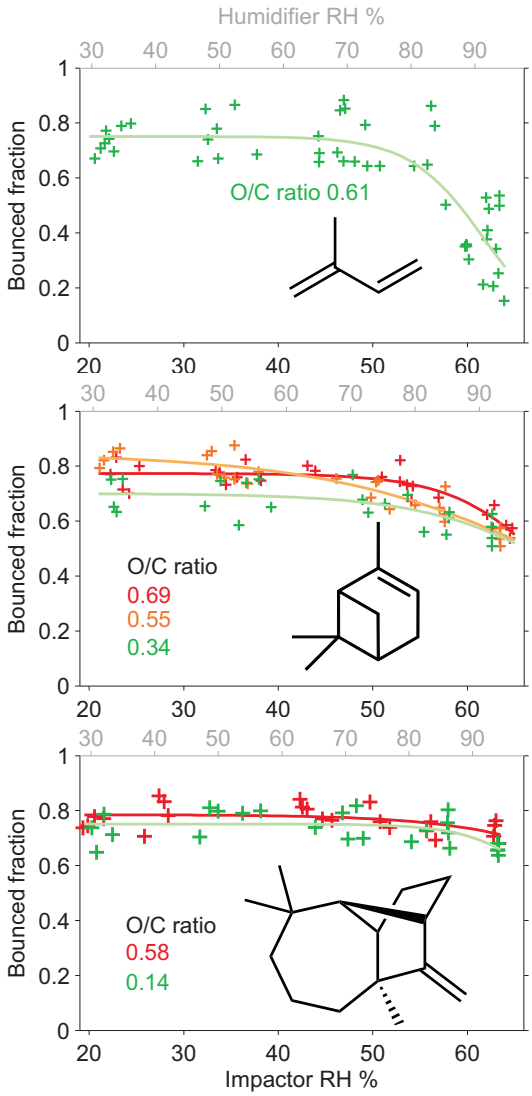

Figure 5.1: Bounced fractions biogenic SOA produced from isoprene, α-pinene and longifolene. The ·OH exposures were between 2 and 17 days (0 for O/C of 0.34 α-pinene ozonolysis case). Figure adopted from **Paper 4**

The alkane structure of n-heptadecane is prone to *OH oxidation, which leads at first to an increased bounced fraction at all RH levels. At the highest oxidation level, the hygroscopicity of molecules is increased due to increased polarity, which can be seen in the decreasing bounced fraction when RH is increased (the red points and curve). This effect can be quantified and separated from the oxidative hardening of SOM by measuring the slope of the decrease of bounce with respect to increasing humidity (shown in Figure 5.3). This slope is affected by the oxidation. The structure of the precursor molecule, however, plays a more significant role since the differences in the slope were more dependent on the precursor than, for example, on the O/C ratio of the measured SOA.

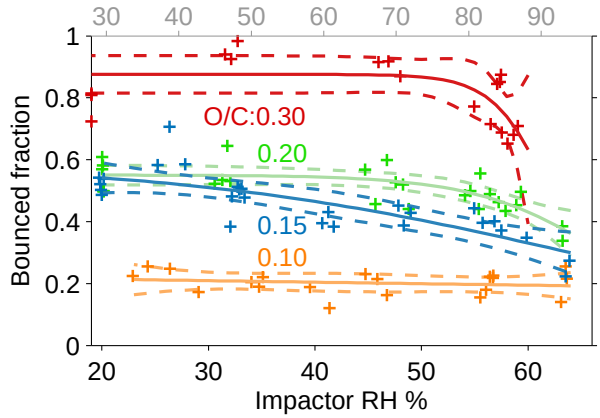

Figure 5.2: Bounced fraction of n-heptadecane SOA versus RH, oxidized to various O/C levels between 0.1 to 0.3, corresponding to photochemical ages between 2 and 9 days. Note the low slope with respect to RH compared to the high response to O/C change. Figure adopted from (**Paper 4**)

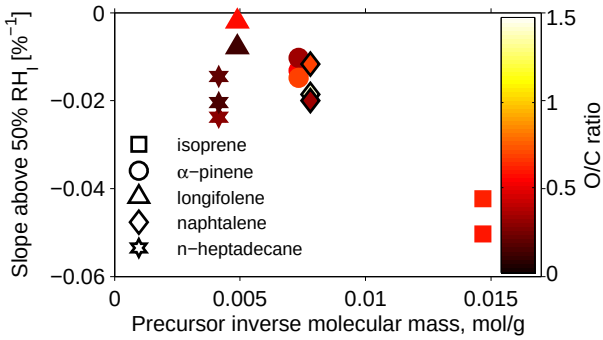

Figure 5.3: The slope of the bounced fraction with respect to increasing humidity. Note the correlation between the inverse molecular mass and the slope for non-alkane precursors. Figure adopted from **Paper 4**

As the oxidation of SOA continues, double bonds and cyclic structures become dissociated, and molecules start losing their mass as hydroxyl radical oxidation breaks the single bonds between the carbon atoms. This breaks up the molecule, and the saturation vapor pressure rises again, releasing the hydrocarbons again to the gas phase (Kroll et al., 2011; Seinfeld and Pandis, 1998). The viscosity of the particulate matter affects the oxidation rate in cases, where the material is reacting in or is transported from the particle bulk. SOA ages also with gas phase chemistry, as material is evaporated from the particle to the gas phase, where it is more likely to oxidize, and then condense back on on the particle. In case of high viscosity material, new condensation can hinder the transport of inner layers on the surface, as well as the transport of oxidants into the bulk Shiraiwa et al. (2011). The rate of oxidation sets a time range during which hydrocarbon products can exist in a condensed phase. Thus solid particles are expected to be more resistant to oxidative aging than low viscosity and liquid particles. Chemical half-life can be expected to range from hours to days for liquid and solid particles, respectively Shiraiwa et al. (2011). This kinetic barrier is lifted when particles are deliquesced, which allows for efficient mixing

between the surface and bulk of the particle.

The change in the chemical half-life of the aerosol in the atmosphere due to the solid phase and the diffusion limitations with the ubiquity of the solid phase can have an effect on some of the assumptions now used in atmospheric models for SOA. The role of the phase state of particles regarding the climate effects of SOA should be investigated further.

Water is so abundant in the atmosphere that it constantly interacts with the aerosol particles present. The interaction of water with SOA particles can be of physical or chemical nature. Physical interactions include absorption and adsorption processes, of which the absorption can change decrease the material viscosity and change density considerably.

As free water molecules meet a particle, they can be adsorbed on the surface or absorbed into the condensed matter bulk. The amount of absorptions depends strongly on the amount of available water and the properties of the substrate matter. Because hygroscopicity strongly depends on the polarity of the substrate material, more oxidized and thus more polar molecules are expected to be more water soluble. For the phase of the particle, hygroscopicity thus sets a compensating effects with increased viscosity brought on by oxidation: increased oxidation induces higher viscosity, but at the same time if water is available, higher oxidation induces a higher affinity to the water-induced softening and solubility of the material. This effect is clearly seen in Figure 5.2, where the overall bounced fraction increases with oxidation but the slope of bounced fraction is steeper. The effect of adsorption cannot be ruled out here, but since there is no energy barrier for absorption in amorphous matter, the role of adsorption is expected to be minimal compared to absorption. The ammonium sulfate is an exception, but for the coated particles the adsorption is likely not relevant for the bounce.

In addition to the phase change induced by changing relative humidity after the formation and growth of SOA, the phase is also dependent on the relative humidity during the formation of SOA, as the higher RH changes the oxidation chemistry to favor lower molecular mass products (Kidd et al., 2014).

5.2 Seeded and multicomponent particles

Because SOM is usually amorphous in form no energy barrier exists, its phase hysteresis for water uptake is caused by kinetic limitations of water evaporation (Bones et al., 2012; Mikhailov et al., 2009; Koop et al., 2011). If, however, a SOA particle is a mixture of SOM and a seed particle of crystalline material, such as most salts, the humidity response changes. Crystalline materials exhibit hysteresis due to the different minimum energy configuration of the crystal structure so that both the deliquesced and dry forms can exist at the same RH. When amorphous and crystalline material are mixed, hysteresis becomes a combination of both time-dependent and independent, but thermodynamic hysteresis effects.

The bounced fraction hysteresis behavior of mixed ammonium sulfate – SOA particles was studied in **Paper 5**, SOA was produced in a smog chamber separately by dark ozonolysis of α-pinene and by photo-oxidation of both α-pinene and isoprene, all with ammonium sulfate particles as seeds. The organic fraction in all experiments involving SOA was in the range of $0.77-0.89$. The two-branch humidity control setup described in section 4.6 was used along with the low pressure impactor described in section 4.5 to obtain bounced fraction response to different humidity as well as the hysteresis behavior

Table 5.1: O/C ratio and organic volume fraction for singly charged seed and total particle.

Experiment	O/C ratio	ϵ	d_m / Seed d_m (nm)	Coat (nm)
α-pinene *OH	0.31±0.01	0.89±0.03	145±15 / 70±6	38±16
α-pinene *OH	0.31±0.01	0.82±0.05	125±13 / 70±6	28±14
α-pinene O_3	N/A	0.82±0.05	125±13 / 70±6	28±14
α-pinene O_3	0.33±0.01	0.86±0.04	135±14 / 70±6	33±15
Isoprene *OH	0.70±0.01	0.82±0.05	125±13 / 70±6	28±14
Isoprene *OH	0.71±0.01	0.77±0.06	115±12 / 70±6	22±13

of the bounced fraction. The results are shown in Figure 5.4 and the experimental details in Table 5.1.

The exact behavior of the hysteresis of SOA, compared with that of pure AS and pure SOM, can be used to deduce phase and mixing information about the particles. In Figure 5.4a), the deliquescence and efflorescence of ammonium sulfate seed is seen at a relative humidity of 80 %RH and 30 %RH, respectively. The drop in bounced fraction before the deliquescence at 80 % is explained by the strong adsorption effect of the ammonium sulfate Bateman et al. (2014).

When photo-oxidized α-pinene SOM (Figure 5.4b)) is condensed on particles, their behavior changes significantly. The bounced fraction (BF) remains above 0.7 until the deliquescence RH of the seed is reached. The amorphous material is expected to exhibit much lower adsorption effect compared to ammonium sulfate, since there is no thermodynamic barrier for absorption shown by for example Smith et al. (2011), by the growth factors of SOA particles at 50 % RH. An offset in the bounced fractions of approximately 0.2 is retained after deliquescence.

At the dehydration branch, however, the bounced fraction starts to increase immediately upon decreasing RH, and the final efflorescence step of the seed is less than 0.2. This shows that the water interaction of the seed is independent of the SOM, while the SOM behavior is very similar to that shown for pure α-pinene SOA particles in Figure 5.1. In other words, the two compounds do not mix, even after deliquescence. The mixing of the two phases would also change the prominent deliquescence and efflorescence relative humidities, as shown by Smith et al. (2012). This agrees with Bertram et al. (2011), who give an O/C limit of 0.7 for liquid-liquid phase separation (LLPS), whereas the α-pinene experiments in Figure 5.4 is 0.30 (further details are presented in **Paper 5**).

The offset in the bounced fraction can indicate either particle bounce despite deliquesced seed or an almost impermeable SOM coating on some of the particles, which inhibits the deliquescence of the seed. In the case of impermeable coating, most particles have an incomplete SOM coating over the seed, while the 20 % that do bounce have a complete shell. Particle bounce with even with the seed deliquesced is more likely explanation, since the pure SOA results in Figure 5.1 show that SOA does bounce even at impactor RH higher than the corresponding DRH of the ammonium sulfate.

A similar experiment but hydroxyl radical as oxidant is shown in Figure 5.4d). The behavior is similar to the photo-oxidation experiment, except for the efflorescence branch, where an efflorescence step typical of ammonium sulfate seed is not seen. One explanation may be the mixing of the two phases while deliquesced. This is, however, contradicted by Bertram et al. (2011), where the 0.7 O/C limit for LLPC is much higher than the O/C

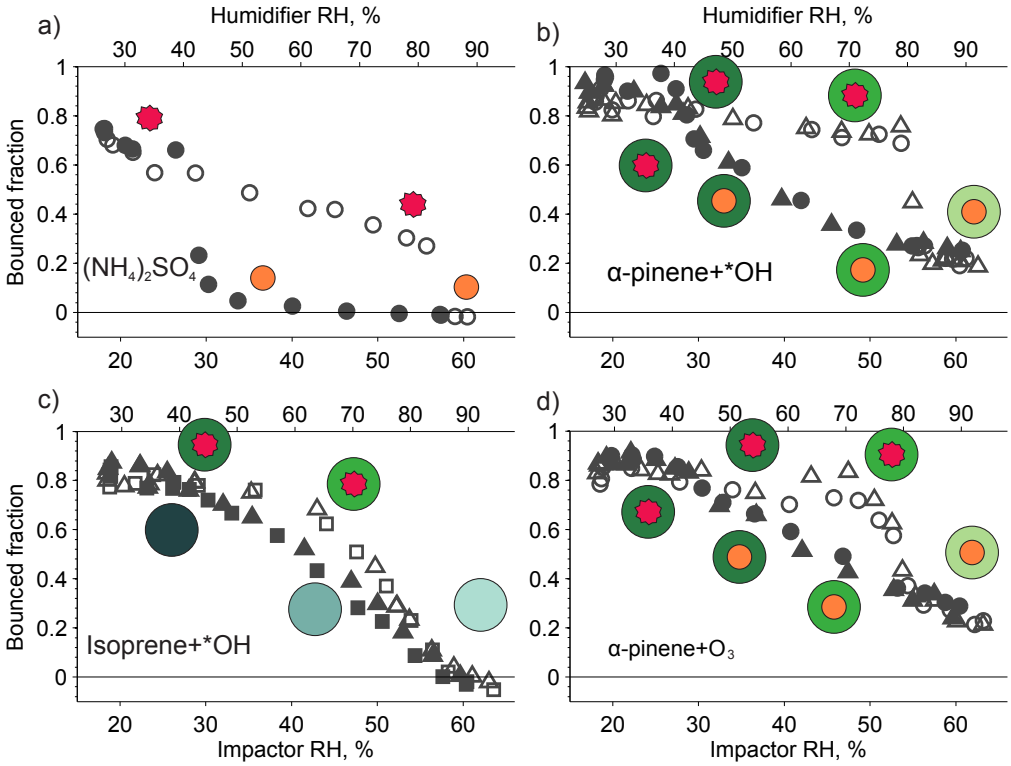

Figure 5.4: Bounced fraction and hysteresis results for a) pure ammonium sulfate particles, b) AS seed coated with photo-oxidized α-pinene SOM, c) AS seed coated with photo-oxidized isoprene SOM, and d) AS seed coated with α-pinene SOM produced via dark ozonolysis. Inferred particle morphologies are represented as drawings close to the data points. The green part in the drawing is the SOM and the red the AS core. The green becoming lighter denotes decreasing viscosity for both SOM and mixed cases. In the case of AS, light color denotes the deliquesced phase. For the data points, the open symbols denote the hydration cycle of the experiment whereas closed symbols denote the hydration-dehydration cycle. Different symbols denote different particle sizes (exact parameters are given in **Paper 5**).

achieved (0.33) with dark ozonolysis in the experiment. Another, more likely explanation is the low susceptibility of SOM to water, as shown in **Paper 4**.

The seeded experiment with isoprene (O/C of 0.7) is at the limit of LLPS (0.7) given by Bertram et al. (2011), and the data shown in Figure 5.4 is in agreement. The deliquescence of the AS seed is, however, masked under the deliquescence of isoprene SOM. In the pure SOM experiment in Figure 5.1 the bounced fraction of isoprene SOA drops much earlier than that of α-pinene SOA, while having lower O/C ratio. The efflorescence branch shows some hysteresis, possibly influenced by the mixing of the phases.

In **Paper 1** SOA produced from pine-emitted VOCs and SO_2 was studied with the electrical low pressure impactor (ELPI) cascade. The particles are composed of the organic matter and sulfuric acid produced from the sulfur dioxide. Figure 5.5 shows the bounce factor measured with an ELPI during the SOM condensation growth. The 17 nm and 30 nm limits are the cutoff sizes of the impactor for the two bounce factor calculations and provide some sensitivity limits for the result. The ammonium sulfate test points

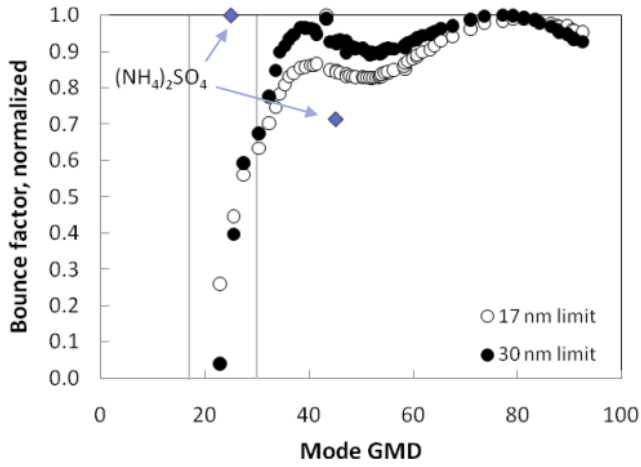

Figure 5.5: Normalized bounce factor during particle growth by pine VOC and SO_2 oxidation by $^*OH$. Figure from **Paper 1**.

indicate the bounce factor for pure ammonium sulfate test particles, which have lowest bounce factor at 50 nm size than the SOA, but the anomaly is explained by the charge transfer properties of the different materials. The mixed SOA-sulfuric acid particles start off with very low bounce factor at around 23 nm and start increasing immediately with increasing particle size. Because of the low pressure, this is the bounce factor of dry particles and it is seen that as the SOM is condensing on the particles, the bounce factor increases sharply until 40 nm, after which the bounced fraction fluctuates. The slight fluctuation can be caused by the different impact velocities of the different stages and thus different charge transfer of the particles.

When the particles are small, a higher fraction of the particle is amines, sulfuric acid, and also water because sulfuric acid is highly hygroscopic. As particles grow, the seed no longer dominates their behavior, and the SOM causes the particles to bounce.

In addition to the change in composition, the oxidation of the SOM changes during the experiment. The particle diameter increase during the growth from 30 nm to 90 nm corresponds to an O/C ratio increase from 0.21±0.01 to 0.35±0.01, as calculated using the parametrization by Ng et al. (2010). In this experiment the oxidation and the particle size have an effect on the composition. The size change matters due to particles having a higher sulfuric acid concentration when fresh, in addition to the different oxidation state of the SOM, as discussed in Section 5.1. The present experiment cannot distinguish whether the sulfuric acid concentration or the oxidation of the SOM causes the change in bounce factor. The change in the O/C-ratio is, however, less radical than the composition change.

Figure 5.6 shows the measured bounced fraction of mixed particles consisting of sulfuric acid and longifolene SOM with an O/C ratio of 0.7–0.8. The high O/C ratio is above the LLPS threshold of 0.7, which indicates completely mixed system. The addition of sulfuric acid clearly drops the bounced fraction of the SOA even at RH below 30 % impactor RH; a 20 % SO_4 content in the particles induces a gradual phase change at 50±10[%], and a further increase to a 36 % SO_4 content drops particle bounce below 0.1 at all measured humidities. Based on this, the bounce behavior seen with the pine-derived SOA in **Paper**

1 is accounted for with high sulfur content at particle sizes below 35 nm.

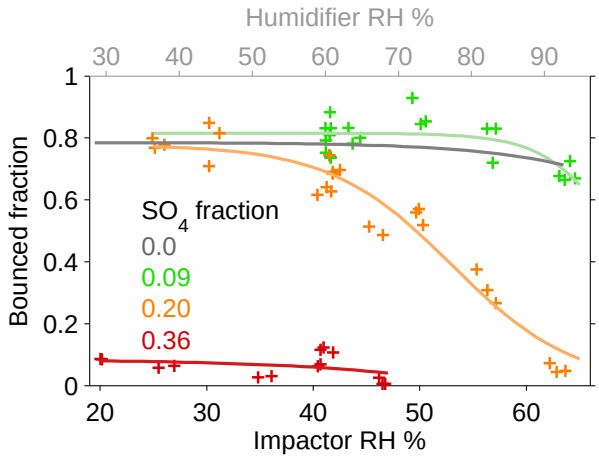

Figure 5.6: Bounced fraction of mixed SOM – sulfuric acid particles with different sulfate mass fractions. The SOM is longifolene SOM with an O/C ratio of 0.70–0.80. Figure from **Paper 4**.

6 Summary

The phase of secondary organic aerosol has consequences for the lifetime of particles in the atmosphere and for their cloud condensation probability. The effect of SOA on the climate depends on many factors. One is presumably the phase state of particles. A need for methods to measure the phase state was the driving force behind the development of instruments and method. A new method was thus devised to study particle mechanical and electrical properties from the measurement signal of an electrical low pressure impactor designed to measure particle size distribution.

With a different approach, a new instrument was developed to measure the phase state of particles with well defined relative humidity and relative humidity history. The instrument was characterized for response on crystalline and amorphous test materials. The instrument was applied to measuring pure and seeded SOA generated with an aerosol smog chamber and a continuous flow tube reactor. In addition to new measurement methods, important new findings emerged to indicate that the solid phase is very common to biogenic SOA.

Experiments with laboratory-generated single component SOA revealed that the phase state of SOA depends on the precursor material, the oxidation state of the organic material, and the relative humidity. The SOA produced was amorphous and was found to bounce in most cases at higher than 50 % RH. The generated SOA had a solid state for all systems studied though the anthropogenic alkane precursor solidified only at a high oxidation level. Increasing oxidation increased particle bounce as the organic material viscosity increased upon oxidation. At the same time, however, hygroscopicity increased with an increasing O/C ratio, as seen also with atmospheric SOA by Jimenez et al. (2009). This indicates that at least a local viscosity maximum exists on the humidity scale. An additional complexity arises from the effect of precursors, which in general is larger than the oxidation effect.

When SOA is internally mixed with sulfuric acid, the sulfuric acid fraction dominates the particle phase state even at low concentrations. Relative humidity history also plays a role since the sulfate seed of a particle dominates its bounce behavior after the seed deliquescence threshold humidity has been reached. These results only shown that the water is able to deliquesce the ammonium sulfate, but the actual state of the SOM is unknown. Thus another dimension to the phase state map is introduced by the seed. In conclusion, the solid phase state of SOA particles is expected to be very common and to depend on the precursors, ambient relative humidity and aging. The phase state has an impact on the interaction of SOA with the atmosphere, especially where atmospheric age is of importance, and should be taken into account when atmospheric models containing SOA effects are improved.

The technique and methods developed in this work are a step towards a better charac-

terization of particle physical properties. The levels, however, do not yet reach those where the measurement signal could be directly linked, for example, with the viscosity or elastic modulus of the particle to facilitate kinetic chemical and fluid dynamic modeling of particle interaction with the surrounding atmosphere. Substrate effects need to be studied more carefully, along with theoretical and computational effort.

The need for methods to determine the phase and ultimately the viscosity and diffusion constants of particulate matter has inspired many new methods after the work published in **Paper 2** and **Paper 3**. The current branches of study also borrow from other disciplines, the most important being improvements in optical measurement of the bounced fraction, the particle coalescence studies of Pajunoja et al. (2014); Renbaum-Wolff et al. (2013); Power et al. (2013), probe particle flow within a SOM sample by Renbaum-Wolff et al. (2013), ozone uptake and reactivity measurements(Shiraiwa et al., 2011) and advances in computation (Miyakawa et al., 2013). The research is active, and further improvements in instrument, theoretical, and computational studies are to be expected.

Review of the original articles

Paper 1: The method described in Virtanen et al. (2010) was extended to smaller particle sizes and different particle compositions of secondary organic aerosol (SOA). The main finding of the article was the solid phase of SOA particles, already at particle sizes below 40 nm indicating that the solid phase is ubiquitous in at least dry conditions.

Paper 2: A new data analysis method was developed to extract bonce and charge transfer coefficinets of particles from the measurement signal of an electrical low pressure impactor (ELPI).

Paper 3: A new instrument was developed to quantitatively measure the bounce of nanoparticles also at elevated relative humidity. The instrument could distinguish between a solid and deliquesced phase but also between crystalline and amorphous phases.

Paper 4: The method developed in **Paper 3** was applied to measuring aged SOA, produced in a potential aerosol mass (PAM) reactor. The ubiquity of the solid phase was demonstrated at a relative humidity of below 60 %. The bounced fraction and the humidity response was shown to depend on the precursor material and oxidation state.

Paper 5: The method developed in **Paper 3** was applied to ammonium sulfate seeded isoprene and α-pinene SOA. The seed dominated the particle bounce behavior, independently confirming the findings of earlier research by Bertram et al. (2011).

Bibliography

Aitken, J. (1889). On the number of dust particles in the atmosphere. *Transactions of Royal Society of Edinburgh*, 35(16):187 – 206.

Aitken, J. (1912). The sun as a fog producer. *Proceedings of Royal Society of Edinburgh*, 32(33):512 – 536.

Almeida, J., Schobesberger, S., Kürten, A., Ortega, I. K., Kupiainen-Määttä, O., Praplan, A. P., Adamov, A., Amorim, A., Bianchi, F., Breitenlechner, M., David, A., Dommen, J., Donahue, N. M., Downard, A., Dunne, E., Duplissy, J., Ehrhart, S., Flagan, R. C., Franchin, A., Guida, R., Hakala, J., Hansel, A., Heinritzi, M., Henschel, H., Jokinen, T., Junninen, H., Kajos, M., Kangasluoma, J., Keskinen, H., Kupc, A., Kurtén, T., Kvashin, A. N., Laaksonen, A., Lehtipalo, K., Leiminger, M., Leppä, J., Loukonen, V., Makhmutov, V., Mathot, S., McGrath, M. J., Nieminen, T., Olenius, T., Onnela, A., Petäjä, T., Riccobono, F., Riipinen, I., Rissanen, M., Rondo, L., Ruuskanen, T., Santos, F. D., Sarnela, N., Schallhart, S., Schnitzhofer, R., Seinfeld, J. H., Simon, M., Sipilä, M., Stozhkov, Y., Stratmann, F., Tomé, A., Tröstl, J., Tsagkogeorgas, G., Vaattovaara, P., Viisanen, Y., Virtanen, A., Vrtala, A., Wagner, P. E., Weingartner, E., Wex, H., Williamson, C., Wimmer, D., Ye, P., Yli-Juuti, T., Carslaw, K. S., Kulmala, M., Curtius, J., Baltensperger, U., Worsnop, D. R., Vehkamäki, H., and Kirkby, J. (2013). Molecular understanding of sulphuric acid-amine particle nucleation in the atmosphere. *Nature*, 502(7471):359 – 363.

Andreae, M. and Rosenfeld, D. (2008). Aerosol – cloud – precipitation interactions. part 1. the nature and sources of cloud-active aerosols. *Earth-Science Reviews*, 89(1):13 – 41.

Arffman, A., Marjamäki, M., and Keskinen, J. (2011). Simulation of low pressure impactor collection efficiency curves. *Journal of Aerosol Science*, 42(5):329 – 340.

Bateman, A. P., Belassein, H., and Martin, S. T. (2014). Impactor apparatus for the study of particle rebound: Relative humidity and capillary forces. *Aerosol Science and Technology*, 48(1):42 – 52. http://dx.doi.org/10.1080/02786826.2013.853866.

Bergström, L. (1997). Hamaker constants of inorganic materials. *Advances in Colloid and Interface Science*, 70:125 – 169.

Bertram, A., Martin, S., Hanna, S., Smith, M., Bodsworth, A., Chen, Q., Kuwata, M., Liu, A., You, Y., and Zorn, S. (2011). Predicting the relative humidities of liquid-liquid phase separation, efflorescence, and deliquescence of mixed particles of ammonium sulfate, organic material, and water using the organic-to-sulfate mass ratio of the particle and the oxygen-to-carbon elemental ratio of the organic component. *Atmospheric Chemistry and Physics*, 11(21):10995 – 11006.

Biskos, G., Paulsen, D., Russell, L. M., Buseck, P. R., and Martin, S. T. (2006). Prompt deliquescence and efflorescence of aerosol nanoparticles. *Atmospheric Chemistry and Physics*, 6(12):4633 – 4642.

Bones, D. L., Reid, J. P., Lienhard, D. M., and Krieger, U. K. (2012). Comparing the mechanism of water condensation and evaporation in glassy aerosol. *Proceedings of the National Academy of Sciences*, 109(29):11613 – 11618.

Calogirou, A., Larsen, B., and Kotzias, D. (1999). Gas-phase terpene oxidation products: a review. *Atmospheric Environment*, 33(9):1423 – 1439.

Cappa, C. D. and Wilson, K. R. (2011). Evolution of organic aerosol mass spectra upon heating: implications for oa phase and partitioning behavior. *Atmospheric Chemistry and Physics*, 11(5):1895 – 1911.

Cheng, Y.-S. and Yeh, H.-C. (1979). Particle bounce in cascade impactors. *Environmental Science & Technology*, 13(11):1392 – 1396.

Dahneke, B. (1971). The capture of aerosol particles by surfaces. *Journal of colloid and interface science*, 37(2):342 – 353.

Ehn, M., Thornton, J. A., Kleist, E., Sipilä, M., Junninen, H., Pullinen, I., Springer, M., Rubach, F., Tillmann, R., Lee, B., Lopez-Hilfiker, F., Andres, S., Acir, I.-H., Rissanen, M., Jokinen, T., Schobesberger, S., Kangasluoma, J., Kontkanen, J., Nieminen, T., Kurtén, T., Nielsen, L. B., Jørgensen, S., Kjaergaard, H. G., Canagaratna, M., Dal Maso, M., Berndt, T., Petäjä, T., Wahner, A., Kerminen, V.-M., Kulmala, M., Worsnop, D. R., Wildt, J., and Mentel, T. F. (2014). A large source of low-volatility secondary organic aerosol. *Nature*, 506(7489):476 – 479.

Hallquist, M., Wenger, J. C., Baltensperger, U., Rudich, Y., Simpson, D., Claeys, M., Dommen, J., Donahue, N. M., George, C., Goldstein, A. H., Hamilton, J. F., Herrmann, H., Hoffmann, T., Iinuma, Y., Jang, M., Jenkin, M. E., Jimenez, J., Kiendler-Scharr, A., Maenhaut, W., McFiggans, G., Mentel, T. F., Monod, A., Prévôt, A. S. H., Seinfeld, J. H., Surratt, J. D., Szmigielski, R., and Wildt, J. (2009). The formation, properties and impact of secondary organic aerosol: current and emerging issues. *Atmospheric Chemistry and Physics*, 9(14):5155 – 5236.

Hammer, E., Bukowiecki, N., Gysel, M., Jurányi, Z., Hoyle, C. R., Vogt, R., Baltensperger, U., and Weingartner, E. (2014). Investigation of the effective peak supersaturation for liquid-phase clouds at the high-alpine site jungfraujoch, switzerland (3580 m a.s.l.). *Atmospheric Chemistry and Physics*, 14(2):1123 – 1139.

Heald, C., Kroll, J., Jimenez, J., Docherty, K., DeCarlo, P., Aiken, A., Chen, Q., Martin, S., Farmer, D., and Artaxo, P. (2010). A simplified description of the evolution of organic aerosol composition in the atmosphere. *Geophysical Research Letters*, 37(8):L08803.

Hinds, W. (1998). *Aerosol technology: properties, behavior, and measurement of airborne particles, 2nd edition*. Wiley-Interscience, New York, NY.

Höhne, G., Hemminger, W., and Flammersheim, H. (2003). *Differential scanning calorimetry*. Springer Verlag.

Hunter, J. F., Carrasquillo, A. J., Daumit, K. E., and Kroll, J. H. (2014). Secondary organic aerosol formation from acyclic, monocyclic, and polycyclic alkanes. *Environmental Science & Technology*, 48(17):10227 – 10234. PMID: 25093758.

IUPAC (1997). *Compendium of Chemical Terminology, 2nd ed. (the "Gold Book")*. Blackwell Scientific Publications, Oxford. Compiled by A. D. McNaught and A. Wilkinson.

Jimenez, J. L., Canagaratna, M. R., Donahue, N. M., Prevot, A. S. H., Zhang, Q., Kroll, J. H., DeCarlo, P. F., Allan, J. D., Coe, H., Ng, N. L., Aiken, A. C., Docherty, K. S., Ulbrich, I. M., Grieshop, A. P., Robinson, A. L., Duplissy, J., Smith, J. D., Wilson, K. R., Lanz, V. A., Hueglin, C., Sun, Y. L., Tian, J., Laaksonen, A., Raatikainen, T., Rautiainen, J., Vaattovaara, P., Ehn, M., Kulmala, M., Tomlinson, J. M., Collins, D. R., Cubison, M. J., E., Dunlea, J., Huffman, J. A., Onasch, T. B., Alfarra, M. R., Williams, P. I., Bower, K., Kondo, Y., Schneider, J., Drewnick, F., Borrmann, S., Weimer, S., Demerjian, K., Salcedo, D., Cottrell, L., Griffin, R., Takami, A., Miyoshi, T., Hatakeyama, S., Shimono, A., Sun, J. Y., Zhang, Y. M., Dzepina, K., Kimmel, J. R., Sueper, D., Jayne, J. T., Herndon, S. C., Trimborn, A. M., Williams, L. R., Wood, E. C., Middlebrook, A. M., Kolb, C. E., Baltensperger, U., and Worsnop, D. R. (2009). Evolution of organic aerosols in the atmosphere. *Science*, 326(5959):1525 – 1529.

John, W., Reischl, G., and Devor, W. (1980). Charge transfer to metal surfaces from bouncing aerosol particles. *Journal of Aerosol Science*, 11(2):115 – 138.

Kang, E., Root, M., Toohey, D., and Brune, W. (2007). Introducing the concept of potential aerosol mass (pam). *Atmospheric Chemistry and Physics*, 7(22):5727 – 5744.

Keskinen, J., Marjamäki, M., Virtanen, A., Mäkelä, T., and Hillamo, R. (1999). Electrical calibration method for cascade impactors. *Journal of Aerosol Science*, 30(1):111 – 116.

Kidd, C., Perraud, V., Wingen, L. M., and Finlayson-Pitts, B. J. (2014). Integrating phase and composition of secondary organic aerosol from the ozonolysis of α-pinene. *Proceedings of the National Academy of Sciences*, 111(21):7552 – 7557.

Kirkby, J., Curtius, J., Almeida, J., Dunne, E., Duplissy, J., Ehrhart, S., Franchin, A., Gagné, S., Ickes, L., Ḱurten, A., Kupc, A., Metzger, A., Riccobono, F., Rondo, L., Schobesberger, S., Tsagkogeorgas, G., Wimmer, D., Amorim, A., F, B., Breitenlechner, M., David, A., Dommen, J., Downard, A., Ehn, M., Flagan, R., Haider, S., Hansel, A., Hauser, D., Jud, W., Junninen, H., Kreissl, F., Kvashin, A., A., L., Lehtipalo, K., Lima, J., Lovejoy, E., Makhmutov, F., Mathot, S., Mikkilä, J., Minginette, P., Mogo, S., Nieminen, T., Onnela, A., Pereira, P., Petäjä, T., Schnitzhofer, R., Seinfeld, S. P., Sipilä, M., Stozhkov, Y., Stratmann, F., Tome, A., Vanhanen, J., Viisanen, Y., Vrtala, A., Wagner, P., Walther, H., Weingartner, E., Wex, H., Winkler, P., Carslaw, K., Worsnop, D., Baltensberger, U., and Kulmala, M. (2011). Role of sulphuric acid, ammonia and galactic cosmic rays in atmospheric aerosol nucleation. *Nature*, 476(7361):429 – 433.

Koop, T., Bookhold, J., Shiraiwa, M., and Pöschl, U. (2011). Glass transition and phase state of organic compounds: dependency on molecular properties and implications for secondary organic aerosols in the atmosphere. *Phys. Chem. Chem. Phys.*, 13:19238 – 19255.

Kroll, J. H., Donahue, N. M., Jimenez, J. L., Kessler, S. H., Canagaratna, M. R., Wilson, K. R., Altieri, K. E., Mazzoleni, L. R., Wozniak, A. S., Bluhm, H., Mysak, E. R., Smith, J. D., Kolb, C. E., and Worsnop, D. R. (2011). Carbon oxidation state as a metric for describing the chemistry of atmospheric organic aerosol. *Nature Chemistry*, 3(2):133 – 139.

Kroll, J. H. and Seinfeld, J. H. (2008). Chemistry of secondary organic aerosol: Formation and evolution of low-volatility organics in the atmosphere. *ATMOSPHERIC ENVIRONMENT*, 42(16):3593 – 3624.

Kulmala, M., Vehkamäki, H., Petäjä, T., Maso, M. D., Lauri, A., Kerminen, V.-M., Birmili, W., and McMurry, P. (2004). Formation and growth rates of ultrafine atmospheric particles: a review of observations. *Journal of Aerosol Science*, 35(2):143 – 176.

Lambe, A. T., Ahern, A. T., Williams, L. R., Slowik, J. G., Wong, J. P. S., Abbatt, J. P. D., Brune, W. H., Ng, N. L., Wright, J. P., Croasdale, D. R., Worsnop, D. R., Davidovits, P., and Onasch, T. B. (2011a). Characterization of aerosol photooxidation flow reactors: heterogeneous oxidation, secondary organic aerosol formation and cloud condensation nuclei activity measurements. *Atmospheric Measurement Techniques*, 4(3):445 – 461.

Lambe, A. T., Onasch, T. B., Massoli, P., Croasdale, D. R., Wright, J. P., Ahern, A. T., Williams, L. R., Worsnop, D. R., Brune, W. H., and Davidovits, P. (2011b). Laboratory studies of the chemical composition and cloud condensation nuclei (CCN) activity of secondary organic aerosol (SOA) and oxidized primary organic aerosol (OPOA). *Atmospheric Chemistry and Physics*, 11(17):8913 – 8928.

Leone, J. A., Flagan, R. C., Grosjean, D., and Seinfeld, J. H. (1985). An outdoor smog chamber and modeling study of toluene – nox photooxidation. *International journal of chemical kinetics*, 17(2):177 – 216.

Liu, B., Pui, D., Whitby, K., Kittelson, D., Kousaka, Y., and McKenzie, R. (1978). The aerosol mobility chromatograph: a new detector for sulfuric acid aerosols. *Atmospheric Environment (1967)*, 12(1-3):99 – 104.

Loza, C. L., Coggon, M. M., Nguyen, T. B., Zuend, A., Flagan, R. C., and Seinfeld, J. H. (2013). On the mixing and evaporation of secondary organic aerosol components. *Environmental science & technology*, 47(12):6173 – 6180. http://pubs.acs.org/doi/pdf/10.1021/es400979k.

Mao, J., Ren, X., Brune, W. H., Olson, J. R., Crawford, J. H., Fried, A., Huey, L. G., Cohen, R. C., Heikes, B., Singh, H. B., Blake, D. R., Sachse, G. W., Diskin, G. S., Hall, S. R., and Shetter, R. E. (2009). Airborne measurement of OH reactivity during INTEX-B. *Atmospheric Chemistry and Physics*, 9(1):163 – 173.

Maricq, M. M. and Xu, N. (2004). The effective density and fractal dimension of soot particles from premixed flames and motor vehicle exhaust. *Journal of Aerosol Science*, 35(10):1251 – 1274.

Marjamäki, M., Keskinen, J., Chen, D.-R., and Pui, D. Y. (2000). Performance evaluation of the electrical low-pressure impactor (ELPI). *Journal of Aerosol Science*, 31(2):249 – 261.

Mikhailov, E., Vlasenko, S., Martin, S., Koop, T., and Pöschl, U. (2009). Amorphous and crystalline aerosol particles interacting with water vapor: conceptual framework and experimental evidence for restructuring, phase transitions and kinetic limitations. *Atmospheric Chemistry and Physics*, 9(24):9491 – 9522.

Miyakawa, T., Matsuzawa, R., Katayama, M., and Takegawa, N. (2013). Reconsidering adhesion and bounce of submicron particles upon high-velocity impact. *Aerosol Science and Technology*, 47(5):472 – 481.

Murphy, D., Cziczo, D., Froyd, K., Hudson, P., Matthew, B., Middlebrook, A., Peltier, R. E., Sullivan, A., Thomson, D., and Weber, R. (2006). Single-particle mass spectrometry of tropospheric aerosol particles. *Journal of Geophysical Research: Atmospheres (1984 – 2012)*, 111(D23):S32.

Myhre, G., D. S., Bréon, F.-M., W. Collins, J. F., Huang, J., Koch, D., Lamarque, J.-F., Lee, D., Mendoza, B., Nakajima, T., Robock, A., Stephens, G., Takemura, T., and Zhang, H. (2013). *Anthropogenic and Natural Radiative Forcing. In: Climate Change 2013: The Physical Science Basis. Contribution of Working Group I to the Fifth Assessment Report of the Intergovernmental Panel on Climate Change*. Cambridge University Press, Cambridge, United Kingdom and New York, NY, USA.

Ng, N. L., Canagaratna, M. R., Zhang, Q., Jimenez, J. L., Tian, J., Ulbrich, I. M., Kroll, J. H., Docherty, K. S., Chhabra, P. S., Bahreini, R., Murphy, S. M., Seinfeld, J. H., Hildebrandt, L., Donahue, N. M., DeCarlo, P. F., Lanz, V. A., Prévôt, A. S. H., Dinar, E., Rudich, Y., and Worsnop, D. R. (2010). Organic aerosol components observed in northern hemispheric datasets from aerosol mass spectrometry. *Atmospheric Chemistry and Physics*, 10(10):4625 – 4641.

Pajunoja, A., Malila, J., Hao, L., Joutsensaari, J., Lehtinen, K. E., and Virtanen, A. (2014). Estimating the viscosity range of SOA particles based on their coalescence time. *Aerosol Science and Technology*, 48(2):i – iv.

Perraud, V., Bruns, E. A., Ezell, M. J., Johnson, S. N., Yu, Y., Alexander, M. L., Zelenyuk, A., Imre, D., Chang, W. L., Dabdub, D., Pankow, J. F., and Finlayson-Pitts, B. J. (2012). Nonequilibrium atmospheric secondary organic aerosol formation and growth. *Proceedings of the National Academy of Sciences*, 109(8):2836 – 2841.

Power, R. M., Simpson, S. H., Reid, J. P., and Hudson, A. J. (2013). The transition from liquid to solid-like behaviour in ultrahigh viscosity aerosol particles. *Chem. Sci.*, 4:2597 – 2604.

Rader, D. and McMurry, P. (1986). Application of the tandem differential mobility analyzer to studies of droplet growth or evaporation. *Journal of Aerosol Science*, 17(5):771 – 787.

Renbaum-Wolff, L., Grayson, J. W., Bateman, A. P., Kuwata, M., Sellier, M., Murray, B. J., Shilling, J. E., Martin, S. T., and Bertram, A. K. (2013). Viscosity of α-pinene secondary organic material and implications for particle growth and reactivity. *Proceedings of the National Academy of Sciences*, 110(20):8014 – 8019.

Roberts, G. and Nenes, A. (2005). A continuous-flow streamwise thermal-gradient CCN chamber for atmospheric measurements. *Aerosol science and technology*, 39(3):206 – 221.

Robinson, A. L., Donahue, N. M., Shrivastava, M. K., Weitkamp, E. A., Sage, A. M., Grieshop, A. P., Lane, T. E., Pierce, J. R., and Pandis, S. N. (2007). Rethinking organic aerosols: Semivolatile emissions and photochemical aging. *SCIENCE*, 315(5816):1259 – 1262.

Romakkaniemi, S., Hämeri, K., Väkevä, M., and Laaksonen, A. (2001). Adsorption of water on 8-15 nm NaCl and (NH4)2SO4 aerosols measured using an ultrafine tandem differential mobility analyzer. *The Journal of Physical Chemistry A*, 105(35):8183–8188. http://pubs.acs.org/doi/pdf/10.1021/jp010647l.

Saleh, R., Donahue, N. M., and Robinson, A. L. (2013). Time scales for gas-particle partitioning equilibration of secondary organic aerosol formed from alpha-pinene ozonolysis. *Environmental Science & Technology*, 47(11):5588–5594. PMID: 23647198.

Seinfeld, J. and Pandis, S. (1998). *Atmospheric chemistry and physics: from air pollution to climate change*. Wiley New York, 2nd edition.

Shiraiwa, M., Ammann, M., Koop, T., and Pöschl, U. (2011). Gas uptake and chemical aging of semisolid organic aerosol particles. *Proceedings of the National Academy of Sciences*, 108(27):11003–11008.

Shiraiwa, M. and Seinfeld, J. H. (2012). Equilibration timescale of atmospheric secondary organic aerosol partitioning. *Geophysical Research Letters*, 39(24):n/a–n/a. L24801.

Shrivastava, M. K., Lane, T. E., Donahue, N. M., Pandis, S. N., and Robinson, A. L. (2008). Effects of gas particle partitioning and aging of primary emissions on urban and regional organic aerosol concentrations. *Journal of Geophysical Research: Atmospheres*, 113(D18):n/a–n/a. D18301.

Sipilä, M., Berndt, T., Petäjä, T., Brus, D., Vanhanen, J., Stratmann, F., Patokoski, J., Mauldin, R. L., Hyvärinen, A.-P., Lihavainen, H., and Kulmala, M. (2010). The role of sulfuric acid in atmospheric nucleation. *Science*, 327(5970):1243–1246.

Smith, M., Bertram, A., and Martin, S. (2012). Deliquescence, efflorescence, and phase miscibility of mixed particles of ammonium sulfate and isoprene-derived secondary organic material. *Atmospheric Chemistry and Physics*, 12(20):9613–9628.

Smith, M., Kuwata, M., and Martin, S. (2011). Secondary organic material produced by the dark ozonolysis of α-pinene minimally affects the deliquescence and efflorescence of ammonium sulfate. *Aerosol Science and Technology*, 45(2):244–261.

Takekawa, H., Minoura, H., Yasuda, A., et al. (2007). Construction and characterization of an atmospheric simulation smog chamber. *Advances in Atmospheric Sciences*, 24(2):250–258.

Vaden, T. D., Imre, D., Beránek, J., Shrivastava, M., and Zelenyuk, A. (2011). Evaporation kinetics and phase of laboratory and ambient secondary organic aerosol. *Proceedings of the National Academy of Sciences*, 108(6):2190–2195.

Vincent, J. (2012). *Structural biomaterials*. Princeton University Press.

Virtanen, A., Joutsensaari, J., Koop, T., Kannosto, J., Yli-Pirilä, P., Leskinen, J., Mäkelä, J., Holopainen, J., Pöschl, U., Kulmala, M., Worsnop, D. R., and Laaksonen, A. (2010). An amorphous solid state of biogenic secondary organic aerosol particles. *Nature*, 467(7317):824–827.

Zhang, Q., Jimenez, J. L., Canagaratna, M. R., Allan, J. D., Coe, H., Ulbrich, I., Alfarra, M. R., Takami, A., Middlebrook, A. M., Sun, Y. L., Dzepina, K., Dunlea, E., Docherty, K., DeCarlo, P. F., Salcedo, D., Onasch, T., Jayne, J. T., Miyoshi, T., Shimono, A.,

Hatakeyama, S., Takegawa, N., Kondo, Y., Schneider, J., Drewnick, F., Borrmann, S., Weimer, S., Demerjian, K., Williams, P., Bower, K., Bahreini, R., Cottrell, L., Griffin, R. J., Rautiainen, J., Sun, J. Y., Zhang, Y. M., and Worsnop, D. R. (2007). Ubiquity and dominance of oxygenated species in organic aerosols in anthropogenically-influenced Northern Hemisphere midlatitudes. *Geophysical Research Letters*, 34(13):L13801.

Zobrist, B., Marcolli, C., Pedernera, D. A., and Koop, T. (2008). Do atmospheric aerosols form glasses? *Atmospheric Chemistry and Physics*, 8(17):5221 – 5244.

Appendices

Publication I

A. Virtanen, J. Kannosto, H. Kuuluvainen, A. Arffman, J. Joutsensaari, E. Saukko, L. Hao, P. Yli-Pirilä, P. Tiitta, J. K. Holopainen, J. Keskinen, D. R. Worsnop, J. N. Smith, and A. Laaksonen. Bounce behavior of freshly nucleated biogenic secondary organic aerosol particles *Atmospheric Chemistry and Physics*, 11(16):8759–8766, 2011.

Atmos. Chem. Phys., 11, 8759–8766, 2011
www.atmos-chem-phys.net/11/8759/2011/
doi:10.5194/acp-11-8759-2011

Atmospheric Chemistry and Physics

Bounce behavior of freshly nucleated biogenic secondary organic aerosol particles

A. Virtanen[1], J. Kannosto[1], H. Kuuluvainen[1], A. Arffman[1], J. Joutsensaari[2], E. Saukko[1], L. Hao[2], P. Yli-Pirilä[3], P. Tiitta[2], J. K. Holopainen[3], J. Keskinen[1], D. R. Worsnop[2,4,5], J. N. Smith[2,6,7], and A. Laaksonen[2,4]

[1]Tampere University of Technology, Department of Physics, P.O. Box 692, 33101 Tampere, Finland
[2]University of Eastern Finland, Department of Applied Physics, P.O. Box 1627, 70211 Kuopio, Finland
[3]University of Eastern Finland, Department of Environmental Science, P.O. Box 1627, 70211 Kuopio, Finland
[4]Finnish Meteorological Institute, P.O. Box 503, 00101 Helsinki, Finland
[5]Aerodyne Research, Billerica, MA 08121-3976, USA
[6]Finnish Meteorological Institute, P.O. Box 1627, Kuopio, Finland
[7]National Center for Atmospheric Research, P.O. Box 3000, Boulder, CO 80307, USA

Received: 23 February 2011 – Published in Atmos. Chem. Phys. Discuss.: 21 March 2011
Revised: 12 August 2011 – Accepted: 23 August 2011 – Published: 26 August 2011

Abstract. The assessment of the climatic impacts and adverse health effects of atmospheric aerosol particles requires detailed information on particle properties. However, very limited information is available on the morphology and phase state of secondary organic aerosol (SOA) particles. The physical state of particles greatly affects particulate-phase chemical reactions, and thus the growth rates of newly formed atmospheric aerosol. Thus verifying the physical phase state of SOA particles gives new and important insight into their formation, subsequent growth, and consequently potential atmospheric impacts. According to our recent study, biogenic SOA particles produced in laboratory chambers from the oxidation of real plant emissions as well as in ambient boreal forest atmospheres can exist in a solid phase in size range >30 nm. In this paper, we extend previously published results to diameters in the range of 17–30 nm. The physical phase of the particles is studied by investigating particle bounce properties utilizing electrical low pressure impactor (ELPI). We also investigate the effect of estimates of particle density on the interpretation of our bounce observations. According to the results presented in this paper, particle bounce clearly decreases with decreasing particle size in sub 30 nm size range. The comparison measurements by ammonium sulphate and investigation of the particle impaction velocities strongly suggest that the decreasing bounce is caused by the differences in composition and phase of large (diameters greater than 30 nm) and smaller (diameters between 17 and 30 nm) particles.

Correspondence to: A. Virtanen
(annele.virtanen@tut.fi)

1 Introduction

Secondary aerosol formation via nucleation of precursor vapors and subsequent condensational growth has been reported to produce atmospheric aerosol in a variety of environments (e.g., Kulmala et al., 2004; Laaksonen et al., 2005). Numerous modelling studies (e.g., Spracklen et al., 2006) suggest that these particles are likely to have a significant impact on climate. The assessment of the climatic impacts and adverse health effects of atmospheric aerosol particles require detailed information on particle properties. Oxidation products of volatile organic compounds (VOC) emitted by sources such as vegetation participate in the formation and growth process of the newly formed atmospheric particles (Laaksonen et al., 2008, Kanakidou et al., 2005, Jimenez et al., 2009; Claeys et al., 2004). These are called secondary organic aerosols (SOA). Recent estimates on the importance of SOA formation show that it may be as significant as primary organic aerosol emissions, comprising about 60-70 % of the organic aerosol mass on the global scale and regionally even higher (Hallquist et al., 2009, Kanakidou et al., 2005). Furthermore, substantial formation of biogenic SOA takes place over the boreal forest in northern Europe, indicating that the forest is a major source of climate-relevant aerosol particles

Published by Copernicus Publications on behalf of the European Geosciences Union.

Table 1. Summary of plant chamber experiments. Values are determined at the beginning of trials (density during experiments ± standard deviation).

#	Experiment	VOC	O_3	SO_2	TME	RH	T	density
		(ppb)	(ppb)	(ppb)	(ppb)	(%)	(°C)	g cm^{-3}
1	Pine + O_3	16.8	35	–	–	34	22	1.00±0.06
2	Pine + OH + SO_2	107.6	35	22	35.2	31	22	1.10±0.07

(Tunved et al., 2006). SOA formation and properties are widely studied to clarify the role of SOA in radiative forcing and climate. In spite of their importance, the exact species and mechanisms that are responsible for the formation and growth of SOA is still not known. This is especially true for sub-30 nm diameter particles, for which the Kelvin effect predicts that a relatively small subset of available aerosol precursors participate in gas-particle partitioning due to their volatility.

It is well known that inorganic salts such as $NH_4(SO_4)_2$ and NaCl can be found in liquid droplets or solid crystals in the atmosphere depending on the surrounding humidity and temperature (e.g., Martin, 2000). However, very limited information is available on the morphology and phase state of SOA particles. According to our recent study, biogenic SOA particles produced in laboratory chambers from the oxidation of real plant emissions as well as in ambient boreal forest atmospheres can exist in a solid phase (Virtanen et al., 2010). In addition, the results of Cappa and Wilson (2011) indicate that the SOA particles formed through α-pinene ozonolysis might be in a solid amorphous state rather than liquid. The physical state of particles greatly affects chemical reactions in the particles, and thus the growth rates of newly formed atmospheric aerosol. For highly viscous and solid particles, chemical reactions are typically surface-limited (i.e., heterogeneous reaction on particle surfaces). Zobrist et al. (2008) and others (Murray 2008; Mikhailkov et al., 2009) also suggested that the water uptake of the particles is diminished or even fully inhibited for highly viscous or glassy aerosols. In gas-to-particle partitioning models developed for SOA particles, it is generally assumed that particles are in liquid state (Pankow, 1994; Odum et al., 1996). Thus verifying the physical phase state of SOA particles gives new and important insight into their formation and growth process and essential information on their atmospheric impacts.

The physical phase of the particles can be studied by investigating particle bounce properties (Virtanen et al., 2010). When an aerosol particle collides with an impaction surface, one part of its kinetic energy is dissipated in the deformation process, and another part is converted elastically into kinetic energy of rebound. If the rebound energy exceeds the adhesion energy, the particle will bounce from the surface. Thus both the elastic properties and surface properties of particles affect their bounce probability (Rogers and Reed, 1984). Relative humidity (RH) also affects the bounce probability as RH influences the viscoelastic properties of hygroscopic aerosol particles (Stein et al., 1994). Generally, harder materials, larger particles or greater impact velocity will lead to a higher bounce probability, although the roughness of the collecting surface also plays a significant role (Dahneke, 1971, Chang et al., 1991). In our recent paper (Virtanen et al., 2010) we showed that biogenic SOA particles bounce in impactor stages, indicating that the particles are solid in their physical phase. Based on electron diffraction analysis and bounce measurements of liquid, crystalline and amorphous solid laboratory-generated aerosol, we concluded that biogenic SOA particles larger than 30 nm in diameter are amorphous solids. In this paper, we extend these results to diameters in the range of 17–30 nm. Furthermore, we investigate the effect of estimates of particle density on the interpretation of our bounce observations.

2 Methods

2.1 Chamber experiments

The SOA experiments were performed at the Kuopio aerosol research chamber using living Scots pine trees as a natural source of VOCs. The experimental setup has been described in detail by Hao et al. (2009). Briefly, the system consists of a plant enclosure (fluorinated ethylene propylene (FEP) bag), a reaction chamber (made also of FEP film with a volume of 6 m^3), and gas and particle measurement systems that are described in greater detail below. All branches with green needles on a 10-yr-old Scots pine seedling were enclosed in an FEP bag, which was sealed on the stem bark. Plant-emitted VOCs were transported by purified and dried air into the separate reaction chamber in order to achieve the desired concentration of VOCs. To simulate herbivore attack on tree bark and to activate the chemical defence of seedlings, thereby enhancing VOC emissions, 1 cm long and 1 mm deep cuts were made on the base of the main stem by a knife.

Table 1 summarizes the experiments conducted in this research. The experiments are the same described in Virtanen et al. (2010). In experiment (#1) ozone-initiated chemistry was explored, whereas in experiment (#2) tetramethylethylene (TME) was added to the chamber to produce additional hydroxyl radicals (OH) and increase the OH:O_3 ratio (i.e.,

oxidation conditions) in the reaction chamber (Lambe et al., 2007). In experiment (#2) 1 ppm of SO_2 in nitrogen was also added to the chamber. After injecting the plant-derived VOCs, 700 ppb of ozone generated by a UV lamp O_3 generator was added to the chamber at a flow rate of 40 lpm for approximately 8 min. In all experiments, the temperature (T) was 22±1°C and relative humidity (RH) was controlled in the range of 30±5 % (measured with Vaisala Humidity and Temperature Probe HMP50). Ozone (DASIBI 1008-RS O_3 analyzers, Dasibi Environmental Corporation), NO_x (AC 30M NO_x analyzer Environment s.a.), SO_2 (AF21M SO_2 analyzer Environment s.a.) and VOC concentrations were measured inside the chamber during experiments. VOC samples were collected on Tenax-TA adsorbent and the samples were analyzed by gas chromatography-mass spectrometry (Vuorinen et al., 2004). The initial VOC concentrations inside the chamber before ozone addition were 18.8 ppb and 107.6 ppb for the ozone O_3 (exp. #1) and OH+SO_2 (exp. #2) experiments, respectively. To increase aerosol mass loading in the experiment (#1), two extra ozone injections were made at two hours after the first ozone addition.

The particle size distributions were measured by two scanning mobility particle sizers (SMPS) comprised of a Differential Mobility Analyzer (DMA; model 3081, TSI, Inc.) coupled to a condensation particle counter (CPC; model 3022, TSI, Inc.) and a nano DMA (model 3085, TSI, Inc.) coupled to a ultrafine CPC (model 3027, TSI, Inc.) with mobility diameter ranges of 10–700 nm and 3–60 nm, respectively. Furthermore, chemical composition and mass size distributions of aerosol particles formed during the experiments were measured with a quadrupole-based Aerosol Mass Spectrometer (AMS, Aerodyne Inc.). The average density of particles was determined by comparing the SMPS volume and AMS mass size distributions (De Carlo et al., 2004).

The size distributions and bounce behaviour of particles, which are related to particle physical phase state, were determined with an electrical low pressure impactor (ELPI). In ELPI, particles are charged by a unipolar corona charger and after the charger, the particles enter a twelve stage cascade impactor (Keskinen et al., 1992), where the particles are classified according to their aerodynamic size, depending on both the physical size and the density of the particle. In a conventional ELPI set-up, the cut size of the lowest stage is approximately 30 nm, however for these investigations the ELPI was equipped with an additional impactor stage with a cut-off size of 17 nm. In addition, a back-up filter was used to measure particles smaller than the lowest impactor cut-off size.

2.2 Particle bounce analysis

In the normal operation of a cascade impactor, particle bounce perturbs the measurement as larger particles are transferred to lower stages following bounce thus biasing the inferred size distribution towards smaller sizes. When particle bounce occurs in an ELPI, a significant excess current is measured in the lowest impactor stages resulting from the charges carried by the bounced particles.

Hence, particle bounce can be quantified by analyzing the difference in bounce-affected measured currents with ideal non-affected currents. To calculate the ideal currents the measured SMPS number distribution as a function of particle diameter, $n_{\mathrm{SMPS}}(d_p)$, is converted to ELPI current response $i^{\mathrm{id}}(d_p)$ by first multiplying the measured SMPS distribution by the ELPI charger efficiency curve, $E_{\mathrm{ch}}(d_p)$ (Ristimäki et al., 2002)

$$i^{\mathrm{id}}(d_p) = n_{\mathrm{SMPS}}(d_p) E_{\mathrm{ch}}(d_p) \quad (1)$$

Next, the resulting current distribution i^{id} is passed through the ELPI impactor kernel functions k_j to mimic the particle collection within the impactor (Ristimäki et al., 2002). The kernel functions are carefully calibrated for chosen impactor units and substrate types. The current in the j*th* impactor stage can be calculated from the following equation:

$$I_j^{\mathrm{id}} = \int_0^\infty k_j(d_p, \rho) i^{\mathrm{id}}(d_p) dd_p \quad (2)$$

Such calculations result in idealized ELPI currents. In the above calculations, the average particle density (ρ) is required. For pine derived SOA particles measured in the smog chamber we use densities obtained from AMS – SMPS measurements (density value of 1.1 g cm^{-3}). Note that the particle density was determined for particle diameters larger than 100 nm due to low mass loadings in the chamber and the low particle transmission efficiency of the AMS for particles smaller than 40 nm. In the following section we shall explore relationship between particle bounce observations and density for particles smaller than 100 nm in diameter.

When the measured and ideal currents are compared, the fraction of excess current in the back-up filter can be estimated. This fraction is called the bounce factor (Virtanen et al., 2010). In the measurements reported by Virtanen et al. (2010), the bounce factor was determined reliably only for particles having GMD larger than 30 nm. This was due to the fact that the lowest cut size of the impactor set-up used in atmospheric measurements was 30 nm. If the ELPI is equipped with additional impactor stage having cut-size 17 nm (Yli-Ojanperä et al., 2010), it is possible to extend the bounce characteristic investigations down to 17 nm according to (see also Fig. 1)

$$\text{bounce factor} \equiv \frac{I_{\mathrm{filter}} - I_{\mathrm{filter}}^{\mathrm{id}}}{\sum I_{\mathrm{impactor\ stages} \geq 17\,\mathrm{nm}}^{\mathrm{id}}}, \quad (3)$$

where I_{filter} is the current measured in back-up filter, $I_{\mathrm{filter}}^{\mathrm{id}}$ is the simulated ideal current in back up filter, and $\Sigma I_{\mathrm{impactor\ stages} \geq 17\,\mathrm{nm}}^{\mathrm{id}}$ is the sum of the ideal currents calculated from the impactor stages (excluding the back-up filter).

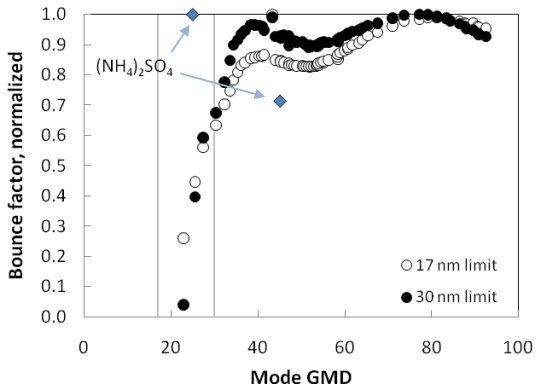

Fig. 1. Comparison of normalized bounce factors for measurements having 17 nm (open circles) and 30 nm (black dots) size limitations. In addition, reference measurements by ammonium sulphate particles are shown (blue diamonds).

Here the cut size of the last impactor stage is 17 nm. We would like to point out that the bounce factor defined by Eq. (3) does not depend only on particle bounce properties but also on the charge transfer properties of the particles.

In the following section, we present the results calculated by the Eq. (3), and compare them to the results published in Virtanen et al. (2010) where the bounce factors were calculated by utilizing the same data but using the 30 nm size limitations.

3 Results and discussion

For comparison, the normalized bounce factors for 17 and 30 nm size limits are shown in Fig. 1 for particles produced by the OH dominated oxidation of pine emitted VOCs (in presence of added SO_2 in the chamber). In Fig. 1, the bounce factors are calculated using the same data with two different size limitations, The results shown in Fig. 1 are calculated using particle density of 1.1 g cm^{-3} derived from the AMS-SMPS measurements and they are shown as a function geometric mean mobility diameter (GMD) of SMPS size distributions. It should be noted, that the absolute value of bounce factors for size limits 17 nm and 30 nm differs because in the 30 nm case, the bounce factor is calculated according to the equation presented in Virtanen et al. (2010) instead of Eq. (3). The size limits of 17 nm and 30 nm are marked with grey vertical lines in the figure. As can be seen, the particle bounce factor clearly decreases in size range below 30 nm.

The particle bounce data can be used to constrain the density of sub-30 nm diameter particles, for which little experimental data is available (Kannosto et al., 2008). In Fig. 2 we show the calculated bounce factor for data obtained with the 17 nm diameter size limit using density values varying from 0.8 g cm^{-3} to 2 g cm^{-3}. The results indicate that in spite of possible uncertainties in the density, the bounce of the sub 30 nm particles clearly decreases with decreasing particle size. In addition, the bounce factor for particles >40 nm is insensitive to the chosen density.

In the upper right corner of Fig. 2a and b, the results of the details in bounce factor values for the smallest particle sizes are shown. The zero value for bounce factor is marked with dashed line in the figure. As can be seen, the bounce factor gets clearly negative values when low density values are used in calculations. Underestimating the density in the calculations results in unrealistically high simulated current values in the back up filter compared to the measured currents (i.e., unrealistic high values of $I^{\mathrm{id}}_{\mathrm{filter}}$ in Eq. 3), thus the numerator in Eq. (3) gets negative values. The closer the investigated size is to the cut size of lowest impactor stage (in this case 17 nm) the more sensitive the calculated bounce factor is for the chosen density values. The estimated maximum uncertainty in the calculated bounce factor is ca. 10 % including the noise in current measurement and the uncertainty in current simulations (but excluding the effect of the density values used in calculations which is shown in Fig. 2a and b). It is clear that for all used density values the changes in bounce factor in sub 30 nm size range in Fig. 2a and b are significant compared to the uncertainty in the bounce factor calculations.

In the case of particles formed by ozonolysis of pine derived VOC in the absence of SO_2 (henceforth referred to as the "O_3 case"), the bounce factor achieved positive values for the smallest measured mobility diameter (18 nm) when the density used in calculations are greater than 1.3 g cm^{-3} (Fig. 2a). In the case of OH initiated oxidation in the presence of SO_2 (referred to as the "OH+SO_2 case"), the corresponding density value is 1.6 g cm^{-3} (Fig. 2b). This indicates that in the experiments with SO_2 (OH+SO_2 case), the density of the smallest particles is higher than in the absence of SO_2 (O_3 case). In Fig. 4a the ratio of SO_4^{2-} to organics measured by the AMS is shown for OH+SO_2 case. It can be seen that smaller particles contained higher amount of SO_4^{2-} than larger particles. On the other hand, particles formed through ozonolysis in absence of SO_2 contained no SO_4^{2-}. Densities of inorganic compounds containing SO_4^{2-} are typically higher compared to organic compounds, e.g., 1.84 g cm^{-3} for sulphuric acid and ca. 1.77 g cm^{-3} for ammonium sulphate (Lide, 1996). This can explain the differences in densities of the smallest particles in these two cases. When the density values analyzed for larger particles (50–100 nm) from AMS and SMPS distributions shown in Table 1, no clear differences are observed. As Fig. 4a shows, at these larger sizes the ratio of SO_4^{2-} to organic decreases and particles become more similar to pure SOA.

The higher density values needed to gain the positive bounce factor (calculated from Eq. 3) for the OH+SO_2 case could be explained also by the lower bounced fraction of

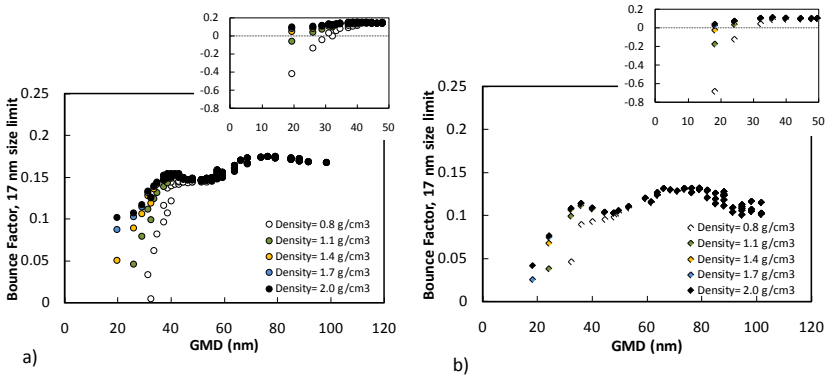

Fig. 2. Calculated bounce factors for the 17 nm size limit measured for **(a)** O_3 initiated oxidation in absence of SO_2 and **(b)** OH dominated oxidation in presence of SO_2. Density values varying from 0.8 g cm^{-3} to 2 g cm^{-3} were used in calculations. Insets in the upper right corners of **(a)** and **(b)** show details in bounce factor values for the smallest particles.

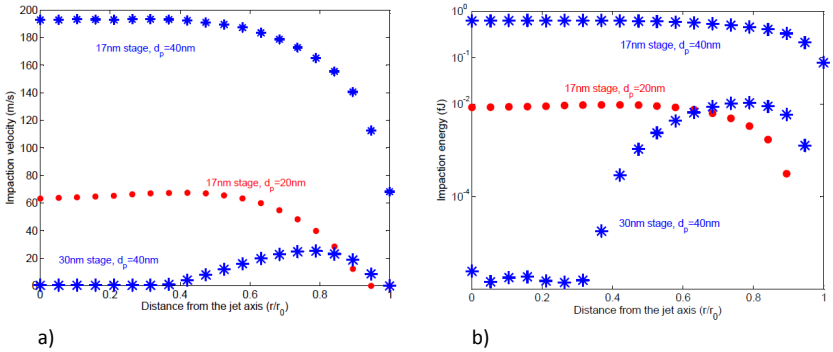

Fig. 3. (a) Calculated impaction velocities and **(b)** impaction energies for the 20 nm particles impacting for the first time on the stage having 17 nm cut size (red dots) and 40 nm particles (blue stars) impacting on the 30 nm stage and 17 nm stage.

these particles (i.e., the lower measured current value in the filter stage (I_{filter}) in Eq. 3) when compared to O_3 case. In fact, when the bounce factors in Fig. 2a and b are compared, it can be seen that the overall bounce factor for OH+SO_2 case is lower than for the O_3. According to our earlier work (Virtanen et al., 2010) the bounce factor measured for ammonium sulphate particles is clearly lower than for amorphous polystyrene or SOA particles. This could be due to the difference in elastic properties of crystalline and amorphous materials or in charge transfer characteristics of these materials. One conclusion that one may draw from our observations that the differences in bounce behaviour of the smallest (around 20 nm) particles in these two investigated cases are related to the SO_4^{2-} concentration in particles. The higher SO_4^{2-} fraction in smallest particles can result in higher density value of the particles or the lower bounce probability of the particles (or both of these). The effect of these differences can be seen in calculated bounce factors. The decrease of the SO_4^{2-} fraction in particles in OH+SO_2 case (Fig. 4a) with increasing particle size indicates also that the sulphate compounds play a key role in initial particle formation and the organics participate strongly on particle growth.

According to the results presented here, particle bounce clearly decreases with decreasing particle size. The decreasing bounce can be caused by two reasons. Firstly the decreasing bounce can be caused by the differences in composition and phase of larger (GMD >30 nm) and smaller (GMD 17–30 nm) particles. In Fig. 4a and b the ratio of mass of m44 to mass of total organics analyzed from AMS data, which is a measure of the oxidation state of the particulate organics, is shown as a function of the GMD of number distribution for the O_3 and OH+SO_2 experiments, respectively. It should be noted that the AMS composition data shown in Fig. 4 is presented as a function of GMD of

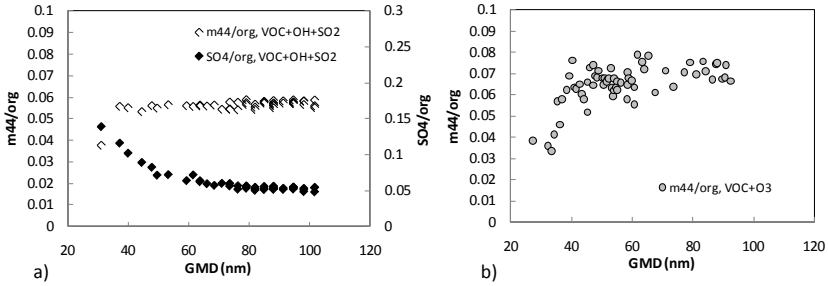

Fig. 4. $m44$/total organics ratio of particles derived from **(a)** OH initiated oxidation of the pine emitted VOCs, in the presence of SO_2, and **(b)** ozonolysis of the pine-emitted VOCs.

number distribution measured by SMPS. In the O_3 case, no SO_4^{2-} was detected in the AMS signal, as can be expected, but the particle oxidation degree of the smallest particles, as represented by the fraction of the m/z 44 fragment of the total organic mass concentration, is clearly lower than of the larger particles (Fig. 4b). A decreasing trend of $f44$ with decreasing particle size can be seen in Fig. 4b indicating strong possibility of similar trend also in the sub 30 nm size range. Hence we can assume that the fresher sub 30 nm particles are less oxidized than the larger particles. As a matter of fact, the lower oxidation degree of the smallest particles might be related to the "less solid" nature of the particles: it is known that the oligomers or other organic compounds with high molar mass are more prone to glass formation than smaller molecules (Zobrist et al., 2008). Hydrogen bonding between oxygenated compounds and functional groups may also favor the formation of solid phases (Mikhailov et al., 2009). According to Fig. 2, the fresher particles having GMD of 18 nm have clearly lower bounce factor than more aged particles having GMD of 30 nm. The time difference between these two measurements was approximately 15 minutes and the GMD 30 nm was measured approximately 25 min after the first particles were detected in the chamber. Thus, in these experimental conditions, we can make a rough approximation according to which the solidification takes place 10–25 min after the beginning of the nucleation process. The potential influence of oxidation and the age on the phase state of organic aerosol particles should be explored in future studies.

In the OH + SO_2 case, the measured fraction of particulate SO_4^{2-} increases with decreasing particles size but no clear changes in particle oxidation degree (f44) can be observed (Fig. 4a). As mentioned above, the bounce factor for OH+SO_2 case particles containing fraction of SO_4^{2-} is generally lower than bounce factor for O_3 case (no SO_4^{2-} in particles). According to our earlier laboratory experiments (Virtanen et al., 2010) the bounce factor measured for ammonium sulphate particles is clearly lower than for amorphous polystyrene or SOA particles. This could be due to the difference in elastic properties of crystalline and amorphous materials or in charge transfer characteristics of these materials. Hence the increasing fraction of SO_4^{2-} in smallest particles might also result in lowering bounce factor.

Secondly, it is important to note that with decreasing particle size the velocity needed for bounce to occur increases, since the required velocity is inversely proportional to particle size (Dahneke et al., 1971). On the other hand, 17–30 nm particles impact on the lowest impactor stage where the impactor jet velocities are generally higher than the jet velocities in the upper stage where, e.g., the 40 nm particle impacts for the first time. In addition, the contact velocities of particles impacting onto specific impactor stage depend on particle size: particles clearly larger than the cut point of the impaction stage have higher velocities than particles having size close to the cut point. We estimated the impaction velocities for 20 nm particles impacting the first time on the lowest impactor stage (having cut size 17 nm) and 40 nm particles impacting the first time on the upper stage (having cut size of 30nm) by using the modeling method presented by Arffman et al. (2011). As can be seen in Fig. 3a, where the impaction velocities of the particles are presented as a function of the radial distance from the center of the jet, the impaction velocities for 20 nm particles in the lowest impactor stage are higher on the average than impaction velocities of 40 nm particles on the upper stage. Impaction velocities of the 40 nm particles are higher at the edges of the jet, because the slip correction factor increases rapidly towards edges of the jet as discussed by Arffman et al. (2011). Most of the particles flow through the center parts of the impactor jet where the impaction velocities of the 20 nm particles are much higher than the impaction velocities of 40 nm particles at the upper stage. In addition, Fig. 3a shows the impaction velocity of 40 nm particles bouncing from the upper stage to the lowest stage. The impaction velocity increases as 40 nm particles travel from upper stage to the lowest stage resulting in higher bounce probability. We also calculated the kinetic energy of the particles by assuming density 1 g cm^{-3}. As can be seen in Fig. 3b, the kinetic energy of 20 nm particles at the lowest

stage (cut size 17 nm) is higher than the kinetic energy of the 40 nm particles impacting the upper stage (cut size 30 nm). These results indicate that the decreasing particle size does not explain the observed decrease in bounce factor in the sub 40 nm size range.

To further clarify the effect of particle size on bounce, reference measurements using solid 25 nm and 45 nm ammonium sulphate particles were performed. The measured bounce for 25 nm particles was higher than for 45 nm particles resulting the ratio of 1.4 for the bounce(25nm)/bounce(45 nm). We assume that the increase of bounce factor with decreasing particle size is due to both the increase in impaction energy (ref. Fig. 3) and the changes in charge transfer properties with particle size. The corresponding ratio for pine derived SOA particles is 0.53 (for the O_3 case) and 0.4 (for the $OH+SO_2$ case). Thus the behavior of bounce as a function of particle size is clearly different for solid ammonium sulphate particles and freshly nucleated pine derived SOA in sub 30 nm size range supporting the conclusion that the phase of newly formed sub 30 nm SOA particles is more liquid like than the phase of more aged larger particles.

4 Conclusions

The results reported here give information on the bounce characteristics (i.e., physical phase state) of smallest SOA particles produced by O_3 initiated oxidation and by OH dominated oxidation with SO_2 added in the chamber. Results strongly suggest that the decrease of bounce is caused by the differences in particle chemistry and their phase: the smaller (diameters between 17 and 30 nm) particles having lower oxidation degree or containing higher amount of SO_4^{2-} bounced less than larger (diameters greater than 30 nm) particles indicating different material characteristics in the case of fresher sub 30 nm size particles. The result might indicate that the initial nucleation process and growth of the newly formed particle is driven by mass transfer of molecules from gas phase to liquid phase. When particles are more aged, the solidification takes place and the partitioning process changes.

Acknowledgements. A. V. acknowledges the Maj and Tor Nessling Foundation for the financial support. J. J. acknowledges the support by the Academy of Finland (decision no. 110763, 111543, 131019, 218115 and Centre of Excellence Programme). J. S. acknowledges the financial support of the Saastamoinen foundation and the Office of Science (BER), US Department of Energy, grant DE-FG-02-05ER63997. The National Center for Atmospheric Research is sponsored by the US National Science Foundation.

Edited by: I. Riipinen

References

Arffman, A., Marjamäki, M., and Keskinen, J.: Simulation of low pressure impactor collection efficiency curves, J. Aerosol Sci., 42, 329–340, 2011.

Cappa, C. D. and Wilson, K. R.: Evolution of organic aerosol mass spectra upon heating: implications for OA phase and partitioning behavior, Atmos. Chem. Phys., 11, 1895–1911, doi:10.5194/acp-11-1895-2011, 2011.

Chang M., Kim, S., and Sioutas, C.: Experimental studies on particle impaction and bounce effects of substrate design and materials, Atmos. Environ., 33, 2313–2322, 1999.

Claeys M., Graham, B., Vas, G., Wang, W., Vermeylen, R., Pashynska, V., Cafmeyer, J., Guyon, P., Andreae, M. O., Artaxo, P., and Maenhaut, W.: Formation of secondary organic aerosols through photooxidation of isoprene, Science, 303, 1173–1176, 2004.

Dahneke, B.: Capture of aerosol particles by surfaces, J. Coll. Interface Sci. 37, 342–347, 1971.

De Carlo, P. F., Slowik, J. G., Worsnop, D. R., Davidovits, P., and Jimenez, J. L.: Particle morphology and density characterization by combined mobility and aerodynamic diameter measurements. Part 1: Theory, Aerosol. Sci. Technol., 38, 1185–1205, 2004.

Hallquist, M., Wenger, J. C., Baltensperger, U., Rudich, Y., Simpson, D., Claeys, M., Dommen, J., Donahue, N. M., George, C., Goldstein, A. H., Hamilton, J. F., Herrmann, H., Hoffmann, T., Iinuma, Y., Jang, M., Jenkin, M. E., Jimenez, J. L., Kiendler-Scharr, A., Maenhaut, W., McFiggans, G., Mentel, Th. F., Monod, A., Prévôt, A. S. H., Seinfeld, J. H., Surratt, J. D., Szmigielski, R., and Wildt, J.: The formation, properties and impact of secondary organic aerosol: current and emerging issues, Atmos. Chem. Phys., 9, 5155–5235, doi:10.5194/acp-9-5155-2009, 2009.

Hao, L. Q., Yli-Pirilä, P., Tiitta, P., Romakkaniemi, S., Vaattovaara, P., Kajos, M. K., Rinne, J., Heijari, J., Kortelainen, A., Miettinen, P., Kroll, J. H., Holopainen, J. K., Smith, J. N., Joutsensaari, J., Kulmala, M., Worsnop, D. R., and Laaksonen, A.: New particle formation from the oxidation of direct emissions of pine seedlings, Atmos. Chem. Phys., 9, 8121–8137, doi:10.5194/acp-9-8121-2009, 2009.

Jimenez., J. L., Canagaratna, M. R., Donahue, N. M., Prevot, A. S. H., Zhang, Q., Kroll, J. H., DeCarlo, P. F., Allan, J. D., Coe, H., Ng, N. L., Aikene, A. C., Docherty, K.S., Ulbrich, I.M., Grieshop, A. P., Robinson, A. L., Duplissy, J., Smith, J. D., Wilson, K. R., Lanz, V. A., Hueglin, C., Sun, Y. L., Tian, J., Laaksonen, A., Raatikainen, T., Rautiainen, J., Vaattovaara, P., Ehn, M., Kulmala, M., Tomlinson, J. M., Collins, D. R., Cubison, M. J., Dunlea, E. J., Huffman, J. A., Onasch, T. B., Alfarra, M. R., Williams, P. I., Bower, K., Kondo, Y., Schneider, J., Drewnick, F., Borrmann, S., Weimer, S., Demerjian, K., Salcedo, D., Cottrell, L., Griffin, R., Takami, A., Miyoshi, T., Hatakeyama, S., Shimono, A., Sun, J. Y., Zhang, Y. M., Dzepina, K., Kimmel, J. R., Sueper, D., Jayne, J. T., Herndon, S. C., Trimborn, A. M., Williams, L. R., Wood, E. C., Middlebrook, A. M., Kolb, C. E., Baltsenberger, U., and Worsnop, D. R.: Evolution of Organic Aerosols in the Atmosphere, Science, 326, 1525–1529, 2009.

Laaksonen, A., Kulmala, M., O'Dowd, C. D., Joutsensaari, J., Vaattovaara, P., Mikkonen, S., Lehtinen, K. E. J., Sogacheva, L., Dal Maso, M., Aalto, P., Petäjä, T., Sogachev, A., Yoon, Y. J., Lihavainen, H., Nilsson, D., Facchini, M. C., Cavalli, F., Fuzzi, S., Hoffmann, T., Arnold, F., Hanke, M., Sellegri, K., Umann, B.,

Junkermann, W., Coe, H., Allan, J. D., Alfarra, M. R., Worsnop, D. R., Riekkola, M.-L., Hyötyläinen, T., and Viisanen, Y.: The role of VOC oxidation products in continental new particle formation, Atmos. Chem. Phys., 8, 2657–2665, doi:10.5194/acp-8-2657-2008, 2008.

Lide, D. R. (Ed.): CRC handbook of chemistry and physics (77th ed.), Boco Raton, FL, USA, CRC Press, 1996.

Kanakidou, M., Seinfeld, J. H., Pandis, S. N., Barnes, I., Dentener, F. J., Facchini, M. C., Van Dingenen, R., Ervens, B., Nenes, A., Nielsen, C. J., Swietlicki, E., Putaud, J. P., Balkanski, Y., Fuzzi, S., Horth, J., Moortgat, G. K., Winterhalter, R., Myhre, C. E. L., Tsigaridis, K., Vignati, E., Stephanou, E. G., and Wilson, J.: Organic aerosol and global climate modelling: a review, Atmos. Chem. Phys., 5, 1053–1123, doi:10.5194/acp-5-1053-2005, 2005.

Kannosto, J., Virtanen, A., Lemmetty, M., Mäkelä, J. M., Keskinen, J., Junninen, H., Hussein, T., Aalto, P. P., and Kulmala, M.: Mode resolved density of atmospheric aerosol particles, Atmos. Chem. Phys., 8, 5327–5337, doi:10.5194/acp-8-5327-2008, 2008.

Kulmala, M., Vehkamäki, H., Petäjä, T., Dal Maso, M., Lauri, A., Kerminen, V.-M., Bilmili, W., and McMurry, P.: Formation and growth rates of ultrafine atmospheric aerosol particles: a review of observations, J. Aerosol Sci., 35, 143–176, 2004.

Laaksonen, A., Hamed, A., Joutsensaari, J., Hiltunen, L., Cavalli, F., Junkermann, W., Asmi, A., Fuzzi, S., and Facchini, M. C.: Cloud condensation nuclei production from nucleation events at a highly polluted region, Geophys. Res. Lett., 32, L06812, doi:10.1029/2004GL022092, 2005.

Lambe, A. T., Zhang, J. Y., Sage, A. M., and Donahue, N. M.: Controlled OH radical production via ozone-alkene reactions for use in aerosol aging studies, Environ. Sci. Technol., 41, 2357–2363, 2007.

Martin, S.: Phase transitions of aqueous atmospheric particles, Chem. Rev., 100, 3403–3453, 2000.

Mikhailov, E., Vlasenko, S., Martin, S. T., Koop, T., and Pöschl, U.: Amorphous and crystalline aerosol particles interacting with water vapor: conceptual framework and experimental evidence for restructuring, phase transitions and kinetic limitations, Atmos. Chem. Phys., 9, 9491–9522, doi:10.5194/acp-9-9491-2009, 2009.

Murray, B. J.: Inhibition of ice crystallisation in highly viscous aqueous organic acid droplets, Atmos. Chem. Phys., 8, 5423–5433, doi:10.5194/acp-8-5423-2008, 2008.

Odum, J. R., Hoffmann, T., Bowman, F., Collins, D., Flagan, R. C., and Seinfeld, J. H.: Gas/particle partitioning and secondary organic aerosol yields, Environ. Sci. Technol., 30, 2580–2585, 1996.

Pankow, J. F.: An absorption model of the gas/aerosol partitioning involved in the formation of secondary organic aerosol, Atmos. Environ., 28, 189–193, 1994.

Ristimäki, J., Virtanen, A., Rostedt, A., and Keskinen, J.: On-line measurement of size distribution and effective density of submicron aerosol particles, J. Aerosol Sci. 33, 1541–1557, 2002.

Rogers, L. N. and Reed, J.: The adhesion of particles indergoing elastic-plastic impact with a surface, J. Phys. D, 17, 677–689, 1984.

Spracklen, D., Carslaw, K., Kulmala, M., Kerminen, V.-M., Mann, G., and Sihto, S.-L.: The contribution of boundary layer nucleation events to total particle concentrations on regional and global scales, Atmos. Chem. Phys., 6, 5631–5648, doi:10.5194/acp-6-5631-2006, 2006.

Stein, S. W., Turpin, J. B., Cai, X., Huang, P. F., and McMurry, P. H.: Measurements of relative humidity dependent bounce and density for atmospheric particles using DMA-impactor technique, Atmos. Environ., 28, 1739–1746, 1994.

Tunved, P., Hansson, H.-C., Kerminen, V.-M., Ström, J., Dal Maso, M., Lihavainen, H., Viisanen, Y., Aalto, P. P., Komppula, M., and Kulmala, M.: High Natural Aerosol Loading over Boreal Forests, Science, 312, 261–263, 2006.

Virtanen, A., Joutsensaari, J., Koop, T., Kannosto, J., Yli-Pirilä, P., Leskinen, J., Mäkelä, J. M., Holopainen, J. K., Pöschl, U., Kulmala, M., Worsnop, D. R., and Laaksonen, A.: An amorphous solid state of biogenic secondary organic aerosol particles, Nature, 467, 824–827, 2010.

Vuorinen, T., Nerg, A. M., Ibrahim, M. A., Reddy, G. V. P., and Holopainen, J. K.: Emission of Plutella xylostella-induced compounds from cabbages grown at elevated CO2 and orientation behavior of the natural enemies, Plant Physiol., 135, 1984–1992, 2004.

Yli-Ojanperä, J., Kannosto, J., Marjamäki, M., and Keskinen, J.: Improving the Nanoparticle Resolution of the ELPI, Aerosol Air Qual. Res., 10, 360–366, 2010.

Zobrist, B., Marcolli, C., Pedernera, D. A., and Koop, T.: Do atmospheric aerosols form glasses?, Atmos. Chem. Phys., 8, 5221–5244, doi:10.5194/acp-8-5221-2008, 2008.

Publication II

Kuuluvainen, A. Arffman, E. Saukko, A. Virtanen, and J. Keskinen A new method for characterizing the bounce and charge transfer properties of nanoparticles *Journal of Aerosol Science*, 55:104–115, 2013.

Journal of Aerosol Science 55 (2013) 104–115

Contents lists available at SciVerse ScienceDirect

Journal of Aerosol Science

journal homepage: www.elsevier.com/locate/jaerosci

A new method for characterizing the bounce and charge transfer properties of nanoparticles

Heino Kuuluvainen [a,*], Anssi Arffman [a], Erkka Saukko [a], Annele Virtanen [b], Jorma Keskinen [a]

[a] Aerosol Physics Laboratory, Department of Physics, Tampere University of Technology, Tampere, Finland
[b] Department of Applied Physics, University of Eastern Finland, Kuopio, Finland

ARTICLE INFO

Article history:
Received 14 June 2012
Received in revised form
28 August 2012
Accepted 28 August 2012
Available online 3 September 2012

Keywords:
Bouncing
Charge transfer
Nanoparticle
Impactor
ELPI

ABSTRACT

Bouncing and charge transfer between a particle and a surface are fundamental phenomena in aerosol physics. In this study, a new method is presented for characterizing these phenomena in the nanometer size range. The method is based on electrical detection of particles and on a new manner to exploit an electrical low pressure impactor (ELPI). By measuring particles with and without the charger, bouncing and charge transfer can be distinguished. To connect the measurement with the existing theoretical knowledge, a new model describing the bouncing and charge transfer behavior in a cascade impactor is presented. The model is linked to measurements through a fitting process which provides theoretical parameters for polydisperse nanoparticles. With this method, the bouncing and charge transfer of nanoparticles can be described by the existing theory of micrometer-sized particles. To demonstrate the performance of the method in practice, measurements were carried out to define the parameters for sodium chloride and levoglucosan particles.

1. Introduction

Nanoparticles are of interest in many fields of aerosol physics. Present research of aerosol synthesis, atmospheric aerosols, traffic related aerosols and their health effects is focused on ultrafine particles, i.e. particles below 100 nm (Kittelson et al., 2004; Kruis et al., 1998; Kulmala et al., 2004). It is well known that the properties of nanoparticles can differ significantly from those of larger aerosol particles and, in general, all the knowledge should be confirmed before applying it to nanoscale. In that sense, the interaction between a nanoparticle and a surface is rather poorly understood, especially considering the phenomena of particle bouncing and charge transfer.

Motivation to study the bouncing of aerosol particles has often been in means to prevent or reduce it. There are several studies focused on impactors and filters where particle bouncing is an undesirable phenomenon (e.g. Chang et al., 1999; Fujitani et al., 2006; Mullins et al., 2003). Charge transfer is a side effect of bouncing when a particle is in a contact with different surface material. Charge transfer has been studied as a fundamental phenomenon (John, 1995; John et al., 1980) and within some medical inhalator applications, in which the role of contact charging is significant (Matsusaka et al., 2010; Watanabe et al., 2007). Common for both bouncing and charge transfer is that experimental studies are practically restricted to particle sizes over one micrometer. In spite of the experimental challenges and the lack of interest from the perspective of medical inhalators in the nanometer size range, a few studies have recently been published related to

* Corresponding author.
E-mail address: heino.kuuluvainen@tut.fi (H. Kuuluvainen).

0021-8502/$ - see front matter © 2012 Elsevier Ltd. All rights reserved.
http://dx.doi.org/10.1016/j.jaerosci.2012.08.007

the bouncing and charge transfer of nanometer-sized particles. Weber & Wu (2009) defined yield points for particle materials by measuring the charge transfer of spherical metal nanoparticles. Furthermore, recent fragmentation studies of nanoparticle agglomerates are closely related to particle bouncing (Froeschke et al., 2003; Seipenbusch et al., 2007).

Recently, an electrical low pressure impactor (ELPI) was used in a totally new manner to indicate an amorphous solid state of secondary organic aerosol particles (Virtanen et al., 2010). The method was based on particle bouncing in the impactor. The ELPI, originally developed by Keskinen et al. (1992), is a commercially available measuring device, in which particles are charged in a corona charger and led to a cascade impactor. The device is capable of measuring an aerosol size distribution in the size range of 7 nm to 10 μm. In the normal operation of an ELPI, particles are collected on impactor substrates and a current signal is measured at each impactor stage connected to an electrometer. However, if particles are bouncing in the impactor, apparent changes can be observed in the measured current distribution compared to the ideal case of non-bouncing particles.

A concept of bounce factor was defined to quantify the amount of bounce in an ELPI (Virtanen et al., 2010, 2011). The factor is calculated simply from the extra current measured at the lowest impactor stage or filter stage, and it should represent the ratio of the current transferred by bounced particles to the ideal current of non-bouncing particles. However, the problem is that the factor does not take into account possible charge transfer nor the precise characteristics of a low pressure cascade impactor. More recently, Kannosto et al. (accepted) were able to define a lower limit for the bouncing probability of particles by taking into account possible charge transfer in a simplified manner. Although the procedure was based only on the measurements of secondary organic aerosol particles with an ELPI equipped with greased substrates, the bounce probability represented the real fraction of bounced particles at a single impactor stage. However, in this respect, it is more accurate and more applicable to use a single stage impactor and an optical measurement of particle concentration. Saukko et al. (2012) introduced a method of this kind, naming the corresponding bounce probability as bounced fraction. Principally, this method is a very good means to measure particle bounce with similar conditions for all particles, but it practically requires a monodisperse aerosol sample. In this work, the analysis of bouncing and charge transfer rests upon previous theoretical knowledge. The theoretical knowledge of particles over one micrometer is applied in the nanometer size range. The contact charge in charge transfer and the capture limit velocity of bouncing are even more profound concepts than bounce probability in the case of a single stage impactor. Through a new model and a principle of measurement introduced in this work, the measurement of a polydisperse aerosol sample with an ELPI can be connected to these concepts.

Using an ELPI or another instrument based on electrical measurement of particles in bouncing and charge transfer measurements, there is especially one question that should be settled. That is how to distinguish the phenomena of bouncing and charge transfer from each other. In this work, the key to the solution is that particles are measured with two different preliminary states of charge. Simply by calculating the difference of the two measured currents, the fraction of bounced particles can be seen. This simple principle of measurement is the basis of this study but it will also be accompanied with a fundamental theoretical analysis and modeling of the instrument behavior.

For the further analysis, a new model for bouncing particles and charge transfer in an ELPI is presented. The model is based on previous theories of bouncing and charge transfer (Dahneke, 1971; John et al., 1980) and on a recent flow field model of a low pressure impactor (Arffman et al., 2011). The aim of the bouncing and charge transfer model is to calculate the theoretical output of the instrument starting from an aerosol size distribution and parameters describing the bounce and charge transfer properties of particles. Finally, when measurements with an ELPI and with a scanning mobility particle sizer (SMPS) are performed simultaneously, the bounce and charge transfer properties of nanoparticles can be defined by fitting the modeled currents to the measured ELPI currents.

2. Theoretical background

2.1. Bouncing

There are three elements that affect the process when an aerosol particle collides with a surface. Those three elements are adhesion, the initial velocity of the particle and energy loss mechanisms in the collision. Assuming a spherical particle and an infinite smooth surface, the adhesion energy between the particle and the surface can be written as (Dahneke, 1971)

$$E_{\mathrm{adh}} = \frac{A d_{\mathrm{p}}}{12 z_0}, \tag{1}$$

where d_{p} is the particle diameter, A is Hamaker constant and z_0 is the separation distance usually assumed to be 0.4 nm. Hamaker constant is dependent on both particle and surface materials. It arises from the van der Waals interaction of molecules and can be calculated theoretically using Lifshitz theory (Bergström, 1997).

The relation between the initial velocity of the particle v_{i}, perpendicular to the surface, and the rebound velocity of the particle v_{r} is called coefficient of restitution,

$$C_{\mathrm{R}} = \frac{v_{\mathrm{r}}}{v_{\mathrm{i}}}, \tag{2}$$

and it represents the amount of energy losses in the collision. The smaller the value of C_R, the more energy is lost during the impaction and rebound. In practice, there are several different energy loss mechanisms in the case of an aerosol particle and a firm surface, but the most important is the plastic deformation of the particle. Particle bouncing was studied in more detail from the aspect of plastic and elastic deformation by Rogers & Reed (1984).

Because of the energy losses and relatively large adhesion energies arising from the area-to-mass ratio, aerosol particles do not usually bounce after a contact to a surface but they tend to adhere. According to Hinds (1999), this is one of the characteristics that distinguishes aerosol particles from gas molecules. However, if the initial velocity of a particle is large enough, its kinetic energy after the contact may suffice to overcome the adhesion energy resulting particle bounce. For the initial velocity, there is a certain capture limit v_i^*, which can be derived from the Eqs. (1) and (2) by setting the rebound kinetic energy equal to the adhesion energy. This was done by Dahneke (1971) and the result is

$$v_i^* = \frac{\alpha}{d_p}, \tag{3}$$

where the material coefficient of bouncing

$$\alpha = \left(\frac{A(1-C_R^2)}{\pi z_0 \rho_p C_R^2}\right)^{1/2}, \tag{4}$$

is dependent on the coefficient of restitution, Hamaker constant and particle density ρ_p. Thus, according to the theory, the capture limit is inversely proportional to particle diameter. Note also the dependency on particle density: $\alpha \propto 1/\sqrt{\rho_p}$. John (1995) collected results from several experimental studies in the micrometer size range showing that the value of the product $v_i^* d_p$ spanned approximately an order of magnitude for different particle and surface materials, corresponding α values between 10^{-6} and 10^{-5} m^2/s. Cheng & Yeh (1979) introduced a semi-empirical relationship for the capture limit in an impactor,

$$v_i^* d_p \sqrt{\frac{\rho_p}{\rho_0}} = B \times 10^{-6}\ \mathrm{m^2/s}, \tag{5}$$

where ρ_0 is the unit density and B ranges from 2.5 to 9.2 depending on the particle and surface materials and the type of the impactor. In this representation, material coefficient $\alpha = (B \times 10^{-6}\ \mathrm{m^2/s})/\sqrt{\rho_p/\rho_0}$.

2.2. Charge transfer

Charge transfer between a particle and a surface is a triboelectric phenomenon, in which electrons are transferred due to the properties of different materials. From the point of view of a particle, the process can also be called as contact charging or triboelectrification. The difference between these two terms may not always be recognized but, for example, Bailey (1984) considered the triboelectrification as more general than contact charging, because it includes sliding/frictional contact. A theoretical approach to the phenomenon, supported by extensive experimental data in the micrometer size range, was introduced by John et al. (1980). Starting from the elasticity theory of Hertz, they derived theoretical equations for a spherical particle and a smooth surface. The charge transfer process was divided into two parts, one depending on the material properties and particle size, and another depending on the particle precharge. As a result, the total charge transferred in the contact could be written as

$$q_{tot} = q_c + \beta q_0, \tag{6}$$

where q_c is the contact charge, q_0 is the precharge and β is a constant describing precharge sensitivity of the process. All the details of the theory are not presented here, but one equation is important related to this work. That is the final form of the equation of contact charge for insulating particle materials. According to John et al. (1980),

$$q_c = \frac{0.3675\pi V_c}{z_0 K \varrho}\left(\frac{5}{4}\pi^2 \rho_p (k_p + k_s)\right)^{4/5} v_i^{3/5} d_p^3, \tag{7}$$

where V_c is the contact potential between the particle and surface materials, K is the dielectric constant, ϱ is the resistivity, k_p is the elasticity parameter of particle material, k_s is the elasticity parameter of surface material and v_i is the impact velocity. Note that q_c is proportional to $\rho_p^{4/5}$.

The theoretical dependencies were confirmed and parameter values for different materials were defined in the experiments also performed by John et al. (1980). In the measurements, a single stage impactor and aerosol particles from 3 to 7 μm were used. They found that contact charge was dependent on substrate material but the substrate did not significantly affect the value of β. For methylene blue particles the average value of β was 0.043 ± 0.009, for potassium biphthalate 0.036 ± 0.016 and for sodium chloride 0.42 ± 0.05. Theoretically, contact charge is proportional to particle diameter raised to the power of two for conducting materials and raised to the power of three for insulating materials. As an example, John et al. (1980) measured for sodium chloride particles on a steel substrate a size dependency of $q_c = 124 \times d_p^{2.45}$, where d_p is in micrometers and the unit of the result is elementary charge. They used an impact velocity

of 50 m/s. In this work, the size dependency of contact charge is formulated as

$$q_c(d_p) = \frac{q_{c,0}}{d_{p,0}^{b_c}} \cdot d_p^{b_c}, \tag{8}$$

where b_c is the power of the dependency and $q_{c,0}$ is the contact charge for a certain particle size $d_{p,0}$. In addition to size dependency, contact charge is also dependent on impact velocity v_i. John et al. (1980) noticed in the experiments that contact charge is directly proportional to impact velocity, although the theory would predict q_c being proportional to $v_i^{3/5}$. In this work, for a certain particle size, the dependency is formulated as

$$q_c(v_i) = \frac{q_{c,0}}{v_{i,0}} v_i, \tag{9}$$

where $q_{c,0}$ is the contact charge for a certain impact velocity $v_{i,0}$.

2.3. Impaction velocities

In an experimental analysis of particle bouncing, it is essential to quantify the impaction velocities of particles. There are some methods based on direct measurement such as laser doppler velocimetry, which was used for example by Wall et al. (1990) for particles over one micrometer, and high speed cameras which can be used for macroscopic spheres. Nevertheless, none of these methods are directly applicable for nanometer-sized particles. First steps in applying optical velocity measurement for nanoparticles were taken by Reuter-Hack et al. (2007). They used "transparent" agglomerates of low fractal dimension, which have optical size adequate for optical detection but are aerodynamically much smaller.

Besides the challenging experimental methods, another means is to use flow field modeling. Impaction velocities can be defined by modeling the flow field in impactors and calculating the trajectories of particles. Recently, Arffman et al. (2011) published a flow field model of a low pressure impactor, in which the flow field was solved with a commercial CDF modeling software and particle trajectories were defined using Lagrangian methods. The study was focused on calculating the collection efficiency curves but the model is applicable also in predicting impaction velocities. When calculating collection efficiency curves, particles are considered to impact when they have a velocity component perpendicular to the surface close to the impaction plate.

In this work, the model of Arffman et al. (2011) for ELPI is exploited in quantifying impaction velocities with a semi-empirical approach. First of all, the impaction velocities were calculated with the model for several impactor stages and for several particle sizes. This information was combined with the known impactor pressures and the impaction velocity profiles, i.e. impaction velocities as a function of radial distance from the center of the jet, were defined for the cut-off particle sizes of all the impactor stages. The results of the model were also used to generate a functional form for the size dependency of impaction velocity. The final form is

$$v_{i,n}(d_a) = v_{j,n} - \frac{d_{50,n}(v_{j,n} - v_{50,n})}{d_a}, \tag{10}$$

where d_a is the aerodynamic particle diameter, $v_{j,n}$ is the jet velocity, $d_{50,n}$ is the cut-off size and $v_{50,n}$ is the velocity from the velocity profile of the cut-off size, all of which are defined for a stage n. The impaction velocities are seen in Fig. 1 as a function of radial distance from the center of the jet, r, and as a function of particle diameter for the 2nd impactor stage of an ELPI.

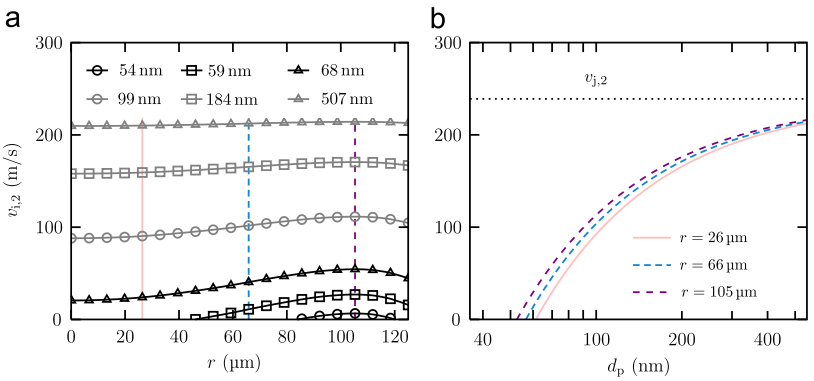

Fig. 1. Impaction velocities $v_{i,2}$ (a) for different particle sizes as a function of radial distance from the center of the impactor jet, r and (b) for three different radial distance as a function of particle size at the 2nd stage of an ELPI. The cut-off size of the stage is 55 nm, the radius of the jet 120 μm and the flow velocity in the jet 239 m/s.

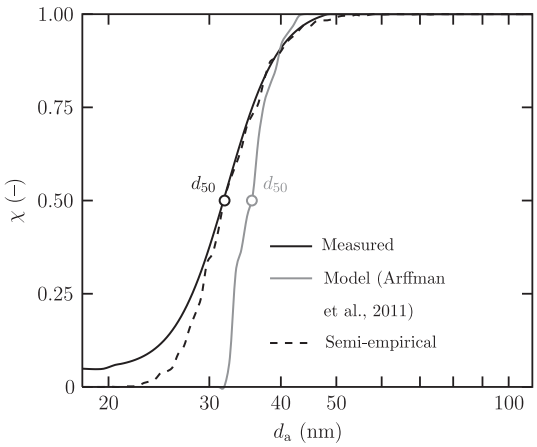

Fig. 2. Collection efficiency χ of the 1st stage of an ELPI as a function of aerodynamic particle size. The semi-empirical approach of adjusting the impaction velocities of the model provides a more realistic cut-off curve than the pure model.

The semi-empirical approach means that the impaction velocities were adjusted to correspond with the experimental collection efficiency curves by determining a certain cut-off size for each impactor stage and adding random noise to the velocities. The latter can also be justified physically because the pure model does not take account the effect of turbulent diffusion on impact velocities. Fig. 2 shows an example of this adjusting for the 1st impactor stage of an ELPI. The collection efficiency calculated by the model of Arffman et al. (2011) is sharper than the measured collection efficiency and the cut-off size is slightly different. In the semi-empirical approach, calculated impaction velocity profiles are moved either towards smaller or towards larger particle size, so that the cut-off size d_{50} matches with the experimental collection efficiency curve. Finally, random noise of 15% is added to the impaction velocity profiles in order to achieve more realistic shape for the collection efficiency curve. Because of the variation caused by the randomness, a set of 100 different cases and averaging are used.

3. Method description

Electrical detection of particles is problematic in measuring particle bouncing and charge transfer. For example, by measuring a current signal from a single impactor stage, it is practically impossible to distinguish the current caused by impacted particles from the current caused by bounced particles and charge transfer. In addition, if the amount of transferred charge is not known, the state of charge of bounced particles continuing to further measurements remains unknown. In this work, this problem is solved with a new approach, which includes a theoretical assumption and a principle of measurement. The theoretical assumption is that the parameter β can be approximated as zero, i.e. the amount of transferred charge is not dependent on the precharge of a particle. And further, the principle of measurement states that by measuring particles with two different preliminary states of charge, the fraction of bounced particles can be seen from the difference of the measured currents.

In practice, the experimental part of the method introduced in this work consists of two current distribution measurements with an ELPI. The first $I_{ch,on}$ is measured with the charger and the other $I_{ch,off}$ is measured without the charger. Thus, the initial charge distribution of the particles is described either by the charging efficiency curve of the ELPI charger or by the equilibrium charge distribution of net neutral particles. In both cases, it is enough to use the average number of charges per particle as an estimate of the charge distribution, which in the latter case is simply zero. Assuming $\beta \approx 0$, it is possible to eliminate the effect of charge transfer on the current distribution by calculating the difference of the two measured currents. In this study, so-called bounce current is defined

$$I_b = I_{ch,on} - I_{ch,off}, \tag{11}$$

which now represents the fraction of bounced particles, i.e. the current distribution in the case no charge transfer occurs.

Only by measuring $I_{ch,on}$ and $I_{ch,off}$ with an ELPI, the bounce current can be defined and analyzed further. For instance, the bounce factor analysis used by Virtanen et al. (2010, 2011) is now exploitable for a current distribution that is not disturbed by charge transfer. However, the bounce factor analysis still includes some problems such as changes in the particle size and density, which can affect the final bounce factor value even if the ability to bounce would stay unchanged. Another weakness of the bounce factor analysis is that it does not provide any absolute information comparable to fundamental theories or other studies. Consequently, this study focuses on a more profound method, but it is good to remember that the bounce factor analysis together with the defined bounce current provides a simple and approximate

on-line method for bouncing measurement. The more profound method introduced in this work is based on a size distribution measurement with an SMPS together with the ELPI measurement and calculation of bounce current. The idea is to simulate the measured ELPI current distributions starting from a size distribution by modeling the bounce and charge transfer behavior of incoming particles in an ELPI. The simulated current distributions are dependent on the theoretical parameters of bouncing and charge transfer and through a fitting process the values of these parameters can be defined.

4. Model

A new model describing the bounce and charge transfer behavior of nanoparticles in an ELPI is presented here. As an input for the model, there are incoming aerosol distribution in the form of mobility size distribution, effective density of the incoming particles and parameters of bouncing and charge transfer describing the particle–surface interaction. Effective density is required to convert particle mobility size to aerodynamic size and vice versa. The relation between these two size metrics is

$$\rho_{\mathrm{eff}} C_{\mathrm{C}}(d_{\mathrm{b}}) d_{\mathrm{b}}^2 = \rho_0 C_{\mathrm{C}}(d_{\mathrm{a}}) d_{\mathrm{a}}^2, \tag{12}$$

where d_{b} is the mobility diameter, d_{a} the aerodynamic diameter, C_{C} the slip correction factor and ρ_{eff} the effective density. In this work, the mobility diameter d_{b} is identified with the particle diameter d_{p} used in the bouncing and charge transfer model. The output of the model is the same as the output of the instrument in measurements including current distributions with and without the charger, $I_{\mathrm{ch,on}}$ and $I_{\mathrm{ch,off}}$, respectively. In addition, the bounce current derived from these by Eq. (11) plays an important role in comparing the model and measurements.

To obtain an idea of the model and its operation, it is reasonable to explain the process at a single impactor stage in detail. There are a few factors that play an important role in the process. Those are the collection efficiency curve of the impactor stage, bouncing probability and the charge distribution of the incoming particles. As an example, the collection efficiency χ of the second stage of an ELPI and the corresponding bouncing probability $P_{\mathrm{b},2}$, calculated with the help of impaction velocities and Eq. (3), are illustrated in Fig. 3. When a particle distribution $f_n(d_{\mathrm{b}},\rho_{\mathrm{eff}})$ with a certain particle density enters the stage n, it is straightforward to calculate the part of the distribution $f_{\mathrm{i},n}$ that impacts and another part $f_{\mathrm{b},n}$ that bounces after the impact, i.e. $f_{\mathrm{i},n} = \chi_n(d_{\mathrm{a}}) f_n(d_{\mathrm{b}},\rho_{\mathrm{eff}})$ and $f_{\mathrm{b},n} = P_{\mathrm{b},2}(d_{\mathrm{b}}) f_{\mathrm{i},n}$ (or $f_{\mathrm{b},n} = P_{\mathrm{b},2}(d_{\mathrm{p}}) f_{\mathrm{i},n}$). Finally, the part that remains at the impactor stage is

$$f_{\mathrm{f},n} = f_{\mathrm{i},n} - f_{\mathrm{b},n}, \tag{13}$$

and the part that continues to the next stage, f_{n-1}, is the complement of the latter.

The last procedure at a single stage is to calculate the output of the model, i.e. current signal caused by the impacted and bounced particles. The charge distribution of the incoming particles is an essential part of the preliminary information required in the procedure. As mentioned earlier, the charge distribution $g_n(d_{\mathrm{b}})$ entering the stage n is initially either zero or equal to the charging efficiency curve of the ELPI charger. Charging efficiency of the ELPI charger is often presented as a function of particle mobility size in the form (Marjamäki et al., 2002)

$$Pn = \begin{cases} 222.49 \times d_{\mathrm{b}}^{1.3637}, & d_{\mathrm{b}} \le 0.023\ \mu\mathrm{m}, \\ 68.12 \times d_{\mathrm{b}}^{1.32}, & d_{\mathrm{b}} > 0.023\ \mu\mathrm{m}, \end{cases} \tag{14}$$

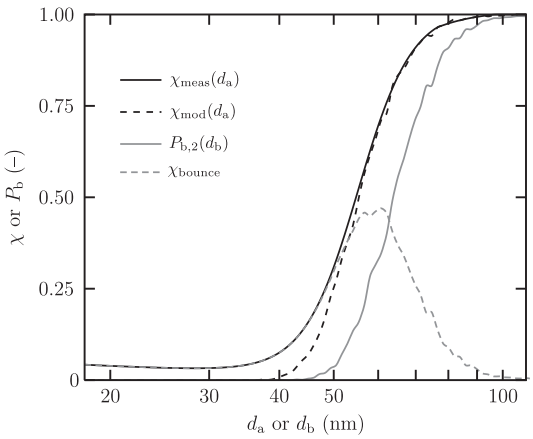

Fig. 3. Measured collection efficiency χ_{meas}, modeled collection efficiency χ_{mod} without diffusion losses and bounce probability $P_{\mathrm{b},2}$ as a function of particle size for the 2nd stage of an ELPI. In this figure, effective density is assumed to be one and thus $d_{\mathrm{a}} = d_{\mathrm{b}}$. In addition, collection efficiency χ_{bounce} when bouncing occurs and the illustrated bounce probability are shown.

where P is the particle penetration through the charger and n is the average number of charges per particle. Because the losses of the charger are mainly caused by the electric field in the charger, it is technically correct to include the penetration function to the initial charge distribution (i.e. $g_n = Pn$) when the charger is considered to be on but not when the charger is considered to be off. In the latter case, the charge distribution is initially zero.

At the stage n, the final current signal is caused by the particles $f_{\mathrm{f},n}$ and by the particles $f_{\mathrm{b},n}$ through charge transfer. The first part is calculated as

$$I'_n = eQ \int_0^\infty g_n(d_\mathrm{b}) f_{\mathrm{f},n}(d_\mathrm{b}) d \log d_\mathrm{b}, \tag{15}$$

where e is the elementary charge and Q is the flow rate through the impactor. The current induced by the bounced particles and charge transfer can be calculated by integrating Eq. (6) over the distribution $f_{\mathrm{b},n}$ and multiplying it with the term eQ. The result is

$$I''_n = eQ \int_0^\infty (q_\mathrm{c}(d_\mathrm{b}) f_{\mathrm{b},n}(d_\mathrm{b}) + \beta g_n(d_\mathrm{b}) f_{\mathrm{b},n}(d_\mathrm{b})) d \log d_\mathrm{b}. \tag{16}$$

Summing up the currents from Eqs. (15) and (16), the total current for the stage n and a part of the model output is obtained

$$I_n = I'_n + I''_n. \tag{17}$$

One of the main elements of the charge transfer process in a cascade impactor is that the charges of the particles may change after bouncing several times. In the model, this is taken into account by calculating the charge distribution over again after each impactor stage. The change is defined recursively as

$$g_{n-1} = g_n + \int_0^\infty \frac{f_{\mathrm{b},n}(d_\mathrm{b})}{f_{\mathrm{f},n}(d_\mathrm{b})} (q_\mathrm{c}(d_\mathrm{b}) + \beta g_n(d_\mathrm{b})) d \log d_\mathrm{b}. \tag{18}$$

So far, it is shown how the output current I_n is calculated at the stage n and how the particle size distribution f_{n-1} and the charge distribution g_{n-1} continuing to the next stage are determined. Next step is to repeat the procedures for the stage $n-1$.

Not only the model but also the manner it is connected to measurements is a crucial part of this work. If there are measured current distributions with and without the charger, the modeled currents can be fitted into the measured currents by searching optimum values for fitting parameters. The three fitting parameters are the effective density ρ_eff, the material coefficient of bouncing α and the contact charge $q_{\mathrm{c},0}$, the latter corresponding particle size $d_{\mathrm{p},0}$ and impaction velocity $v_{\mathrm{i},0}$. According to Eqs. (4) and (7), material coefficient and contact charge are dependent on particle density. Therefore, they are also theoretically dependent on effective density. However, in the fitting process, all these three parameters are equally free and the dependencies do not have any effect on the fitting. The other parameters of charge transfer are kept invariable: $d_{\mathrm{p},0} = 100$ nm, $v_{\mathrm{i},0} = 100$ m/s, $b_\mathrm{c} = 3$ and $\beta = 0$. Because the example materials used in this work are insulators, the value of b_c is chosen to be 3, which is supported by the theory and experiments of John et al. (1980). Assuming β to be zero is not as straightforward, but most of the values of β measured by John et al. (1980) and presented earlier in this work are smaller than 0.1. In addition, Fig. 4 shows an example of modeling the effect of β on bounce current, defined by Eq. (11), with a simulated lognormal size distribution. It reveals that growing β can be observed

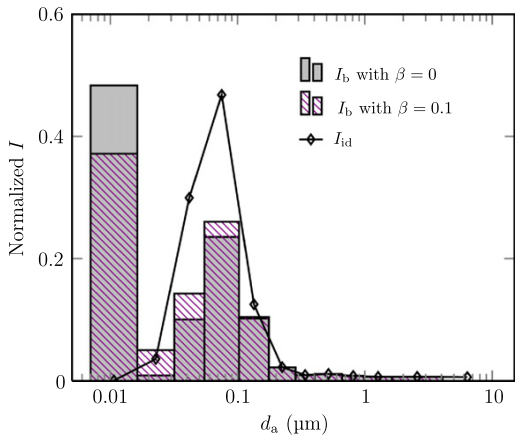

Fig. 4. Modeling the effect of β on bounce current I_b with a simulated lognormal size distribution. Also the ideal current I_id without bouncing and charge transfer is shown. Growing β fills the gap between the mode of impacted particles and the filter stage collecting the majority of bounced particles.

in the bounce current distribution. Due to the change in β, the relation of transferred charges in different stages changes, and the change fills the gap between the mode of impacted particles and the filter stage collecting the majority of the bounced particles. Thus, by observing measured bounce current, it is possible to see if β differs significantly from zero. Finally, the success of the fitting method in practice shows the validity of all the parameters.

In the fitting process, the difference between the measured and modeled current distributions is minimized by the method of least squares. Searching of the optimum parameter values is performed with an algorithm called Nelder–Mead simplex algorithm, which is a popular tool for multidimensional unconstrained minimization (Lagarias et al., 1999). The fitting process is divided into two separate parts. In the first part, the values of effective density and material coefficient are defined by fitting the bounce current I_b. The second part consists of fitting the current $I_{ch,off}$ and defining the value of contact charge.

5. Experiment

The experimental section of this work was carried out in a laboratory by measuring bounce and charge transfer behavior of nanoparticles. An ELPI, equipped with a filter stage (Marjamäki et al., 2002) and with an extra stage (Yli-Ojanperä et al., 2010) was used in these experiments. Normally, the substrates of the cascade impactor are coated with grease, which is an efficient means to prevent particle bounce in most cases. However, in this work, particle bounce was desirable. Thus, no grease was spread on the impactor plates and, along with standard steel substrates, also polished steel substrates were used. All the substrates were cleaned in an ultrasonic washing device and dried before assembling them to the impactor. The solution used in the washing device consisted of a 2% (v/v) solution of RBS 25 detergent dissolved in water. In few cases, isopropyl alcohol (IPA) was used instead of the detergent.

A schematic diagram of the experimental setup is seen in Fig. 5. The setup includes nanoparticle generation, an ELPI and a scanning mobility particle sizer (SMPS). The SMPS measures the mobility size distribution of generated particles and it consists of a DMA (TSI model 3081) and a CPC (TSI model 3025). The DMA was run with a sheath flow of 6 lpm and with a sample flow of 0.6 lpm. In the particle generation, an atomizer was used to produce approximately lognormal size distributions for the measurements. After the atomizer, the sample flow was dried either in a silica gel dryer or by diluting it with dry filtered air. Materials used in the watery solution of the atomizer were sodium chloride and levoglucosan. These two materials represent two different forms of solid phase as sodium chloride particles are crystalline and levoglucosan particles have been shown to be in an amorphous phase state (Mikhailov et al., 2009; Saukko et al., 2012). The concentration and the mean particle size of the aerosol led to the instruments could be varied by changing the liquid concentration in the atomizer, the flow rate through the atomizer and the optional dilution after the atomizer.

For each particle distribution, both the currents $I_{ch,on}$ and $I_{ch,off}$ were measured. Although the time resolution of the ELPI is only one second, the currents were averaged over 120 s to correspond the size distribution measured by the SMPS. Each particle size distribution was measured two times because the currents $I_{ch,on}$ and $I_{ch,off}$ could not be measured simultaneously. The currents for a representative analysis were finally measured for six sodium chloride distributions and four levoglucosan distributions. Using polished steel substrates in some cases, the effect of surface could be evaluated. Furthermore, the time dependency of the currents and the effect of substrate loading were observed by monitoring the ELPI currents.

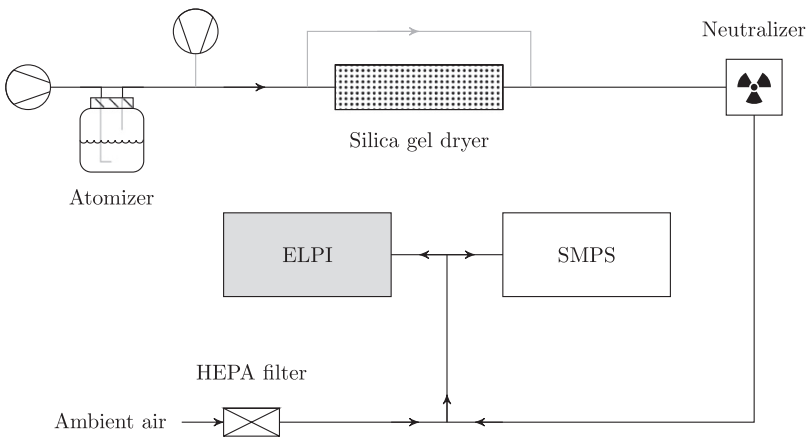

Fig. 5. A schematic diagram of the experimental setup. The dilution by pressurized air after the atomizer was optional as well as the by-passing of the silica gel dryer.

6. Results and discussion

The experimental data was analyzed by the fitting process based on the bounce and charge transfer model. An example of the fitting is seen in Fig. 6. The example shows three different current bar plots, including $I_{ch,on}$, $I_{ch,off}$ and normalized I_b, and a mobility size distribution measured with the SMPS. All these are linked to the same sodium chloride distribution. In the current plots, gray bars represent the measured currents and violet bars with a line pattern are the result of the model and the fitting process. Regarding the first two subfigures (Fig. 6(a) and (b)), it is clearly seen that the measured currents $I_{ch,on}$ and $I_{ch,off}$ have some irregularities which probably arise from the sensitivity of the charge transfer process. However, those changes seem to be similar in both the currents and they are no more seen in the bounce current (Fig. 6(a)). In fact, this remark is consistent with the theoretical assumption of the model, which states that $\beta \approx 0$ and the charge transfer do not have any effect on bounce current. In addition, there are practically no current in the gap between the mode of impacted particles and the filter stage (compare to the simulated bounce currents in Fig. 4), which supports the assumption of β being close to zero.

The agreement between the measured and modeled currents in Fig. 6(a)–(c) is good. Especially in Fig. 6(c), which shows the result of the first part of the fitting defining the values of ρ_{eff} and α, the agreement is even astonishingly good. Also the ideal current without bouncing and charge transfer is shown in Fig. 6(c). It is calculated from the mobility size distribution using the effective density value, the charging efficiency function, i.e. Eq. (14), and the collection efficiency curves of the ELPI impactor. Here, it could also be possible to use the bounce factor analysis, which can be performed only for the ELPI data. The advantage compared to the former bounce analyses by Virtanen et al. (2010, 2011) would be the concept of bounce current. In this case, where charge transfer is considerable, the usage of the general ELPI current $I_{ch,on}$ would lead to a negative value of bounce factor. In contrast, the bounce factor analysis together with the bounce current is a good estimation of bounce behavior. However, in this study, the more accurate analysis connected to the theoretical parameters of bouncing and charge transfer is preferred. Comparing the ideal current and the bounce current in Fig. 6(c), it can be seen that bouncing occurs almost in all the particle sizes and most of the bouncing particles finally end up to the filter stage. Practically, this allows one to see the original shape of the distribution in the bounce current and find a good estimate for the effective density in the fitting method.

In the main analysis of the experimental data, the fitting process was performed for six sodium chloride distributions and for four levoglucosan distributions. Parameter values from the fittings are seen in Table 1, which shows the average values of three parameters for each material and standard deviations as approximate error limits. Even though the amount of data is not very large and the deviations are notable especially for levoglucosan, the difference between two different materials can be seen in all parameter values. Nevertheless, the contact charge values may not be comparable with each other because of the uncertainties in the surface conditions of these measurements. This subject will be discussed more below. The most

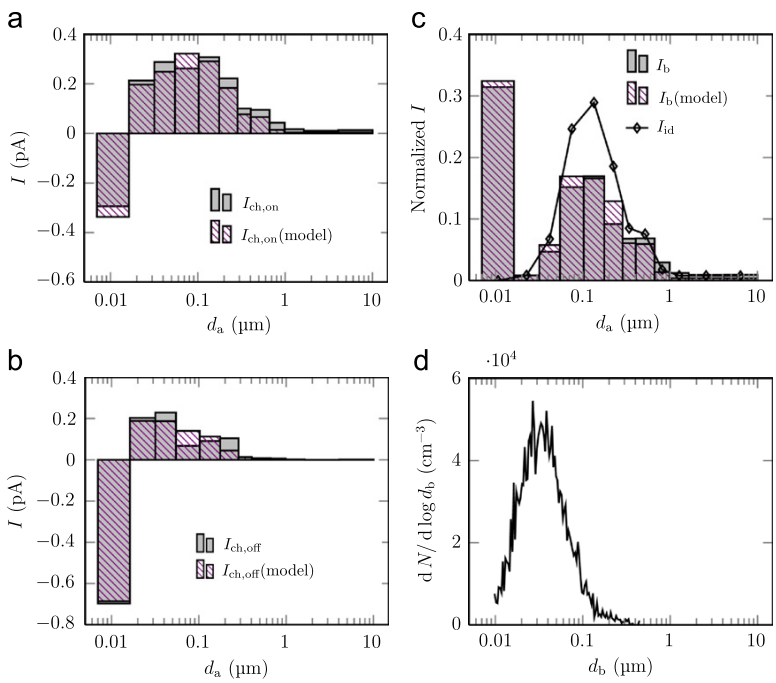

Fig. 6. An example of fitting the bounce and charge transfer model to a measured sodium chloride distribution. The currents measured by the ELPI (a) with the charger $I_{ch,on}$ and (b) without the charger $I_{ch,off}$ as well as (c) the normalized bounce current I_b are drawn in gray. Bars with a line pattern represent the modeled currents and the solid line the ideal current I_{id}, which are calculated from (d) the mobility size distribution measured by the SMPS.

Table 1
Parameter values from the fittings. The average values and standard deviations describing the error limits are calculated for six sodium chloride distributions and for four levoglucosan distribution. Bulk densities are shown as a reference to the effective density values.

Particle material	ρ_{bulk} (g/cm^3)	ρ_{eff} (g/cm^3)	α (m^2/s)	$q_{c,0}$
Sodium chloride	2.17[a]	2.23 ± 0.14	$(5.2 \pm 0.7) \times 10^{-6}$	0.49 ± 0.15
Levoglucosan	1.618[b]	1.5 ± 0.4	$(7.6 \pm 1.3) \times 10^{-6}$	0.22 ± 0.14

[a] CRC Handbook (2007).
[b] Rosenørn et al. (2006).

promising results are the effective density values which are comparable to the bulk density values also shown in Table 1. Of course, there are more useful methods for defining the effective density such as the general use of an ELPI and the method introduced by Ristimäki et al. (2002), but these good results strongly support the fitting method and the significance of the other parameter values α and $q_{c,0}$. Surface conditions and particle size may affect these parameters, as discussed more below, but in a single measurement these parameters characterize well the bounce and charge properties of particles.

Looking in detail Table 1, the values of α indicate that sodium chloride particles are more inclined to bounce than levoglucosan particles. The values are of the same magnitude as the previously presented material coefficient values measured in the micrometer size range (Cheng & Yeh, 1979; John, 1995). As presented earlier in Eq. (4), α is dependent on particle density. Taking account this dependency, it is seen that the density partly accounts for the difference between sodium chloride and levoglucosan. According to the values of $q_{c,0}$, sodium chloride would also be more inclined to transfer charge with a steel surface than levoglucosan. However, in this respect, it is reasonable to discuss only about the magnitudes of the results. The contact charge of sodium chloride can be compared to the results of John et al. (1980) by extrapolating the size dependency and impact velocity equations presented earlier. In 100 nm and 100 m/s, the extrapolated value is 0.88. This is of the same magnitude as the result of the fitting method 0.49.

To analyse the possible size dependency of the results given by the fitting method, the parameter values are drawn in Fig. 7 as a function of particle mode GMD. Because of relatively high deviations and small amount of data, it is difficult to analyze the possible size dependency of levoglucosan particles. However, if only the violet circles, representing sodium chloride particles measured with conventional steel substrates, are considered, rather clear size dependency is seen for the parameter α but not for ρ_{eff} and q_c. It means that, for effective density and contact charge, the fitting method works and most of the theoretical assumptions behind the model are relevant at least in this size range. On the other hand, the size dependency of material coefficient probably refers to a disagreement with the theoretical size dependency of the capture limit shown in Eq. (3). The real size dependency of nanoparticles should be studied experimentally in detail in the future to be able to modify the theory and the model. However, the results of the fitting method are still relevant and comparable also for material coefficient, if particle modes are in the same size range.

The parameter values were also viewed as a function of particle concentration but no clear correlation was observed. However, the effect of the substrate roughness, loading and cleaning process are discussed in more detail. In Fig. 7, the triangle markers represent parameter values that are calculated for the measurements with polished steel substrates. Intuitively, a polished steel surface could be seen more efficient and more stable a tool for bouncing and charge transfer measurements compared to a rougher steel surface. In practice, Fig. 7 shows that there is no significant difference in the parameter values between conventional and polished steel substrates except the case of the contact charge of sodium chloride. In that case, higher contact charge values are related to the substrate loading and the time dependency of charge transfer. This will be discussed more below but, altogether, the results measured with both substrates are mostly comparable and there are no advantages in using polished substrates.

Substrate loading and changes in the surface can affect considerably the charge transfer. John et al. (1980) noticed that it took from 20 to 60 min for contact charge to achieve an asymptotic value after starting the measurement with a cleaned substrate. In the experiments of this work, surface exposure times and measured particle concentrations varied. Actually, clearly asymptotic behavior was not observed but changes as a function of time were always seen to some extent in the measured currents. However, the only situation, where it notably affected the final parameter values given by the fitting method, is the case of polished steel substrates and sodium chloride. In Fig. 7(c), the two triangle markers above the others represent this case. These points were measured with fresh cleaned substrates. For some reason, the charge transfer was very intensive at the beginning but it also decreased rather quickly reaching the normal level compared to the other measurements in about 20 min. This example could be regarded as an unsuccessful measurement of contact charge, but interesting is, that it is not unsuccessful in the sense of measuring effective density or material coefficient. As seen in Fig. 7, those parameter values compare well to the other measurements.

Fig. 7 also shows two measurements for levoglucosan, in which the substrates were cleaned with isopropyl alcohol (IPA) instead of RBS. Once again, the difference between these two cleaning procedures is most clearly seen in the contact charge values. According to these measurements, cleaning the steel substrates with RBS seems to result in higher contact charge values and more intense charge transfer than cleaning the substrates with isopropyl alcohol. Other parameter values are not as sensitive to different cleaning procedures. Altogether, obtaining a meaningful contact charge parameter

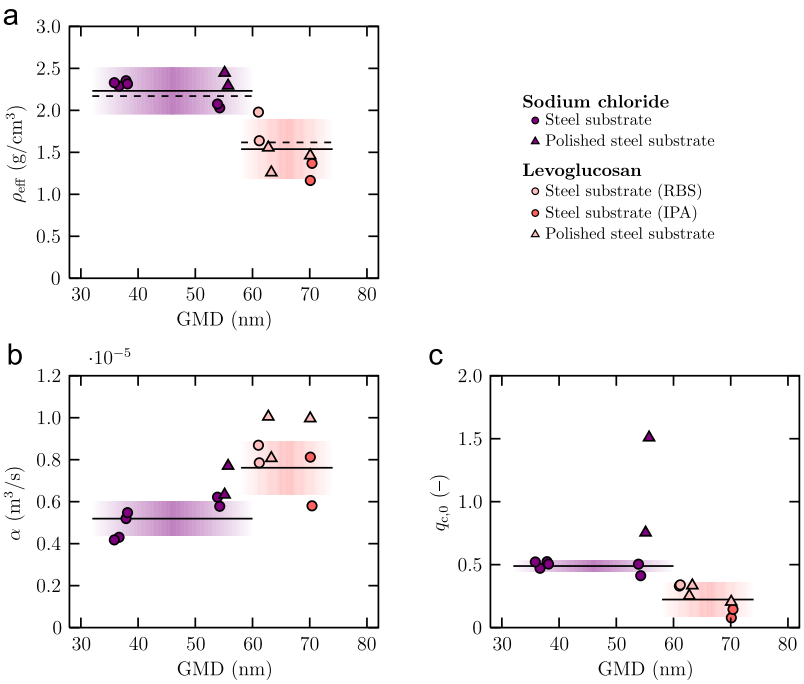

Fig. 7. The parameter values (ρ_{eff}, α and $q_{\mathrm{c,0}}$) as a function of particle mode GMD. Representative values are marked with circles and the average values for each material with a solid line. Dashed lines represent the bulk densities and colored bars the standard deviations. For the contact charge parameter, the effect of different cleaning methods (RBS and IPA) and polished substrates can be seen. (For interpretation of the references to color in this figure caption, the reader is referred to the web version of this article.)

experimentally seems to be problematic because of the effect of substrate roughness, substrate loading and cleaning procedures. In a single measurement, the contact charge value provided by the fitting method describes well the charge transfer behavior, but, in order to compare the results of several measurements, the effect of different substrates and surface conditions should be studied in more detail. Even though the contact charge values of sodium chloride in Table 1 were close to the values measured by John et al. (1980) for micrometer-sized sodium chloride particles and a steel substrate, it cannot be said that these values reliably represent the contact charge between a sodium chloride nanoparticle and a steel substrate. To reach the fundamental contact charge values between nanoparticles and different surface materials, extensive measurements for different cleaning procedures and substrate materials are required in the future, for example, using the method introduced in this study.

7. Conclusions

Bouncing of nanoparticles has recently become an important tool in studying the phase state of atmospheric aerosols. Bouncing and its common side effect charge transfer can be considered as fundamental phenomena in aerosol physics. However, these phenomena are not fully understood and there are practically no previous experimental studies or systematic methods presented for bouncing and charge transfer of nanometer-sized particles. This work shows that both bouncing and charge transfer of nanoparticles can be characterized with a new method. The method is based on an ELPI measurement with and without the charger, which enables the separation of the two phenomena. Further analysis relies on a new bouncing and charge transfer model constructed for the ELPI and on a simultaneous measurement with an ELPI and an SMPS. By fitting the modeled ELPI currents to the measured currents, bouncing and charge transfer of nanoparticles can be described by the existing theory of micrometer-sized particles.

The method presented here is a unique tool for defining the theoretical parameters of bouncing and charge transfer from an experimental analysis of nanoparticles. To authors' knowledge, there are no other methods that are capable of this. Although the method is a pioneering one, it is still exceptionally ready for use in different environments and applications. From the point of view of experiments, the straightforward utilization of commercially available measuring devices is a great advantage and no special modifications are required. The method is designed for a polydisperse aerosol distribution which is advantageous in many cases as well. In the fitting process, especially the effective density as a fitting parameter, along with the parameters of bouncing and charge transfer, provides a possibility to evaluate the results given by the fitting method and, in some cases, compare the results with reference data.

This work has been able to emerge the theories of bouncing and charge transfer to the experiments for nanometer-sized particles. There are still some experimental challenges, such as the effect of substrate roughness, substrate loading and cleaning procedures on charge transfer, and theoretical problems, such as the size dependency of bouncing. However, it is important that the tool now exists. In the future, more experiments should be performed for different particle and substrate materials, and the method could be developed further for different applications. To understand the fundamental phenomena of bouncing and charge transfer, totally new approaches may be required, but after this study, the task seems to be more conceivable.

Acknowledgments

This work was supported by a grant from the Nessling Foundation. H. Kuuluvainen acknowledges the support from the Graduate School of Tampere University of Technology.

References

Arffman, A., Marjamäki, M., & Keskinen, J. (2011). Simulation of low pressure impactor collection efficiency curves. *Journal of Aerosol Science*, *42*(5), 329–340.
Bailey, A.G. (1984). Electrostatic phenomena during powder handling. *Powder Technology*, *37*(1), 71–85.
Bergström, L. (1997). Hamaker constants of inorganic materials. *Advances in Colloid and Interface Science*, *70*(1–3), 125–169.
Chang, M., Seongheon, K., & Sioutas, C. (1999). Experimental studies on particle impaction and bounce: Effects of substrate design and material. *Atmospheric Environment*, *33*(15), 2313–2322.
Cheng, Y.S., & Yeh, H.C. (1979). Particle bounce in cascade impactors. *Environmental Science and Technology*, *13*(11), 1392–1396.
CRC Handbook. (2007). *CRC Handbook of Chemistry and Physics* (88th ed.). CRC Press.
Dahneke, B. (1971). The capture of aerosol particles by surfaces. *Journal of Colloid and Interface Science*, *37*(2), 342–353.
Froeschke, S., Kohler, S., Weber, A.P., & Kasper, G. (2003). Impact fragmentation of nanoparticle agglomerates. *Journal of Aerosol Science*, *34*(3), 275–287.
Fujitani, Y., Hasegawa, S., Fushimi, A., Kondo, Y., Tanabe, K., Kobayashi, S., & Kobayashi, T. (2006). Collection characteristics of low-pressure impactors with various impaction substrate materials. *Atmospheric Environment*, *40*(18), 3221–3229.
Hinds, W.C. (1999). *Aerosol Technology: Properties, Behavior, and Measurement of Airborne Particles* (2nd ed.). John Wiley & Sons.
John, W. (1995). Particle–surface interactions: Charge transfer, energy loss, resuspension, and deagglomeration. *Aerosol Science and Technology*, *23*(1), 2–24.
John, W., Reischl, G., & Devor, W. (1980). Charge transfer to metal surfaces from bouncing aerosol particles. *Journal of Aerosol Science*, *11*(2), 115–138.
Kannosto, J., Yli-Pirilä, P., Hao, L., Leskinen, J., Jokiniemi, J., Mäkelä, J. M., Joutsensaari, J., Laaksonen, A., Worsnop, D. R., Keskinen, J., & Virtanen, A. Bounce characteristics of α-pinene derived SOA particles with implications to physical phase. *Boreal Environment Research*, accepted.
Keskinen, J., Pietarinen, K., & Lehtimäki, M. (1992). Electrical low pressure impactor. *Journal of Aerosol Science*, *23*(4), 353–360.
Kittelson, D.B., Watts, W.F., & Johnson, J.P. (2004). Nanoparticle emissions on Minnesota highways. *Atmospheric Environment*, *38*(1), 9–19.
Kruis, F.E., Fissan, H., & Peled, A. (1998). Synthesis of nanoparticles in the gas phase for electronic, optical and magnetic applications—A review. *Journal of Aerosol Science*, *29*(5–6), 511–535.
Kulmala, M., Vehkamäki, H., Petäjä, T., Maso, M.D., Lauri, A., Kerminen, V.M., Birmili, W., & McMurry, P.H. (2004). Formation and growth rates of ultrafine atmospheric particles: A review of observations. *Journal of Aerosol Science*, *35*(2), 143–176.
Lagarias, J.C., Reeds, J.A., Wright, M.H., & Wright, P.E. (1999). Convergence properties of the Nelder–Mead simplex method in low dimensions. *SIAM Journal on Optimization*, *9*(1), 112–147.
Marjamäki, M., Ntziachristos, L., Virtanen, A., Ristimäki, J., Keskinen, J., Moisio, M., Palonen, M., & Lappi, M. (2002). Electrical filter stage for the ELPI. In: *Society of Automotive Engineers (SAE)*. Technical Paper Series 2002-01-0055.
Matsusaka, S., Maruyama, H., Matsuyama, T., & Ghadiri, M. (2010). Triboelectric charging of powders: A review. *Chemical Engineering Science*, *65*(22), 5781–5807.
Mikhailov, E., Vlasenko, S., Martin, S.T., Koop, T., & Pöschl, U. (2009). Amorphous and crystalline aerosol particles interacting with water vapor: Conceptual framework and experimental evidence for restructuring, phase transitions and kinetic limitations. *Atmospheric Chemistry and Physics*, *9*(24), 9491–9522.
Mullins, B.J., Agranovski, I.E., & Braddock, R.D. (2003). Particle bounce during filtration of particles on wet and dry filters. *Aerosol Science and Technology*, *37*(7), 587–600.
Reuter-Hack, K., Weber, A.P., Rösler, S., & Kasper, G. (2007). First LDA measurements of nanoparticle velocities in a low-pressure impacting jet. *Aerosol Science and Technology*, *41*(3), 277–283.
Ristimäki, J., Virtanen, A., Marjamäki, M., Rostedt, A., & Keskinen, J. (2002). On-line measurement of size distribution and effective density of submicron aerosol particles. *Journal of Aerosol Science*, *33*(11), 1541–1557.
Rogers, L.N., & Reed, J. (1984). The adhesion of particles undergoing an elastic–plastic impact with a surface. *Journal of Physics D: Applied Physics*, *17*(4), 677–689.
Rosenørn, T., Kiss, G., & Bilde, M. (2006). Cloud droplet activation of saccharides and levoglucosan particles. *Atmospheric Environment*, *40*(10), 1794–1802.
Saukko, E., Kuuluvainen, H., & Virtanen, A. (2012). A method to resolve the phase state of aerosol particles. *Atmospheric Measurement Techniques*, *5*(1), 259–265.
Seipenbusch, M., Toneva, P., Peukert, W., & Weber, A.P. (2007). Impact fragmentation of metal nanoparticle agglomerates. *Particle and Particle Systems Characterization*, *24*(3), 193–200.
Virtanen, A., Joutsensaari, J., Koop, T., Kannosto, J., Yli-Pirilä, P., Leskinen, J., Mäkelä, J.M., Holopainen, J.K., Pöschl, U., Kulmala, M., Worsnop, D.R., & Laaksonen, A. (2010). An amorphous solid state of biogenic secondary organic aerosol particles. *Nature*, *467*(7317), 824–827.
Virtanen, A., Kannosto, J., Kuuluvainen, H., Arffman, A., Joutsensaari, J., Saukko, E., Hao, L., Yli-Pirilä, P., Tiitta, P., Holopainen, J.K., Keskinen, J., Worsnop, D.R., Smith, A., & Laaksonen, A. (2011). Bounce behavior of freshly nucleated biogenic secondary organic aerosol particles. *Atmospheric Chemistry and Physics*, *11*(16), 8759–8766.
Wall, S., John, W., & Wang, H.-C. (1990). Measurements of kinetic energy loss for particles impacting surfaces. *Aerosol Science and Technology*, *12*(4), 926–946.
Watanabe, H., Ghadiri, M., Matsuyama, T., Ding, Y.L., Pitt, K.G., Maruyama, H., Matsusaka, S., & Masuda, H. (2007). Triboelectrification of pharmaceutical powders by particle impact. *International Journal of Pharmaceutics*, *334*(1–2), 149–155.
Weber, A.P., & Wu, T. (2009). Kontaktauflaung von Nanopartikeln bei Impaktion. *Chemie-Ingenieur-Technik*, *81*(6), 791–795.
Yli-Ojanperä, J., Kannosto, J., Marjamäki, M., & Keskinen, J. (2010). Improving the nanoparticle resolution of the ELPI. *Aerosol and Air Quality Research*, *10*(4), 360–366.

Publication III

E. Saukko, H. Kuuluvainen, and A. Virtanen. A method to resolve the phase state of aerosol particles. *Atmospheric Measurement Techniques*, 5(1):259–265, 2012.

Atmos. Meas. Tech., 5, 259–265, 2012
www.atmos-meas-tech.net/5/259/2012/
doi:10.5194/amt-5-259-2012

Atmospheric Measurement Techniques

A method to resolve the phase state of aerosol particles

E. Saukko[1], **H. Kuuluvainen**[1], **and A. Virtanen**[1,*]

[1]Department of Physics, Tampere University of Technology, Tampere, Finland
[*]now at: Department of Applied Physics, University of Eastern Finland, Kuopio, Finland

Correspondence to: E. Saukko (erkka.saukko@tut.fi)

Received: 23 June 2011 – Published in Atmos. Meas. Tech. Discuss.: 6 October 2011
Revised: 20 December 2011 – Accepted: 18 January 2012 – Published: 30 January 2012

Abstract. The phase state of atmospheric aerosols has an impact on their chemical aging and their deliquescence and thus their ability to act as cloud condensation nuclei (CCN). The phase change of particles can be induced by the deliquescence or efflorescence of water or by chemical aging. Existing methods, such as tandem differential mobility analysis rely on the size change of particles related to the water uptake or release.

To address the need to study the phase change induced by mass-preserving and nearly mass-preserving processes a new method has been developed. The method relies on the physical impaction of particles on a smooth substrate and subsequent counting of bounced particles by a condensation particle counter (CPC). The connection between the bounce probability and physical properties of particles is so far qualitative.

To evaluate the performance of this method, the phase state of ammonium sulfate and levoglucosan, crystalline and amorphous solid, in the presence of water vapor was studied. The results show a marked difference in particle bouncing properties between substances – not only at the critical relative humidity level, but also on the slope of the bouncing probability with respect to humidity. This suggests that the method can be used to differentiate between amorphous and crystalline substances as well as to differentiate between liquid and solid phases.

1 Introduction

Particle deliquescence plays an important role in cloud condensation dynamics and is thus studied widely. Common methods to investigate particle-water interaction are the use of hygroscopicity tandem DMA, (HTDMA) (Rader and McMurry, 1986; Liu et al., 1978) and cloud condensation nucleus counter (CCN-counter) (Hudson, 1993; Roberts and Nenes, 2005). These methods rely on detecting the size change of particles as they are deliquesced in HDTMA according to the Köhler theory, or activated to larger droplets in CCN-counter. The notable size change steps in the HTDMA spectrum is used to determine the efflorescence and deliquescence relative humidity (ERH and DRH) (Seinfeld et al., 1998). These methods, nevertheless, can not distinguish the phase state of the particles.

The electrodynamic balance technique is also used to study particle-water interaction (Marcolli and Krieger, 2006; Pope et al., 2010) and this gives ample information about the particle size and water uptake kinetics, and also of its phase. The method is, however, constrained to large particles, typically 2–50 µm.

In case of water uptake induced phase change, the connection between the phase change from solid to liquid upon major change in particle size is evident, but for example the possible oxidation induced phase change – when the size stays constant – can not be detected by these methods apart from possible changes in the kinetics of the particle growth.

The phase state is an important factor for the lifetime consideration of the particles since the chemical reactions in the particle become diffusion limited surface reactions in solid particles. This may increase the lifetime of organic aerosols markedly, as the oxidation caused by atmospheric ozone, nitrous oxides and hydroxyl radicals is confined only to the surface. The water activation of particles can also be strongly affected by its phase (Hori et al., 2003; Bilde and Svenningsson, 2004). Solid crystalline particles activate faster than amorphous solid particles as the diffusion of water to the bulk is much slower for the latter (Zahardis and Petrucci, 2007; Zobrist et al., 2008)

According to the recently published research, the physical phase of the particles can be studied by investigating particle bounce properties (Virtanen et al., 2010). When an aerosol particle collides with an impaction surface, one part of its kinetic energy is dissipated in the deformation process, and another part is converted elastically into the kinetic energy of rebound (Dahneke, 1971). If the rebound energy exceeds the adhesion energy, the particle will bounce from the surface. Thus both the elastic properties and surface properties of particles affect their bounce probability (Rogers and Reed, 1984).

In the method utilized by Virtanen et al. (2010) the bounce is determined by using electrical low pressure impactor (ELPI). In a cascade impactor, the aerosol particle bounce perturbs the measurement as larger particles are transferred to lower stages upon bounce, thus tilting the inferred size distribution to smaller particles. This phenomenon is usually considered unwanted and is suppressed by different substrates and coatings. When particle bounce occurs in an ELPI, a significant excess current is measured in the lowest impactor stages and the back-up filter resulting from the charges carried by the bounced particles. Virtanen et al. (2010) defined the *Bounce factor* by calculating the fraction of excess current measured in the lowest impactor stages. The method is a fast way to detect the bounce, but the Bounce factor, defined from ELPI measurement, depends not only on the bounce properties of the particles, but also on the charge transfer properties of the particles and the substrate. Thus quantitative information on bounce characteristics of particles is not currently possible to get by utilizing the electrical detection method

Here we present a bounce measurement method based on single stage impactor with optical, instead of electrical, detection. The fraction of bounced particles is defined by a direct measurement of particle concentration in the inlet and outlet of the impactor. We test the method with crystalline and amorphous laboratory aerosols and present the bounce results related to the humidity induced phase transitions of crystalline and amorphous solid materials.

2 Experimental methods and materials

The measurement setup is described schematically in Fig. 1. The aerosol was generated from de-ionized water (DI-water, Milli-Q) solutions of 1 to 2 g l^{-1} using a Collison atomizer. After generation, 1.5 lpm of the aerosol was conducted through Topas silica gel diffusion dryer, or in the case of ammonium sulfate, diluted, to reach the efflorescence relative humidity of the nebulized material and the rest vented. The aerosol was then charged and classified with a Vienna type DMA. The classified aerosol was diluted and conducted through a Permapure nafion tube which humidified the aerosol to a controlled RH.

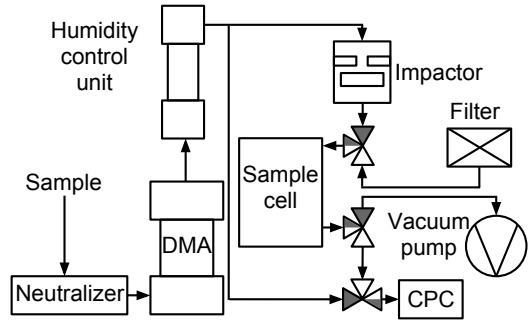

Fig. 1. Measurement setup used in the DRH experiments. The dark route through valves denote the sampling period and white route the measurement period.

After the humidifier there was a residence time of 3 s after which the flow was separated to the impactor and to the ultrafine water condensation particle counter (UWCPC, TSI 3786) to measure the number concentration entering into the impactor. The flow to the impactor was constricted using a pinhole orifice and a needle valve to achieve desired upper pressure for the impactor. The flow leaving the impactor is guided to a vacuum pump through a sampling cell of a volume of 0.4 l and a needle valve. This is referred to as the sampling mode, and denoted in dark in the valves in Fig. 1.

The sampling is continued until the impactor pressures have stabilized and the sampling cell has been flushed several times. Next the valves are turned such that the cell is repressurized with particle free air and the CPC is measuring the decreasing concentration of particles in the cell. This is the measurement mode, and is denoted in white in the valves in Fig. 1. The measurement is continued until sufficient number of particles are measured, after which the system is returned to the sampling mode.

The bounced fraction can be computed from the UWCPC data record by comparing the concentration from upstream of the impactor and the sample from the repressurised sample cell. To take in to account the decrease in concentration caused by dilution and the different losses at separate routes and residence times for the reference sample and the bounced sample, a baseline sample calibration was done with the collection plate removed. The bounced fraction of the particles can be thus calculated as the relation of the passed particles to the entering particles, divided by the same relation for the baseline sample.

The collection plate for the impactor was polished steel plate, thoroughly cleaned and finally rinsed with de-ionized water. The operational conditions for the ELPI-type impactor used in the study are presented in Table 1.

Table 1. The operational parameters for the impactor, p_u and p_l are the pressures above and below the jet stage, respectively and d_{50} is the 50 % collection efficiency cutpoint of the impactor as calibrated.

NTP Air flow	d_{50}	Jet diameter	Jet number	p_u	p_l
2.3 lpm	120 nm	0.3 mm	5	68.56 kPa	38.72 kPa

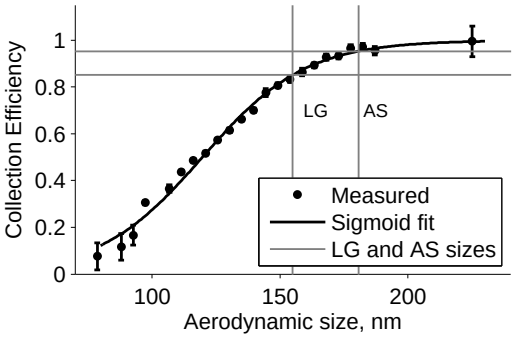

Fig. 2. The collection efficiency curve and sigmoid fit for the impactor stage used. Marked are the aerodynamic sizes and corresponding collection efficiencies for levoglucosan (LG) and ammonium sulfate (AS).

The chosen mobility sizes of the levoglucosan and ammonium sulphate particles were 105 and 115 nm, respectively. When taking into account the densities of the substances (1.618 g cm^{-3} Rosenørn et al., 2006 and 1.77 g cm^{-3} Lide, 2008, respectively) and assuming spherical particles, the aerodynamic size for levoglucosan particles is 155 nm and for ammonium sulfate particles 181 nm.

The impactor collection efficiency curve was measured using dioctyl sebacate (DOS), in a similar setup described for electrical low pressure cascade impactor in Keskinen et al. (1999). The collection efficiency curve for the impactor used is shown in Fig. 2.

When efflorescence relative humidity measurements were done, an extra nafion tube humidifier was set to 80 % and after a minimum of 3 s residence time, the second nafion tube was used to dry the sample and further 3 s residence time was allowed before measurement step.

2.1 Data analysis

When operating with particle sizes where the calibrated collection efficiency shown in Fig. 2 is below unity, a further correction is needed to get the bounced fraction of the particles separated from the particles which do not impact to the substrate. This corrected bounced fraction is calculated as:

$$B = \frac{B' - (1 - C_E(d_a))}{C_E(d_a)} \quad (1)$$

where $B\prime$ is the measured, uncorrected bounced fraction and $C_E(d_a)$ is the calibrated collection efficiency at the aerodynamic particle size d_a that was used. The use of correction allows for the use of smaller particle sizes where the collection efficiency has not reached unity. The downside is the reduced dynamics; using correction means scaling up the real data, but at the same time scaling up the noise. Thus it is not advisable to operate the impactor at the lower portion of the collection efficiency curve. The use of the steepest portion of the curve may also induce larger errors due to the errors in the calculated aerodynamic diameter discussed below; error in the diameter, shape or density causes large error in collection efficiency if the slope is very steep. It should be also noted, that the particle aerodynamic size needs to be known to make the correction.

The aerodynamic particle size can be calculated with (Kelly and McMurry, 1992):

$$d_a = d_p \left(\frac{C_C(d_p)}{C_C(d_a)} \right)^{1/2} \left(\frac{\rho_e}{\rho_0} \right)^{1/2}, \quad (2)$$

where d_p is the mobility diameter, C_C is the Cunningham slip correction factor, and ρ_e and ρ_0 are the effective densities of the particle matter and water, respectively. The aerodynamic particle sizes for dry particles are 155 nm and 181 nm for levoglucosan and ammonium sulfate.

The growth factors for the aerosols were not measured, but based on Mikhailov et al. (2009), the growth factor at the maximum attainable humidity conditions system, 60 % RH (see Figs. 5 and 4) for levoglucosan is 1.2 and about 1.3 for deliquesced ammonium sulfate. While this is a notable increase in the mobility diameter, the aerodynamic diameter, for which the collection efficiency is calibrated, does not change very much. When the particles are hydrated, the new diameter is $d_p \cdot$ GF and the effective density, assuming a volume additivity of the mixture:

$$\rho_p = \frac{\rho_p + \rho_0 (\mathrm{GF}^3 - 1)}{\mathrm{GF}^3} \quad (3)$$

When the deliquesced density and mobility diameter is substituted to Eq. (2), the deliquesced aerodynamic diameters

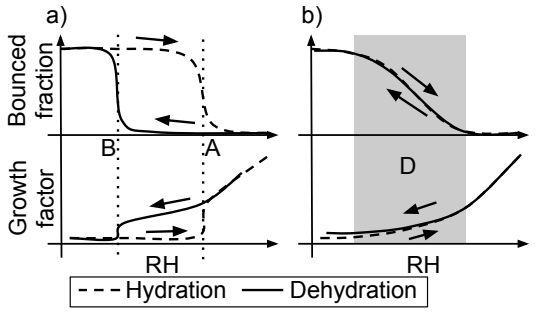

Fig. 3. A schematic figure of the relation of the fraction of the bounced particles and growth factor during hydration and dehydration of, **(a)** a crystalline solid sample and **(b)** an amorphous solid sample. Growth factor curve schematics adapted from Mikhailov et al. (2009).

are 162 nm and 188 nm, respectively. This results in a maximum error of 3.2 % of the collection efficiency. Further error analysis gives the maximum error on corrected bounce to be:

$$\Delta B = \frac{1-B'}{C_E}\Delta C_E \tag{4}$$

At the maximum condition i.e. lowest used collection efficiency and lowest bounce fraction (zero), the error is 3.8 %, which is within experimental noise.

2.2 Hydration and dehydration induced phase transitions

The humidity induced phase transitions of crystalline and amorphous solids are explained thoroughly by Mikhailov et al. (2009) and experimental data for ammonium sulfate and levoglucosan are presented. Briefly, crystalline substances exhibit hysteresis upon the phase change very clearly in step-function like manner and amorphous solids have a wide, continuous regime of hydration induced water uptake. Figure 3 shows schematic representations of the effect of phase change to growth factor and to bounce probability. When relating the measured bounce data with the sample humidity, the pressure reduction in the impactor must be taken into account. As the pressure decreases, the concentration of water molecules reduces in the ratio of the pressure drop. We denote this RH inside the impactor *Impactor RH*, RH_I.

$$\mathrm{RH_I} = \mathrm{RH_H}\frac{p_\mathrm{u}}{p_\mathrm{amb}} \tag{5}$$

where $\mathrm{RH_H}$ is the relative humidity in the humidifier and p_u and p_amb are the impactor upper pressure and the ambient pressure, respectively. The impactor upper pressure for the present study is 68.56 kPa. This limits the operational RH range in the impactor to less than 65 % $\mathrm{RH_I}$.

The particles have sufficient time (0.9 s) to equilibrate to the Impactor RH. This means that in practice, we are drying the particles in the impactor. In the results section figures, also the relative humidity before the impactor, *Humidifier RH*, is shown on a separate axis.

The particle experiences a short time in the lower-pressure acceleration region before there is a section of stagnation pressure before the impaction. The timescale of the acceleration and the impaction are in the order of microseconds. Based on this we assume that the conditions above the stage define the state of the particles at the moment of impaction. This assumption is verified by the results from ammonium sulfate aerosol and is further discussed in the results section.

When the sample RH in the inlet of the impactor is higher than the deliquescence RH of the substance (point A in Fig. 3a) particle remain liquid in the impactor conditions if the Impactor RH is higher than the ERH of the material (point B in the Fig. 3a). In that case, the DRH point can be determined by bounce measurement. If the Impactor RH is lower than the ERH, particles are solid at the moment of the impaction and no clear changes in the bounce of the particles can be seen even if the sample RH is increased to values corresponding DRH. To avoid the latter case, the operation point should be chosen for high enough pressure.

When the efflorescence behavior of the particle is investigated, the sample is first humidified (RH values larger than DRH). After the humidification, the sample is dried by drier and then lead to the impactor. The sample is further dried due to the pressure drop in the impactor. The sample humidity is altered by altering the dryer conditions until the Impactor RH achieves ERH values and bounce increases again (point B in Fig. 3a).

For the amorphous particles the deliquescence is continuous in a wide range and there is no sharp hysteresis and thus no sharp phase transition on either the growth factor (Mikhailov et al., 2009) or the bounce probability. This is represented by area D in Fig. 3b.

3 Results

The method is demonstrated with ammonium sulfate as the crystalline test substance and levoglucosan as the amorphous test substance. Both of these substances are easy to obtain and their phase state when in aerosol form, with respect to relative humidity, is well documented (Mikhailov et al., 2009)

3.1 Crystalline solid

The change of phase can be clearly seen in the bounce diagram of 115 nm (mobility size), ammonium sulfate (Fig. 4), where the fraction of the bounced particles reduce almost with a step-like manner at the deliquescence relative humidity of around 81 % (Humidifier RH) when going up in the

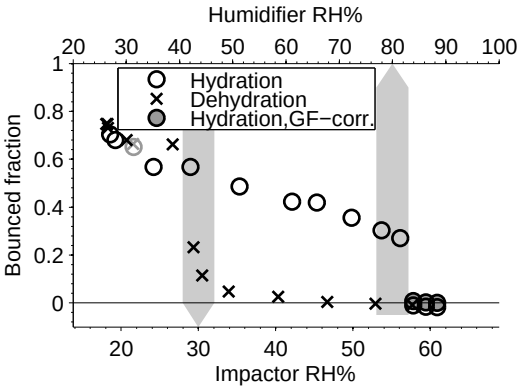

Fig. 4. Bounce fractions of ammonium sulfate aerosol at hydration and dehydration experiments. The *GF-corrected* points denote hydration points corrected for water uptake induced change in aerodynamic particle size as discussed previously. The first humidifier was kept at 90 % RH for the ERH run. The arrows point at the efflorescence and deliquescence relative humidities reported in Mikhailov et al. (2009). Bounced fraction is corrected according to Eq. 1. The gray symbols denote *downscan points*, to show the effect of loading of the substrate.

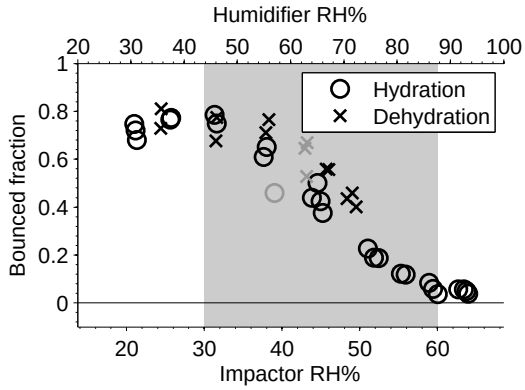

Fig. 5. Bounce fractions of levoglucosan aerosol at hydration and dehydration experiments. The first humidifier was kept above 75 % RH for the ERH run. The gray patch indicates the transitional area from solid to liquid, reported by Mikhailov et al. (2009). Bounced fraction is corrected according to Eq. (1). The gray open symbols denote *downscan points*, to show the effect of loading of the substrate.

humidity. Although the actual humidity the particle is exposed is lower than DRH, the hysteresis of the deliquescence ensures wetted phase state, once the particles have reached the DRH. The DRH for ammonium sulfate particles defined by Mikhailov et al. (2009) is marked by the gray arrow in Fig. 4.

As can be seen in Fig. 4 the bounce of AS particles decreases from value of approximately 0.75 to 0.3 already at the sample RH values lower than DRH. We relate this behavior to adsorption of water molecules on ammonium sulfate particles (Romakkaniemi et al., 2001; Biskos et al., 2006; Mikhailov et al., 2009) as well as possibly on the surface of the collection substrate.

When measuring the efflorescence point, deliquesced particles are dried from their DRH, until at around 30 % Impactor RH the particles start to bounce again. This ERH value measured by the bounce method is comparable to ERH values measured for ammonium sulfate particles by the HTDMA method (Mikhailov et al., 2009; Onasch et al., 1999; Brooks et al., 2002). The results are well in line with the assumption that the humidity inside the impactor is reduced by the ratio of the pressure above the impactor stage to the ambient pressure and that the particles do equilibrate to the humidity conditions in the impactor.

The particle bounce does not go up all the way to unity, but at about 20 % Impactor RH, stays at 0.8. This indicates either that when the impactor plate is in place, the changes in flow pattern induce more losses to the walls and the roof of the impactor stage, compared to the baseline setup, or that some of the particles still stick to the impactor plate on impact. With the Humidifier RH above deliquescence, the bounced fraction, when corrected for collection efficiency, is at, or slightly below zero. When the estimated effect of water absorption on aerodynamic size is included, as discussed in Sect. 2.1, the corrected bounce fraction rises slightly to, or above the zero level (filled circles in Fig. 4).

The effect of loading of the impactor substrate during the experiments was studied by measuring additional points at low humidity values ∼30 % RH, after measuring the complete range from low humidity to high humidity. These *downscan points* are marked with gray edges in Fig. 4. There is no difference in bounce to the level measured in the upstepping part of the data. The magnitude of the loading effect is expected to be loading-dependent; at this experiment at number concentration of 1.7 to 2.6×10^3 cm^{-3} it is negligible.

3.2 Amorphous solid

The bounce diagram for 105 nm levoglucosan particles is shown in Fig. 5. There is no hysteresis visible, but a steady decline of bounce starting from about 35 % Impactor RH. According to Zobrist et al. (2008), the glass transition temperature of levoglucosan is 283.6 K. According to the definition, the viscosity of material defined as glass is 10^{12} Pas Debenedetti and Stillinger (2001). Thus at dry conditions at room temperature, the levoglucosan particles are ultraviscous, solid-like or rubbery particles rather than glass.

(Sperling, 2006; Franks, 1993). This, however does not inhibit the bounce, as solid-like or rubbery substance still restitute enough impaction energy for the bounce.

The bounce continues to decrease as the relative humidity increases and achieves minimum value around Impactor RH 60 %. Mikhailov et al. (2009) report that at the relative humidity of 60 % the particles are fully deliquesced, while partially deliquesced starting from 30 % RH, which corresponds well with our observation.

Amorphous particles with extremely high viscosity may exhibit large time constants in diffusive water uptake (Shiraiwa et al., 2011). The effect of increasing residence time, both in the ambient pressure and in the lowered pressure of the impactor was tested, but no effect was seen.

In general, the levoglucosan particle bounce curves behave as expected for an amorphous solids; the water uptake softens the particles and reduces the bounce steadily as the humidity is increased. This gradual softening is caused by the ability of water to function as a plasticizer for the levoglucosan particles (Sperling, 2006; Franks, 1993). This difference between the bounce behavior of ammonium sulfate and levoglucosan suggests that the distinction between crystalline and amorphous particles can be achieved with a rather simple measurement.

With levoglucosan the particle concentration was higher than with ammonium sulfate experiment, $\sim 10^4\,\mathrm{cm}^{-3}$. The effect of loading for the hydration run of the experiment seems larger, as the downscan point is lower than the previous points, but on the efflorescence part, with multiple points the effect seems to be minor, and the downscan points are close to within noise limits on average.

4 Conclusions

We presented a new method for studying the phase state of aerosol particles in atmospherically relevant particle size range. The reported method decouples any change in the charge transfer properties of the particles from the measurement signal, so the effect of particle phase changes on bounce alone can be investigated.

Two chosen test substances show expected behavior; ammonium sulfate has sharp phase changes and hysteresis at relative humidities reported previously. Likewise, amorphous levoglucosan particles have more continuous and reversible phase change in a wide humidity range. The reported method can be also used to study the phase changes caused by changes not visible on the particle size, for example by atmospheric chemical aging of the particles.

The current shortcomings of the method are drop in vapor pressure associated with the pressure drop when introducing the sample to the impactor, and the lack of a quantitative connection of the bounce probability and the physical properties of the particles, such as elastic properties or viscosity. These issues are being investigated and are topics for future studies. The substrate loading effects can be managed with monitoring of the bounce with additional measurement points and proper concentration control and cleaning of the substrate.

The sensitivity of the method to the surface of the impacting particles is also of interest (see Fig. 4). The decrease of bounced fraction with ammonium sulfate suggests that the method can be used to test partial water uptake observed also on some other crystalline solids such as sodium chloride (Wise et al., 2008). The knowledge of the degree of deliquescence corresponding to the drop in bounce probability could allow for particle coating specific measurements and more thorough studies of impaction dynamics.

Another suitable use for the method is the differentiation between amorphous and crystalline forms of different materials. This measurement could be done not only with deliquescence with water but with for example temperature induced phase change, where similar behavior is present.

Acknowledgements. This work has been supported by Maj and Tor Nessling Foundation Grant 2012501.

Edited by: H. Herrmann

References

Bilde, M. and Svenningsson, B.: CCN activation of slightly soluble organics: the importance of small amounts of inorganic salt and particle phase, Tellus B, 56, 128–134, doi:10.1111/j.1600-0889.2004.00090.x, 2004.

Biskos, G., Paulsen, D., Russell, L. M., Buseck, P. R., and Martin, S. T.: Prompt deliquescence and efflorescence of aerosol nanoparticles, Atmos. Chem. Phys., 6, 4633–4642, doi:10.5194/acp-6-4633-2006, 2006.

Brooks, S. D., Wise, M. E., Cushing, M., and Tolbert, M. A.: Deliquescence behavior of organic/ammonium sulfate aerosol, Geophys. Res. Lett., 29(19), 1917, doi:10.1029/2002GL014733, 2002.

Dahneke, B.: The capture of aerosol particles by surfaces, Journal of colloid and interface science, 37, 342–353, 1971.

Debenedetti, P. and Stillinger, F.: Supercooled liquids and the glass transition, Nature, 410, 259–267, 2001.

Franks, F.: Solid aqueous solutions, Pure and applied chemistry, 65, 2527–2538, 1993.

Hori, M., Ohta, S., Murao, N., and Yamagata, S.: Activation capability of water soluble organic substances as CCN, J. Aerosol Sci., 34, 419–448, doi:10.1016/S0021-8502(02)00190-8, 2003.

Hudson, J.: Cloud condensation nuclei, J. Appl. Meteorol., 32, 596–607, 1993.

Kelly, W. and McMurry, P.: Measurement of Particle Density by Inertial Classification of Differential Mobility Analyzer–Generated Monodisperse Aerosols, Aerosol Sci. Technol., 17, 199–212, 1992.

Keskinen, J., Marjamäki, M., Virtanen, A., Mäkelä, T., and Hillamo, R.: Electrical calibration method for cascade impactors, J. Aerosol Sci., 30, 111–116, doi:10.1016/S0021-8502(98)00026-3, 1999.

Lide, D.: CRC handbook of chemistry and physics, CRC Press, 2008.

Liu, B., Pui, D., Whitby, K., Kittelson, D., Kousaka, Y., and McKenzie, R.: The aerosol mobility chromatograph: a new detector for sulfuric acid aerosols, Atmos. Environ., 12, 99–104, 1978.

Marcolli, C. and Krieger, U. K.: Phase Changes during Hygroscopic Cycles of Mixed Organic/Inorganic Model Systems of Tropospheric Aerosols, The Journal of Physical Chemistry A, 110, 1881–1893, doi:10.1021/jp0556759, 2006.

Mikhailov, E., Vlasenko, S., Martin, S. T., Koop, T., and Pöschl, U.: Amorphous and crystalline aerosol particles interacting with water vapor: conceptual framework and experimental evidence for restructuring, phase transitions and kinetic limitations, Atmos. Chem. Phys., 9, 9491–9522, doi:10.5194/acp-9-9491-2009, 2009.

Onasch, T., Siefert, R., Brooks, S., Prenni, A., Murray, B., Wilson, M., and Tolbert, M.: Infrared spectroscopic study of the deliquescence and efflorescence of ammonium sulfate aerosol as a function of temperature, J. Geophys. Res., 104, 21317–21326, 1999.

Pope, F. D., Dennis-Smither, B. J., Griffiths, P. T., Clegg, S. L., and Cox, R. A.: Studies of Single Aerosol Particles Containing Malonic Acid, Glutaric Acid, and Their Mixtures with Sodium Chloride. I. Hygroscopic Growth, The Journal of Physical Chemistry A, 114, 5335–5341, doi:10.1021/jp100059k, pMID: 20361768, 2010.

Rader, D. and McMurry, P.: Application of the tandem differential mobility analyzer to studies of droplet growth or evaporation, J. Aerosol Sci., 17, 771–787, 1986.

Roberts, G. and Nenes, A.: A continuous-flow streamwise thermal-gradient CCN chamber for atmospheric measurements, Aerosol Sci. Tech., 39, 206–221, 2005.

Rogers, L. and Reed, J.: The adhesion of particles undergoing an elastic-plastic impact with a surface, Journal of Physics D: Applied Physics, 17, 677–689, 1984.

Romakkaniemi, S., Hämeri, K., Väkevä, M., and Laaksonen, A.: Adsorption of Water on 8Å15 nm NaCl and (NH4)2SO4 Aerosols Measured Using an Ultrafine Tandem Differential Mobility Analyzer, The Journal of Physical Chemistry A, 105, 8183–8188, doi:10.1021/jp010647l, 2001.

Rosenørn, T., Kiss, G., and Bilde, M.: Cloud droplet activation of saccharides and levoglucosan particles, Atmos. Environ., 40, 1794–1802, doi:10.1016/j.atmosenv.2005.11.024, 2006.

Seinfeld, J., Pandis, S., and Firm, K.: Atmospheric chemistry and physics: from air pollution to climate change, Wiley New York, 1998.

Shiraiwa, M., Ammann, M., Koop, T., and Pöschl, U.: Gas uptake and chemical aging of semisolid organic aerosol particles, Proceedings of the National Academy of Sciences, 108, 11003–11008, doi:10.1073/pnas.1103045108, 2011.

Sperling, L.: Introduction to physical polymer science, Wiley Online Library, 2006.

Virtanen, A., Joutsensaari, J., Koop, T., Kannosto, J., Yli-Pirilä, P., Leskinen, J., Mäkelä, J., Holopainen, J., Pöschl, U., Kulmala, M., Worsnop, D. R., and Laaksonen, A.: An amorphous solid state of biogenic secondary organic aerosol particles, Nature, 467, 824–827, 2010.

Wise, M., Martin, S., Russell, L., and Buseck, P.: Water uptake by NaCl particles prior to deliquescence and the phase rule, Aerosol Sci. Technol., 42, 281–294, 2008.

Zahardis, J. and Petrucci, G. A.: The oleic acid-ozone heterogeneous reaction system: products, kinetics, secondary chemistry, and atmospheric implications of a model system – a review, Atmos. Chem. Phys., 7, 1237–1274, doi:10.5194/acp-7-1237-2007, 2007.

Zobrist, B., Marcolli, C., Pedernera, D. A., and Koop, T.: Do atmospheric aerosols form glasses?, Atmos. Chem. Phys., 8, 5221–5244, doi:10.5194/acp-8-5221-2008, 2008.

Publication IV

E Saukko, AT Lambe, P Massoli, T Koop, JP Wright, DR Croasdale, DA Pedernera, TB Onasch, A Laaksonen, P Davidovits, DR Worsnop and A Virtanen Humidity-dependent phase state of SOA particles from biogenic and anthropogenic precursors *Atmospheric Chemistry and Physics*, 12(16):7517–7529, 2012.

Atmos. Chem. Phys., 12, 7517–7529, 2012
www.atmos-chem-phys.net/12/7517/2012/
doi:10.5194/acp-12-7517-2012

Atmospheric Chemistry and Physics

Humidity-dependent phase state of SOA particles from biogenic and anthropogenic precursors

E. Saukko[1], A. T. Lambe[2,3], P. Massoli[3], T. Koop[4], J. P. Wright[2], D. R. Croasdale[2], D. A. Pedernera[4,*], T. B. Onasch[2,3], A. Laaksonen[5,6], P. Davidovits[2], D. R. Worsnop[3,7], and A. Virtanen[1,6]

[1]Department of Physics, Tampere University of Technology, Tampere, Finland
[2]Chemistry Department, Boston College, Chestnut Hill, MA, USA
[3]Aerodyne Research Inc., Billerica, MA, USA
[4]Faculty of Chemistry, Bielefeld University, Bielefeld, Germany
[5]Finnish Meteorological Institute, Helsinki, Finland
[6]Department of Applied Physics, University of Eastern Finland, Kuopio, Finland
[7]Division of Atmospheric Sciences, Department of Physics, University of Helsinki, Helsinki, Finland
[*]now at: Faculty of Mathematics, Astronomy and Physics, National University of Córdoba, Córdoba, Argentina

Correspondence to: A. Virtanen (annele.virtanen@uef.fi)

Received: 22 December 2011 – Published in Atmos. Chem. Phys. Discuss.: 8 February 2012
Revised: 16 July 2012 – Accepted: 7 August 2012 – Published: 17 August 2012

Abstract. The physical phase state (solid, semi-solid, or liquid) of secondary organic aerosol (SOA) particles has important implications for a number of atmospheric processes. We report the phase state of SOA particles spanning a wide range of oxygen to carbon ratios (O / C), used here as a surrogate for SOA oxidation level, produced in a flow tube reactor by photo-oxidation of various atmospherically relevant surrogate anthropogenic and biogenic volatile organic compounds (VOCs). The phase state of laboratory-generated SOA was determined by the particle bounce behavior after inertial impaction on a polished steel substrate. The measured bounce fraction was evaluated as a function of relative humidity and SOA oxidation level (O / C) measured by an Aerodyne high resolution time of flight aerosol mass spectrometer (HR-ToF AMS).

The main findings of the study are: (1) biogenic and anthropogenic SOA particles are found to be amorphous solid or semi-solid based on the measured bounced fraction (BF), which was typically higher than 0.6 on a 0 to 1 scale. A decrease in the BF is observed for most systems after the SOA is exposed to relative humidity of at least 80 % RH, corresponding to a RH at impaction of 55 %. (2) Long-chain alkanes have a low BF (indicating a "liquid-like", less viscous phase) particles at low oxidation levels ($BF < 0.2 \pm 0.05$ for $O/C = 0.1$). However, BF increases substantially upon increasing oxidation. (3) Increasing the concentration of sulphuric acid (H_2SO_4) in solid SOA particles (here tested for longifolene SOA) causes a decrease in BF levels. (4) In the majority of cases the bounce behavior of the various SOA systems did not show correlation with the particle O / C. Rather, the molar mass of the gas-phase VOC precursor showed a positive correlation with the resistance to the RH-induced phase change of the formed SOA particles.

1 Introduction

The direct and indirect effects of aerosol particles on the Earth's radiative budget remain the largest source of uncertainty in climate change modeling (IPCC, 2007, ch. 2). In many locations, organic matter (OM) forms up to 90 % of observed submicron aerosol particulate mass, and secondary organic aerosol (SOA) represents up to half of the organic fine fraction (Jimenez et al., 2009; Hallquist et al., 2009).

SOA particles are formed from oxidation of gas-phase organic precursors. The volatility of the VOCs decreases as their functionalization and thus binding ability increases (Donahue et al., 2012), causing their vapor pressure to decrease until the gaseous compounds either condense on existing particles or nucleate to form new particles. The SOA

formation process under natural conditions is complicated and it involves a multitude of gaseous precursors and a greater number of particle product compounds. Up to now, the modeling of formation and aging of SOA has been mostly based on gas-particle equilibrium partitioning of volatile and semivolatile species (Pankow, 1994; Kanakidou et al., 2005). This implies fast enough condensed phase diffusion rates to keep the condensed phase in equilibrium with the gas phase as the particles' size increases and the concentration of VOCs decreases.

However, several recent studies show that at least under some conditions natural and laboratory-produced SOA particles have an amorphous solid state (Virtanen et al., 2010; Cappa and Wilson, 2011; Vaden et al., 2011). The solid amorphous state of SOA particles has important implications for a number of atmospheric processes. First, a solid phase implies surface-confined chemistry and kinetic limitations to achieve equilibrium partitioning between the gas phase and the particle phase. More importantly, chemical reactions are impeded in viscous aerosol particles (Zahardis and Petrucci, 2007; Shiraiwa et al., 2011; Pfrang et al., 2011; Ziemann, 2010), because mass transport (diffusion) of reactants within the aerosol particle bulk may become the rate limiting step. Shiraiwa et al. (2011) showed that these kinetic limitations can increase the chemical lifetime of (semi-)solid particles by more than an order of magnitude. The water uptake of highly viscous SOA particles may also be diminished or even fully inhibited, in particular at low temperatures, with implications for the particles' size and scattering properties and their direct effect on climate (Zobrist et al., 2008; Murray, 2008; Mikhailov et al., 2009; Koop et al., 2011). The particles in a glassy state can also catalyse ice formation in cirrus conditions and thus have significant implications on the water-particle interactions at upper atmosphere (Murray et al., 2010).

All recent studies reporting a solid phase of SOA particles (Virtanen et al., 2010; Cappa and Wilson, 2011; Vaden et al., 2011) have focused on studying the properties of laboratory or ambient SOA in dry conditions (RH < 40 %). In order to assess how general is the occurrence of the amorphous solid state of the SOA, and how other factors might affect particle phase state, we report a systematic characterization of the phase of laboratory SOA as a function of O / C and relative humidity (RH). The SOA particles were generated from the *OH oxidation of several atmospherically relevant anthropogenic and biogenic precursors. A low pressure impactor (LPI) equipped with an optical counting arrangement provided a measurement of the phase of the SOA particles, based on the idea that "liquid-like" particles are collected on the impactor stage with minimal bounce, whereas detection of particles downstream of the impactor indicates that particles are bouncing off of the impactor stage and suggests the presence of an amorphous semi-solid or solid state. Other chemical and microphysical properties of the SOA particles were characterized with a Scanning Mobility Particle Sizer (SMPS) (TSI), Cloud Condensation Nuclei Counter (CCNC), and High-Resolution Time-of-Flight Aerosol Mass Spectrometer (HR-ToF-AMS).

2 Experimental

2.1 SOA particle generation

SOA particles were generated with a Potential Aerosol Mass (PAM) flow tube reactor, which is a horizontal 15 l glass cylindrical chamber 46 cm long × 22 cm ID. The details of the reactor used are described in Lambe et al. (2011a). The reactor is capable of simulating atmospheric oxidation timescales of days to weeks with actual residence times of minutes. Previous studies have shown that the PAM reactor can produce SOA at a level of oxidation that is atmospherically-relevant (Massoli et al., 2010; Lambe et al., 2011b, 2012) but unattainable by conventional smog chamber techniques that are limited to ∼ 1 day of equivalent atmospheric oxidation (e.g. Ng et al., 2010).

SOA was generated via gas-phase oxidation of precursors (shown in Fig. 1), followed by homogeneous nucleation. Volatile organic compound (VOC) precursors used in this study were isoprene and α-pinene. VOC precursors were prepared in compressed gas cylinders or in glass bubblers and introduced into the PAM reactor with N_2 carrier gas at controlled rates using a mass-flow controller. Intermediate volatility organic compound (IVOC) precursors used in this study were *n*-heptadecane, longifolene, and naphthalene. With the exception of naphthalene, IVOCs were introduced into the carrier gas flow using a permeation tube placed in a temperature-controlled oven. Naphthalene vapor was introduced by flowing N_2 over solid naphthalene placed in a Teflon tube.

Organic species were transported through the PAM reactor by a carrier gas consisting of 8.5 lpm N_2 and 0.5 lpm O_2. The average species residence time in the PAM reactor was typically 100 s. Four mercury lamps (BHK Inc.) with peak emission intensity at $\lambda = 254$ nm were mounted in teflon-coated quartz cylindrical sleeves inside the chamber, and were continually purged with N_2.

OH radicals (*OH) were produced via the reaction O_3 + hν $\rightarrow O_2$ + $O(^1D)$ followed by the reaction $O(^1D)$ + H_2O $\rightarrow$ 2*OH. O_3 was generated by irradiating O_2 with a mercury lamp ($\lambda = 185$ nm) outside the PAM reactor. Oxygen ($O(^1D)$) radicals were produced by UV photolysis of O_3 inside the PAM reactor. The radical $O(^1D)$ then reacted with water vapor (introduced using a heated Nafion membrane humidifier; Perma Pure LLC) to produce *OH inside the PAM reactor. Most experiments were conducted at RH values ranging from 30 % to 40 %, depending on the temperature in the PAM reactor (22-32°C) at different UV lamp settings. At a given measured relative humidity, this parameter remained constant to within ±5 %.

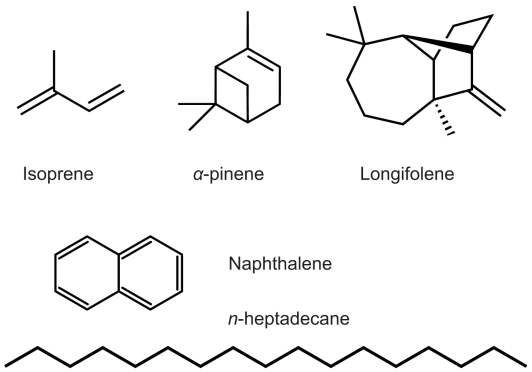

Fig. 1. Molecular structures of the VOC and IVOC gaseous precursors used to generate SOA for the experiment: biogenic precursors are in the top row, anthropogenic model precursors are on the bottom.

The *OH exposure, which is the product of the *OH concentration and the average residence time in the PAM reactor, was varied by changing the UV light intensity through stepping the voltage applied to the lamps between 0 and 110 V. The *OH exposure was determined indirectly by measuring the decay of SO_2 due to reaction with *OH in the PAM reactor. SO_2 calibration measurements were conducted as a function of UV lamp intensity and O_3 concentration (Lambe et al., 2011a). Typical *OH exposures ranged from 2.7×10^{11} to 2.2×10^{12} molec cm^{-3} s. These values are equivalent to 2 to 17 days of atmospheric oxidation assuming an average atmospheric *OH concentration of 1.5×10^6 molec cm^{-3} (Mao et al., 2009). However, we note that this equivalent "atmospheric age" may be a factor of 2 or more uncertain depending on the assumed ambient *OH concentration.

While *OH concentrations in these experiments (approximately 2.7×10^9 to 2.2×10^{10} molec cm^{-3}) are higher than ambient *OH concentrations, the integrated *OH exposures are similar. Previous work suggests that, to first order, extrapolation of flow tube reactor conditions (high [*OH], short exposure times) to atmospheric conditions (low [*OH], long exposure times) is reasonable (Renbaum and Smith, 2011). Even though both O_3 and *OH can oxidize organic species, *OH was the principal oxidant in all experiments except for selected studies, where experiments with O_3 as the oxidizing agent were conducted by turning the lamps off. Prior to each experiment, the PAM reactor was conditioned with *OH radicals until a particle background less than 10 particles cm^{-3} was attained.

In some experiments, internally mixed SOA – sulfuric acid particles were produced by introducing SO_2 along with the SOA precursor, which is oxidized by *OH to produce sulfuric acid (H_2SO_4) in the presence of water vapor (Seinfeld and Pandis, 1998, ch. 6.13).

2.2 Particles phase state measurement

The device used in this study to measure the particle bounce is described in detail in Saukko et al. (2012). The system consists of a low pressure impactor and a polished steel substrate. Size-selected aerosol is guided through a sampling cell (see Fig. 2) at low pressure until the system is stabilized, after which the cell is closed and re-pressurised to bring the sample to the working conditions of a TSI Ultrafine Water Condensation Particle Counter (WCPC), i.e. ambient pressure. This particle number concentration is compared to the particle concentration measured upstream of the impactor. The *bounced fraction* is the ratio of the particle concentrations measured after and before the impactor, divided by a similar ratio (baseline sample) obtained without the impaction substrate. The method is conceptually similar to that used by Virtanen et al. (2010), but the optical detection of particles employed here removes the effect of charge transfer processes. Accurate scales relating the bounced fraction to mechanical or other properties of the particles have not, however, been established yet.

The RH of the sampled aerosol is adjusted between 28 and 91 % RH by a Nafion humidifier (PermaPure). The Nafion capillaries are fed with a mixture of $\sim$100 % RH air from water-fed micro-pore humidifier (Enerfuel) and $<$5 % RH pressurized air. The aerosol sample flows around the Nafion capillaries and the water vapor is transferred from the humidifying flow. The output humidity is adjusted with the ratio of the saturated and $<$ 5 % RH airflows.

The RH history of the sampled aerosol is slightly more complicated than the simple humidification by the Nafion tube: as the aerosol enters the impactor, the upstage pressure is 690 kPa, which is approximately 70 % of the ambient pressure. Thus, the water vapour is diluted by expansion and the range of sample RH values upstream of the impactor (28 % to 91 % RH) corresponds to a range of reduced RH of 20 % to 64 % RH inside the impactor. The validity of this RH scaling is shown in Saukko et al. (2012), where deliquescence and efflorescence relative humidities for ammonium sulfate are obtained to within 3 % RH of literature values. This indicates that the temperature changes in impactor jet do not affect the relevant humidity inside the impactor. The equilibration time for the aerosol at this reduced RH is 0.9 s (Saukko et al., 2012), which at room temperature is sufficient for 100 nm particles to equilibrate with the gas phase humidity even if a semi-solid or solid state was obtained prior to entering the impactor (Koop et al., 2011; Zobrist et al., 2011). The particle sizes used in the experiments were between 105 and 160 nm in mobility diameter, and 130 to 230 nm in aerodynamic diameter.

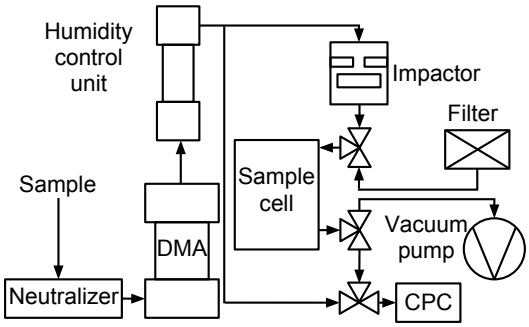

Fig. 2. The measurement system for the particle phase measurement.

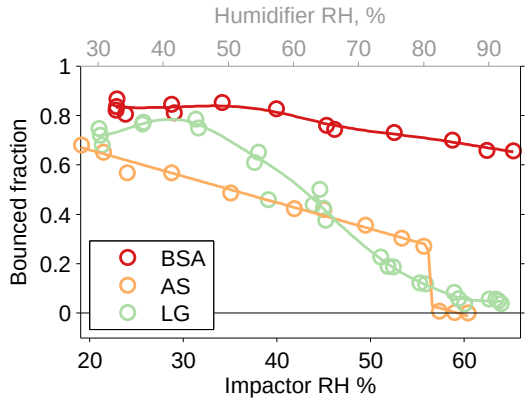

Fig. 3. Reference bounce characteristics of ammonium sulfate (AS) (crystalline), bovine albumin serum (BSA) (amorphous) and levoglucosan (LG) (amorphous).

2.3 SOA CCNC measurements

The CCN activity of SOA particles was measured with a continuous flow CCN counter (CCNC) (Roberts and Nenes, 2005; Lance et al., 2006). The PAM-generated SOA was size-selected using a TSI 3080 DMA prior to CCN number concentration measurements with the CCNC and total particle number concentration measurements with a CPC (TSI 3022A). CCN activation curves were generated by holding the particle size constant while systematically varying the CCNC column temperature gradient to obtain controlled water vapor supersaturation between 0.1–1.5 % or until 100 % activation was reached, as described in Massoli et al. (2010) and Lambe et al. (2011a). The CCN activity, κ, was calculated using the approach by Petters and Kreidenweis (2007). Selected dry mobility diameters ranged from 55 to 85 nm for SOA.

2.4 SOA elemental ratios

The chemical composition of the laboratory generated SOA were obtained with an Aerodyne HR-ToF-AMS (DeCarlo et al., 2006). Elemental analysis yielding oxygen-to-carbon (O / C) and hydrogen-to-carbon (H / C) ratios was performed on the high-resolution measurements using ToF-AMS analysis software (Squirrel and Pika: http://cires.colorado.edu/jimenez-group/ToFAMSResources/ToFSoftware/index.html).

The absolute accuracies for O / C and H / C, determined by comparison to laboratory standards (Aiken et al., 2007, 2008), are 31 % and 10 %, respectively. These values represent upper limits to the uncertainty of measurements for complex OA (Chhabra et al., 2010). The variability of the measurements can be captured by the precision error (standard deviation) which for these laboratory conditions was less than ±5 %. Table 1 shows the range of O / C ratio, H / C ratio and CCN κ values for the SOA particles that were studied in this work, along with the corresponding *OH exposures in the PAM reactor.

3 Results

Figure 3 shows the BF measured with the LPI for ammonium sulfate (AS), bovine albumine serum (BSA) and levoglucosan (LG) particles (Saukko et al., 2012). As can be seen in the figure, the bounce measured for AS particles decreases well below the deliquescence point. In Saukko et al. (2012) this is explained by the formation of water layer on the solid crystalline AS particle surface due to the adsorbed water. The behavior of BSA particles (nominally a non-crystalline amorphous solid) differs considerably from that of AS particles. The BSA bounce does not show similar clear decrease with increasing humidity. The difference in the BSA and AS behavior lies in the differences in material characteristics: adsorbed water forms a layer on the surface of solid crystalline, stable structured AS particles, while in the case of amorphous solid BSA particles the adsorbed water molecules can diffuse into the particle bulk. According to Shiraiwa et al. (2011) the estimated viscosity for BSA is 10^{12}–10^{10} Pas in the studied viscosity range (the viscosity of glassy material is 10^{12} Pas).

Finally, the BF behavior of levoglucosane particles (LG) with increasing RH is shown. Amorphous levoglucosane particles show a gradual decrease in bounce with increasing RH in the range 30–60 %. This decrease in bounce can be related to the gradual humidity induced phase transition described in Mikhailov et al. (2009). Despite these three different compounds show a clear trend in BF with respect to RH, it is currently not possible (and out of the scope of this paper) to define specific and absolute BF threshold values to describe possible particle phase transitions (i.e. from solid amorphous to semi-solid amorphous to liquid).

Table 1. SOA generation parameters and measurements. The third α-pinene line with *OH exposure of 0 refers to an ozonolysis experiment.

Precursor(s)	*OH exposure (10^{11}molec cm^{-3}s)	O / C	H / C	κ	Std. dev. O / C.	Std. dev. H / C
Isoprene	22.0	0.62	1.7	0.21	0.003	0.007
Isoprene	7.82	0.61	1.75	0.15	0.002	0.005
α-pinene	15.5	0.69	1.36	0.19	0.004	0.004
α-pinene	11.4	0.55	1.45	0.17	0.002	0.003
α-pinene	0	0.34	1.52	0.14	0.003	0.001
Longifolene	22.0	0.58	1.31	0.19	0.003	0.002
Longifolene	2.77	0.14	1.53	0.05	0.002	0.001
Longifolene+SO_2	22.0	0.55	1.77	0.19	0.003	0.004
Longifolene+SO_2	22.0	0.57	1.74	0.17	0.006	0.004
Longifolene+SO_2	22.0	0.75	1.49	0.21	0.004	0.003
Naphthalene	22.0	1.41	0.90	0.18	0.005	0.002
Naphthalene	7.82	0.68	0.97	0.15	0.006	0.005
Naphthalene	2.77	0.35	0.92	0.16	0.003	0.004
n-heptadecane	11.4	0.30	1.69	0.12	0.003	0.006
n-heptadecane	7.82	0.20	1.78	0.11	0.002	0.003
n-heptadecane	4.95	0.15	1.85	0.04	0.001	0.003
n-heptadecane	2.77	0.10	1.92	0.01	0.001	0.003

Semi-solid/solid amorphous materials have very wide viscosity range. By definition the viscosity of the liquids is < 102 Pas, viscosity of the semisolids varies from 10^2 Pas up to 10^{12} Pas. Material having viscosity $> 10^{12}$ Pas can be considered as "glass" (e.g. Koop et al., 2011). Thus "more solid" refers to the (amorphous) material having higher viscosity and higher BF value than some other (amorphous) material.

3.1 Phase state and humidity-induced phase transitions of biogenic SOA particles

The fraction of bounced SOA particles formed from biogenic precursors (isoprene, α-pinene, and longifolene) as a function of RH in the impactor is shown in Fig. 4. As mentioned in Sect. 2.2, the relative humidity in the impactor is approximately 30 % lower than the initial humidified sample RH because of the pressure drop in the impactor stage. Therefore we define the RH value inside the impactor as the impactor RH, or RH_I.

For $20\,\% < RH_I < 50\,\%$, the bounced fraction of biogenic SOA particles was between 0.65 and 0.9 in all cases and for all O / C levels ranging from 0.14 to 0.69. Thus, we conclude that biogenic SOA particles generated in the PAM reactor are solid or semi-solid at $RH_I < 50\,\%$ over the range of measured conditions. For $RH_I > 50\,\%$, the measured BF of biogenic SOA particles decreased. This decrease in bounce suggests a decrease in viscosity as a result of a humidity-induced phase change from solid to liquid-like particles. It should be noted that in the case of highly viscous, glassy particles the possibility of formation of liquid layer of adsorbed water on the particle surface can not be entirely excluded. The formation of such a layer may then reduce the bounced fraction of the particles. The HTDMA studies of SOA particles, however show modest but gradual particle water uptake with increasing humidity (Varutbangkul et al., 2006; Prenni et al., 2007). This behaviour suggests that water uptake is not pure adsorption only, but the water is able to diffuse to the particle bulk.

The decrease in BF above RH_I of 55 % was most pronounced for isoprene SOA particles for which BF decreased to 0.25 ± 0.1 at $RH_I = 65\,\%$ (Fig. 4, top panel). The BF vs RH_I relatiosnhip in the case of isoprene could only be explored for one O / C value (0.61). However, similar measurements of bounced fraction as a function of RH_I performed for SOA particles generated from α-pinene (Fig. 4 middle panel) and longifolene (Fig. 4 lower panel) showed that there was no systematic difference in the measured bounced fraction for as a function of O / C ratio (O / C = 0.34 to 0.69 for α-pinene and 0.14 to 0.58 for longifolene SOA). For SOA particles generated from α-pinene, the bounced fraction decreased from 0.75 ± 0.1 (at $RH_I \sim 22\,\%$) to 0.55 ± 0.1 (at $RH_I = 65\,\%$). For SOA particles generated from longifolene, the bounced fraction decreased from 0.78 ± 0.05 to 0.7 ± 0.1 across the same RH_I range. These decreases in bounce were significantly less than for SOA produced from isoprene, suggesting that phase changes were less pronounced.

It appears that for these three biogenic SOA types, the RH_I-dependent decrease in BF became less pronounced with increasing molar mass of the precursor. The observation for α-pinene and levoglucosan SOA of high bounce at the higher RHs are in line with the growth factors reported by Varutbangkul et al. (2006) (1.01–1.02 for monoterpenes, less than 1.01 for most sesquiterpenes at 50 % RH), as well as the observed higher bounce of longifolene versus α-pinene SOA.

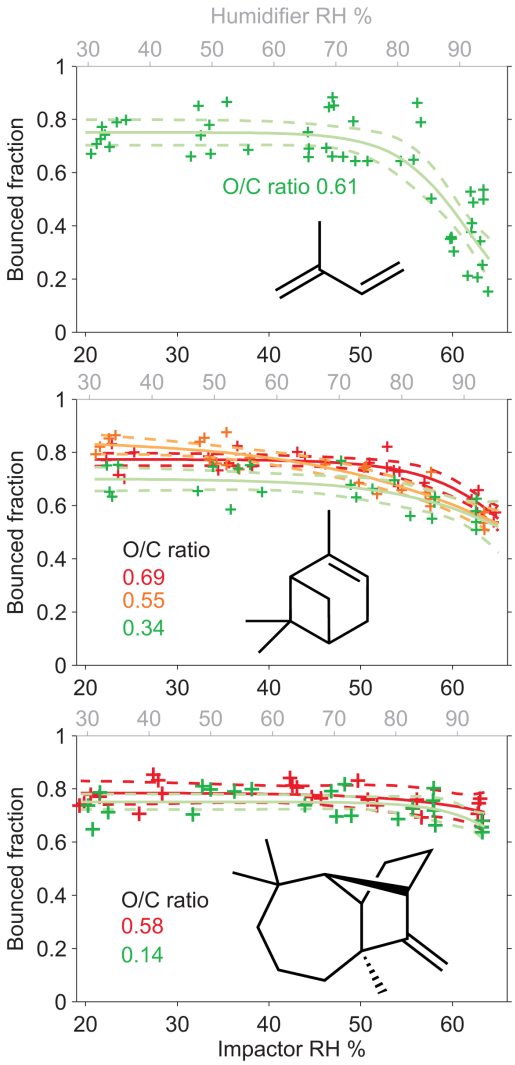

Fig. 4. Bounce behavior of SOA from photo-oxidation experiments of biogenic precursors, solid lines are sigmoid fits to guide the eye, dashed lines give the 95 % confidence bounds for the fits. Upper panel: isoprene SOA, middle panel: α-pinene SOA, lower panel: longifolene SOA.

3.2 Phase state and humidity-induced phase transitions of mixed SOA-sulphuric acid particles

In most cases, ambient oxygenated organic aerosol (OOA) is mixed with inorganic species such as particulate nitrate and sulphate, (e.g. Jimenez et al., 2009), which may influence the viscosity or phase of the aerosols. In a separate set of experiments, we measured the bounced fraction of SOA/sulphuric acid mixtures generated from the simultaneous oxidation of longifolene and SO_2 in the PAM reactor. The longifolene system was chosen because the bounced fraction of longifolene SOA resulted particularly insensitive to increasing RH_I (cf. Fig. 4). Therefore, any changes in particle bounce are due to changes in the organics-to-sulphate ratio of the particles (measured by the HR-ToF-AMS).

It is important to consider that in the case of multi-component inorganic-organic particles it is possible that a liquid-liquid phase separation may occur (Marcolli and Krieger, 2006; Ciobanu et al., 2009; Bertram et al., 2011; Song et al., 2012; Zuend and Seinfeld, 2012). Since we cannot distinguish phase separation in the 100 nm particles studied here, we discuss below whether the observed bounce behavior is consistent with one or both of the two possible cases, i.e. liquid-liquid phase-separated aerosol particles and well-mixed aerosol particles.

Figure 5 shows the measured bounced fraction as a function of RH_I for longifolene SOA-sulphate mixtures, with sulphate mass fractions ranging from 0.09 to 0.36. The sulfate fraction is calculated as the fraction of sulfate mass with respect to the measured AMS total mass (mostly ORG, with small concentrations of NH_4 within instrumental noise). The O / C measured for the pure longifolene SOA was 0.58, and with sulfate fractions of 0.9, 0.20 and 0.36 the respective O / C-ratios were 0.55, 0.57 and 0.75 while keeping other parameters constant.

As is evident from Fig. 5, a sulphate mass fraction of 0.09 does not decrease the particle bounce relative to that of pure longifolene SOA. However, increasing the sulphate mass fraction to 0.20 results in a continual decrease in particle bounced fraction as a function of RH_I, with the sharpest decrease at RH_I 55 %, to a final bounced fraction of 0.1 ± 0.05 at $RH_I = 62$ %. This suggests a solid-to-liquid phase transition of the mixed SOA/sulfate particles in this range of RH_I. Increasing the sulphate mass fraction to 0.36 results in a constant particle bounced fraction 0.10 ± 0.05 for $20\,\% < RH_I < 62\,\%$, suggesting a liquid-like behavior over the entire RH_I range investigated.

The HR-ToF-AMS particle time-of-flight measurements confirmed that the SOA and sulphate were internally mixed in all cases and particle sizes. As noted above, liquid-liquid phase separation may occur in aerosol particles consisting of organic and inorganic species. In the present SA/SOA case, this would result in one phase consisting predominantly of SA with minor contributions from organics, and another phase that is organic-rich but also contains significant SA (typically between 10 to 30 % of dry solute mass, see Song et al., 2012). Moreover, the organic phase is very likely to constitute the outer phase, while the inorganic SA phase is more likely to be located in the core of a particle due to a minimization of the overall surface energy of the particle (Krieger et al., 2012). At room temperature SA/water mixtures are liquid over the entire concentration range. Hence,

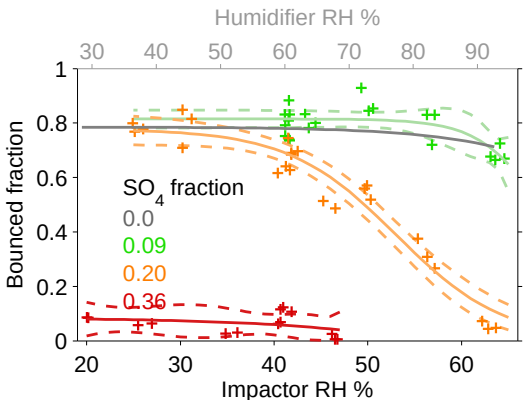

Fig. 5. Addition of SO_2 to precursor flow for longifolene SOA experiment decreases the phase transition relative humidity. The SO_4 fraction indicates the fraction of SO_4 with respect to the total measured AMS mass ($ORG+SO_4+NO_3+NH_4$).

the particle core may be liquid for the entire range of investigated humidity studied here. In contrast, the organic-rich outer "shell" consisting of SOA/SA mixtures might be in a solid, semi-solid or liquid state depending on experimental conditions. For the case of a sulphate fraction of 0.09 it appears that the bounce is very similar to that of pure SOA particles suggesting that neither the minor inorganic fraction contained in the outer shell nor the liquid SA core significantly decrease the bounce of the particle. For a larger SA fraction of 0.2 the reduced bounce at higher humidity suggests at least a partial liquefaction. This might have two causes. First, the liquid core is larger due to an enhanced SA content when compared to the 0.09 SA case and, hence, more significant water uptake occurs at higher humidity. Secondly, in addition a larger SA content in the organic outer shell might reduce its viscosity when compared to the pure SOA particle phase. Finally, at an SA content of 0.36 the particles show a liquid-like bounced fraction over the entire humidity range. Again this might indicate an even larger SA core that is liquid-like even at low humidity and in addition a possible further increased SA content in the organic shell, also further reducing the outer organic shell's viscosity even at lower humidity.

The behavior of longifolene SOA/sulphuric acid mixtures seen in Fig. 5 might therefore be attributed to the particles' SA core being liquid, with potential effects of SA also in the organic shell. As far as the liquid content is concerned, a very rough estimate of the liquid content (water and sulfuric acid) can be made by assuming phase separation and water uptake of sulphuric acid according to Kim et al. (1994). Based on this, the water+H_2SO_4-volume concentration of the particles is above 60 % for the case of 0.36 SO_4 fraction, and below 31 % for the case of 0.09 SO_4 fraction. The intermediate case of SO_4 fraction of 0.20 has the water+H_2SO_4-volume concentration ranging from 0.46 at 30 % RH to 0.52 at 0.52 at 60 % RH_I.

For these reasons, it is useful to discuss how increasing sulphate content would affect the phase state of well-mixed SOA/SA particles. In principle, empirical mixing laws that are based on data from various mixtures of a range of different compounds predict that the glass transition temperature (T_g) of a mixture is between the T_g's of the individual compounds (Koop et al., 2011). However, this has not been confirmed so far for a sulphuric acid /organic mixture. Therefore, the principle behavior of well-mixed organic/sulphate solutions was further examined using differential scanning calorimetry (DSC) (Höhne et al., 2003) by measuring T_g of a model mixtures of glucose and sulphuric acid, for experimental details see Zobrist et al. (2008). (We were not able to use SOA material for such purposes, because the SOA sample mass required for such measurements is in the microgram range and thus far beyond that available from the PAM reactor.) Figure 6 shows that increasing the mass fraction of sulphuric acid decreases the glass transition temperature of the mixture at constant solute mass fraction (i.e. constant water content). Our results are therefore consistent with studies showing that mixing compounds with different T_g values normally results in a glass transition temperature of the mixture that is between T_g values of the individual mixture components (Zobrist et al., 2008; Koop et al., 2011).

Accordingly, because sulphuric acid shows a lower T_g than the SOA organics investigated here, its presence would soften the SOA particles. Moreover, owing to its larger hygroscopicity sulphuric acid (and similarly ammonium bisulfate or ammonium sulfate) also leads to an increase in water content of the particles at the same RH, further softening the particles, thereby leading to a humidity-induced liquefaction of the particles at humidities that are lower when compared to those of pure SOA particles. This is shown schematically in the bottom panel of Fig. 6 , which is a sketch of T_g versus equilibrium relative humidity for various organics and/or sulphuric acid mixtures. When humidity is increased at constant temperature (black arrow) the pure organic (green curve) with the highest glass transition temperature in the dry state, T_g (dry), shows a humidity-induced liquefaction at the highest RH (intersection between the black arrow and the green T_g curve), close to the upper end of investigated RH range. In contrast, pure sulphuric acid or a mixture with high sulphuric acid content (red) show the lowest T_g (dry) and, hence, are liquid over the full range of investigated RH without any bounce. Finally, a mixture with a high organics content (orange) shows an intermediate T_g (dry), thus liquefying at an intermediate RH in the middle of the investigated RH range.

We conclude that both principle types of particle morphology, i.e. liquid-liquid phase-separated particles and also well-mixed particles are able to describe the observed bounce behavior of SOA/SA particles. We further note, that if sulphuric

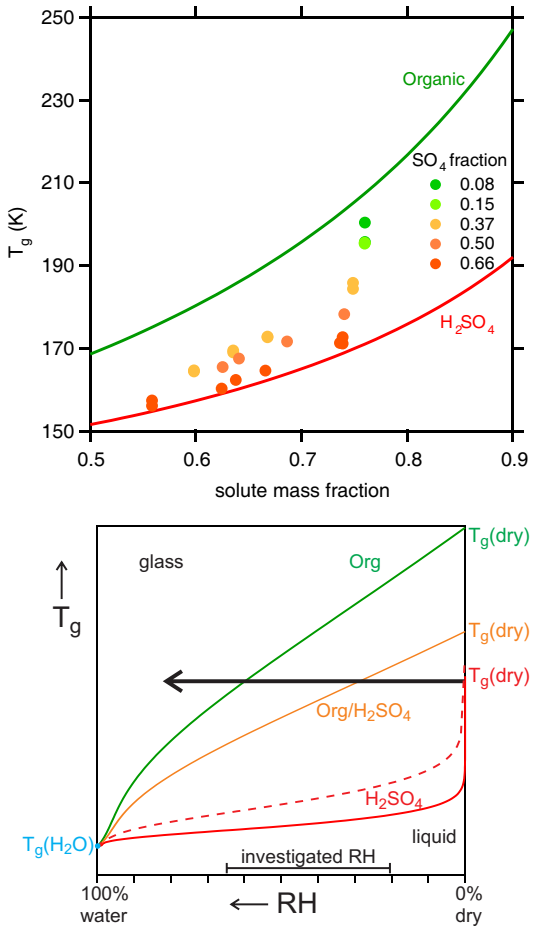

Fig. 6. Top: addition of H_2SO_4 to an organic (here: glucose) leads to a strong reduction in T_g at the same water content (Pedernera, 2008). The effect is even more pronounced when plotted as a function of relative humidity (because of the different hygroscopicities of organics and sulfate). The bottom panel is a schematic picture of T_g versus equilibrium relative humidity for various organic/sulphuric acid mixtures.

acid plays an important role in atmospheric nucleation processes, as suggested by Sipilä et al. (2010) and Kirkby et al. (2011), our results suggest that freshly nucleated particles containing appreciable amounts of sulphuric acid are initially liquid. The discussion above indicates that this might be true independently of whether the sulphate and organic fraction are phase-separated or not. As the particles grow via condensation of oxygenated organic species, the mass fraction and, hence, the effective T_g might increase and the particles may solidify (Virtanen et al., 2010, 2011).

3.3 Phase state and humidity-induced phase transitions of anthropogenic SOA particles

In addition to bounce measurements of biogenic SOA particles, we also studied the bounce behavior of anthropogenic SOA particles generated from the oxidation of naphthalene and *n*-heptadecane. Naphthalene was chosen as a model aromatic precursor, and *n*-heptadecane as a model aliphatic precursor. The upper panel in Fig. 7 shows the bounced fraction of SOA particles generated from naphthalene as a function of RH_I. The bounce behavior for naphthalene SOA is similar to that of α-pinene SOA, with a decrease in bounced fraction from 0.65 ± 0.1 (average value among several O / C ratios) at $RH_I < 50\,\%$ to 0.4 ± 0.1 at $RH_I = 64\,\%$.

The lower panel in Fig. 7 shows the bounce behavior of *n*-heptadecane SOA as a function of RH_I. Unlike the other systems that were studied, the bounced fraction of SOA particles generated from *n*-heptadecane was strongly correlated with the O / C ratio of the SOA. At O / C = 0.10, the SOA bounced fraction was low (0.2 ± 0.05) and was unaffected by RH_I, implying an organic liquid-like phase. At O / C = 0.15, the bounced fraction was above 0.5 at $RH_I = 20\,\%$ and exhibited a monotonic decrease to slightly below 0.3 at $RH_I = 64\,\%$. At O / C = 0.20, a constant bounced fraction of 0.55 ± 0.05 was measured for $RH_I < 50\,\%$, with a decrease in bounced fraction to 0.4 at $RH_I = 64\,\%$. Finally, at an O / C ratio of 0.30, we measured a constant bounced fraction of above 0.8 at $RH_I < 50\,\%$ before the bounced fraction decreased to below 0.7 at $RH_I = 60\,\%$. This bounce behavior was similar to that observed in the other systems that were studied. Thus, SOA particles generated from *n*-heptadecane were initially liquid-like at low O / C ratio and solidified with increasing O / C ratio.

In order to rationalize the observed behavior of the anthropogenic SOA particles, in Fig. 8 we show the predicted T_g values for naphthalene (~ 247 K) and *n*-heptadecane (~ 207 K). These T_g values were predicted from the observed dependence of T_g upon melting temperature T_m, i.e. $T_g \approx 0.7 \times T_m$ (Koop et al., 2011). Also shown in Fig. 8 are the predicted T_g for various oxygenated compounds originating from the parent structure of *n*-heptadecane (red) and naphthalene (blue). The red-shaded and blue-shaded vertical bars indicate the range of investigated O / C ratio for each SOA. The grey horizontal bar indicates the suggested turnover from liquid behavior at room temperature (no bounce) for substances with a T_g less than ~ 250 K to solid behavior (bounce) for substances with a T_g above ~ 270 K.

The predicted T_g of naphthalene is already close to 250 K, and just adding one O-atom (e.g. 1-naphthol and 2-naphthol, with an O / C ratio of 0.1) might initiate (partial) bounce in such particles at room temperature. Further increase in O / C ratio to values between 0.2–0.4 leads to predicted T_g values from close to room temperature up to significantly beyond room temperature, implying full bounce. Even though there is considerable scatter in these data, it is obvious that in the

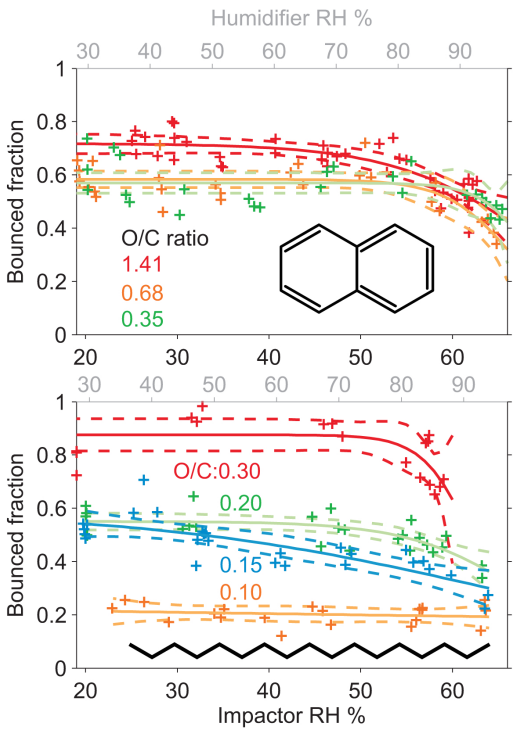

Fig. 7. Bounce behavior of SOA from photo-oxidation of naphthalene (upper panel) and *n*-heptadecane (lower panel).

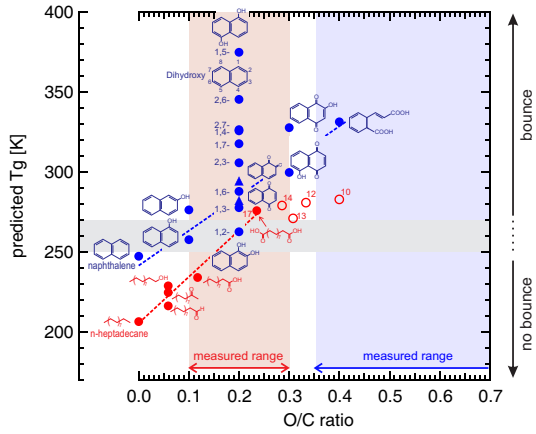

Fig. 8. Predicted glass transition temperatures T_g as a function of the molecular O / C ratio for various oxygenated compounds originating from the parent structure of *n*-heptadecane (red) and naphthalene (blue). Open circles are predicted T_g for *n*-dicarboxylic acids with the number of C-atoms indicates for each point. For details see text.

measured range of O / C > 0.35 (light blue shading) nearly all substances are expected to bounce independently of their actual O / C ratio.

In contrast, the predicted T_g for *n*-heptadecane and those of mildly oxygenated compounds (1-alcohol, 1-aldehyde, 2-ketone) with an O / C ratio of 0.06 are so low that these compounds are liquid at room temperature and, thus, would not show bounce. Only at significant oxygenation (e.g. the 1,17-dicarboxylic acid, with an O / C ratio of 0.24) bounce is to be expected. We note that oxygenation of *n*-heptadecane is likely to lead to fragmentation (Lambe et al., 2012). However, it appears that at least an oxidation to a dicarboxylic acid is required for bounce, more or less independently of the length of the remaining carbon chain (see red open circles with number of C-atoms indicated). For *n*-heptadecane, the T_g goes from ∼ 207 K to greater than ∼ 280 K with increasing O / C (pink shading), in agreement with the measurements.

Similarly to previous studies that suggest a correlation of bounced fraction with the glass transition temperature (Virtanen et al., 2010) the same correlation is observed here. Based on an idealized comparison of predicted T_g values shown in Fig. 8, it is no surprise that *n*-heptadecane SOA shows a "bounce transition" with increasing O / C in the investigated range while naphthalene SOA bounced at all investigated O / C ratios.

3.4 Discussion

The main factors affecting the bounce behavior of SOA particles are likely their viscosity, elasticity and the surface adhesion. For amorphous particles, the viscosity and mechanical properties are sensitive to the glass transition temperature (Shiraiwa et al., 2011; Koop et al., 2011). The glass transition temperature and thus the viscosity at constant temperature are sensitive to the solvent concentration, molar mass and the functional groups of the particulate matter (Zobrist et al., 2008; Koop et al., 2011). As discussed above, we suggest that humidity-induced changes in bounced fraction of the SOA particle are related to a humidity-induced glass transition of SOA particles (Mikhailov et al., 2009).

The conditions for a humidity-induced glass transition (i.e. liquefaction) are connected to T_g (dry) of the SOA compounds at dry conditions, which is correlated to the molar mass of the compounds. Therefore, we attempt to relate the measured humidity-induced phase transitions of the SOA particles to their molar mass by showing the slope of the bounced fraction of SOA particles at $RH_I > 50\,\%$ as a function of precursor molar mass (Fig. 9). Markers are colored by the O / C ratio of the SOA. Fig. 9 shows that for SOA particles produced from isoprene, α-pinene, longifolene, and naphthalene, the "bounce slope" was correlated with the precursor molar mass. Similar trend between precursor molecular

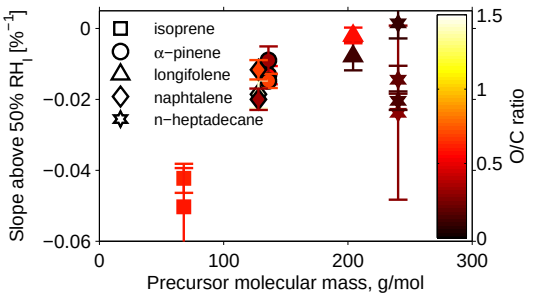

Fig. 9. The slope of the bounce at $RH_I > 50\,\%$ versus precursor molar mass for the studied systems. Error bars mark the standard error of the slope of each fit.

mass and SOA particle growth factor was also shown by Varutbangkul et al. (2006). SOA particles produced from *n*-heptadecane did not follow the same trend as the particles generated by the other precursors.

According to several studies SOA particles may contain oligomers, polymers and other high molecular weight molecules (Tolocka et al., 2004; Gao et al., 2004; Kalberer et al., 2004; Hallquist et al., 2009; Hall IV and Johnston, 2011; Kundu et al., 2012). Such oligomers and polymers are likely to affect the phase state of SOA particles. There is experimental evidence from different types of materials that oligomerisation and polymerisation do lead to an increase of the glass transition temperature of a chemical compound, and semi-empirical formulations exist (e.g., the Fox-Flory relation) that describe the molar mass dependence of T_g (Fox and Flory, 1950; Rietsch et al., 1976; Koop et al., 2011). Moreover, there is also mounting evidence that cross-linking of polymers also leads to an increase in T_g when compared to the same linear polymer, independently of whether the polymers are cross-linked in a linear or even branched fashion (Nielsen, 1969; Rietsch et al., 1976), owing to a reduced segmental motion of the individual monomeric chain units. This, oligomer and polymer formation in SOA particles will normally favor the formation of semi-solid or solid amorphous phases. It should be noted, however, that oligomeric compounds do not automatically lead to the formation of amorphous solids at room temperature. For example, in a recent study by Perraud et al. (2012) it was shown that, in contrast to α-pinene SOA, aerosolized poly(ethyleneglycol) oligomers (PEG 400, molar mass $\sim 400\,g\,mol^{-1}$, equivalent to 9 repeating units) did show liquid-like behavior in terms of their phase partitioning of oxidation products, in agreement with the fact that PEG 400 is liquid and known to be a good plasticizer for polymers. Thus the chemical nature of oligomers in SOA as well as their mass fraction in the organic phase of a particle is crucial to quantify their effect on the formation of amorphous solids. To obtain such detailed data is beyond the present study, as the HR-ToF-AMS does not retain information regarding high MW compounds and/or oligomers in the SOA due to the high degree of fragmentation of the molecular vapor via standard electron impact (Canagaratna et al., 2007), and is an interesting topic for future studies. To the extent that the "bounce slope" is proportional to the average molar mass (AMM) of the SOA, Fig. 9 suggests that the AMM of SOA generated from *n*-heptadecane does not scale with precursor AMM in the same way as the SOA in the other experiments. One possible explanation for this observation is that fragmentation reactions that cleave carbon-carbon bonds and lower the AMM are more important in SOA produced from *n*-heptadecane than in the other systems. The importance of fragmentation reactions has not been extensively characterized for precursors studied in this work. However, Chacon-Madrid et al. (2010) and Chacon-Madrid and Donahue (2011) showed that the *OH oxidation of linear aldehydes/ketones formed SOA in lower yields than linear alkanes with equivalent vapor pressures, suggesting that fragmentation is important for SOA generated from alkane precursors. If SOA generated from the other precursors experienced less fragmentation than SOA generated from *n*-heptadecane, this may explain the trends observed in Fig. 9.

4 Conclusions

Our results suggest that most types of atmospherically-relevant SOA form amorphous solid or semi-solid particles at $RH_I \lesssim 60\,\%$. These SOA particles can undergo phase transitions as a result of changes in relative humidity, and/or O / C level. Addition of hygroscopic sulphuric acid to the SOA liquefied the mixed particles at low RH_I, which is consistent with aerosol bounce observations from Virtanen et al. (2011) and T_g measurements from Koop et al. (2011). The phase of the SOA affects corresponding timescales for mass transfer and heterogeneous reactions within the particles (Cappa and Wilson, 2011; Vaden et al., 2011; Shiraiwa et al., 2011), and may influence their ability to serve as cloud condensation nuclei or ice nuclei in the atmosphere.

In most cases, humidity-induced phase changes measured for the SOA were not correlated with O / C ratio or the CCN activity, κ. However, our measurements suggest that humidity-induced phase changes were related to the average molar mass of the SOA. These observations are consistent with the results of Koop et al. (2011), who showed that T_g was more strongly influenced by molar mass than O / C ratio of model organic compounds.

With the exception of SOA produced from *n*-heptadecane, the bounced fraction of SOA particles at $RH_I < 50\,\%$ was insensitive to changes in O / C ratio. The increase in bounced fraction of *n*-heptadecane SOA particles as a function of O / C ratio is consistent with an oxidation-induced phase change from organic liquid particles to organic semi-solid particles. Future work will investigate the prevalence of oxidation-induced phase changes in other types of SOA, as

well as the ability of the bounce measurement to provide quantitative measurements of particle viscosity, diffusivity, and glass transition temperature.

Acknowledgements. This work was supported by a grant from the Nessling Foundation to the Tampere University of Technology. The research was also supported by the Office of Science (BER), Department of Energy (Atmospheric Science Program) grant No. DE-SC0006980 and the Atmospheric Chemistry Program of the National Science Foundation grants No. ATM-0525355 and ATM-0854916 to Boston College and Aerodyne Research, Inc, and the EU integrated project 505390-GOCE-CT-2004.

Edited by: B. Ervens

References

Aiken, A. C., DeCarlo, P. F., and Jimenez, J. L.: Elemental Analysis of Organic Species with Electron Ionization High-Resolution Mass Spectrometry, Anal. Chem., 79, 8350–8358, doi:10.1021/ac071150w, 2007.

Aiken, A. C., DeCarlo, P. F., Kroll, J. H., Worsnop, D. R., Huffman, J. A., Docherty, K. S., Ulbrich, I. M., Mohr, C., Kimmel, J. R., Sueper, D., Sun, Y., Zhang, Q., Trimborn, A., Northway, M., Ziemann, P. J., Canagaratna, M. R., Onasch, T. B., Alfarra, M. R., Prevot, A. S. H., Dommen, J., Duplissy, J., Metzger, A., Baltensperger, U., and Jimenez, J. L.: O / C and OM/OC Ratios of Primary, Secondary, and Ambient Organic Aerosols with High-Resolution Time-of-Flight Aerosol Mass Spectrometry, Environ. Sci. Technol., 42, 4478–4485, doi:10.1021/es703009q, 2008.

Bertram, A. K., Martin, S. T., Hanna, S. J., Smith, M. L., Bodsworth, A., Chen, Q., Kuwata, M., Liu, A., You, Y., and Zorn, S. R.: Predicting the relative humidities of liquid-liquid phase separation, efflorescence, and deliquescence of mixed particles of ammonium sulfate, organic material, and water using the organic-to-sulfate mass ratio of the particle and the oxygen-to-carbon elemental ratio of the organic component, Atmos. Chem. Phys., 11, 10995–11006, doi:10.5194/acp-11-10995-2011, 2011.

Canagaratna, M., Jayne, J., Jimenez, J., Allan, J., Alfarra, M., Zhang, Q., Onasch, T., Drewnick, F., Coe, H., Middlebrook, A., Delia, A., Williams, L., Trimborn, A., Northway, M., DeCarlo, P., Kolb, C., Davidovits, P., and Worsnop, D.: Chemical and microphysical characterization of ambient aerosols with the aerodyne aerosol mass spectrometer, Mass Spectrom. Rev., 26, 185–222, doi:10.1002/mas.20115, 2007.

Cappa, C. D. and Wilson, K. R.: Evolution of organic aerosol mass spectra upon heating: implications for OA phase and partitioning behavior, Atmos. Chem. Phys., 11, 1895–1911, doi:10.5194/acp-11-1895-2011, 2011.

Chacon-Madrid, H. J. and Donahue, N. M.: Fragmentation vs. functionalization: chemical aging and organic aerosol formation, Atmos. Chem. Phys., 11, 10553–10563, doi:10.5194/acp-11-10553-2011, 2011.

Chacon-Madrid, H. J., Presto, A. A., and Donahue, N. M.: Functionalization vs. fragmentation: n-aldehyde oxidation mechanisms and secondary organic aerosol formation, Phys. Chem. Chem. Phys., 12, 13975–13982, doi:10.1039/C0CP00200C, 2010.

Chhabra, P. S., Flagan, R. C., and Seinfeld, J. H.: Elemental analysis of chamber organic aerosol using an aerodyne high-resolution aerosol mass spectrometer, Atmos. Chem. Phys., 10, 4111–4131, doi:10.5194/acp-10-4111-2010, 2010.

Ciobanu, V. G., Marcolli, C., Krieger, U. K., Weers, U., and Peter, T.: Liquid-Liquid Phase Separation in Mixed Organic/Inorganic Aerosol Particles, J. Phys. Chem. A, 113, 10966–10978, doi:10.1021/jp905054d, 2009.

DeCarlo, P., Kimmel, J., Trimborn, A., Northway, M., Jayne, J., Aiken, A., Gonin, M., Fuhrer, K., Horvath, T., Docherty, K., Worsnop, D. R., and Jimenez, J. L.: Field-deployable, high-resolution, time-of-flight aerosol mass spectrometer, Anal. Chem., 78, 8281–8289, 2006.

Donahue, N. M., Kroll, J. H., Pandis, S. N., and Robinson, A. L.: A two-dimensional volatility basis set – Part 2: Diagnostics of organic-aerosol evolution, Atmos. Chem. Phys., 12, 615–634, doi:10.5194/acp-12-615-2012, 2012.

Fox, T. and Flory, P.: Second-order transition temperatures and related properties of polystyrene. I. Influence of molecular weight, J. Appl. Phys., 21, 581–591, 1950.

Gao, S., Keywood, M., Ng, N. L., Surratt, J., Varutbangkul, V., Bahreini, R., Flagan, R. C., and Seinfeld, J. H.: Low-Molecular-Weight and Oligomeric Components in Secondary Organic Aerosol from the Ozonolysis of Cycloalkenes and α-Pinene, J. Phys. Chem. A, 108, 10147–10164, doi:10.1021/jp047466e, 2004.

Hall IV, W. and Johnston, M.: Oligomer content of α-pinene secondary organic aerosol, Aerosol Sci. Technol., 45, 37–45, 2011.

Hallquist, M., Wenger, J. C., Baltensperger, U., Rudich, Y., Simpson, D., Claeys, M., Dommen, J., Donahue, N. M., George, C., Goldstein, A. H., Hamilton, J. F., Herrmann, H., Hoffmann, T., Iinuma, Y., Jang, M., Jenkin, M. E., Jimenez, J. L., Kiendler-Scharr, A., Maenhaut, W., McFiggans, G., Mentel, Th. F., Monod, A., Prévôt, A. S. H., Seinfeld, J. H., Surratt, J. D., Szmigielski, R., and Wildt, J.: The formation, properties and impact of secondary organic aerosol: current and emerging issues, Atmos. Chem. Phys., 9, 5155–5236, doi:10.5194/acp-9-5155-2009, 2009.

Höhne, G., Hemminger, W., and Flammersheim, H.: Differential scanning calorimetry, Springer Verlag, 2003.

IPCC: Changes in Atmospheric Constituents and in Radiative Forcing. In: Climate Change 2007: The Physical Science Basis. Contribution of Working Group I to the Fourth Assessment Report of the Intergovernmental Panel on Climate Change, available at: http://www.ipcc.ch/ipccreports/ar4-wg1.htm, 2007.

Jimenez, J. L., Canagaratna, M. R., Donahue, N. M., Prevot, A. S. H., Zhang, Q., Kroll, J. H., DeCarlo, P. F., Allan, J. D., Coe, H., Ng, N. L., Aiken, A. C., Docherty, K. S., Ulbrich, I. M., Grieshop, A. P., Robinson, A. L., Duplissy, J., Smith, J. D., Wilson, K. R., Lanz, V. A., Hueglin, C., Sun, Y. L., Tian, J., Laaksonen, A., Raatikainen, T., Rautiainen, J., Vaattovaara, P., Ehn, M., Kulmala, M., Tomlinson, J. M., Collins, D. R., Cubison, M. J., E., Dunlea, J., Huffman, J. A., Onasch, T. B., Alfarra, M. R., Williams, P. I., Bower, K., Kondo, Y., Schneider, J., Drewnick, F., Borrmann, S., Weimer, S., Demerjian, K., Salcedo, D., Cottrell, L., Griffin, R., Takami, A., Miyoshi, T., Hatakeyama, S., Shimono, A., Sun, J. Y., Zhang, Y. M., Dzepina, K., Kimmel, J. R., Sueper, D., Jayne, J. T., Herndon, S. C., Trimborn, A. M., Williams, L. R., Wood, E. C., Middlebrook, A. M., Kolb,

C. E., Baltensperger, U., and Worsnop, D. R.: Evolution of Organic Aerosols in the Atmosphere, Science, 326, 1525–1529, doi:10.1126/science.1180353, 2009.

Kalberer, M., Paulsen, D., Sax, M., Steinbacher, M., Dommen, J., Prevot, A. S. H., Fisseha, R., Weingartner, E., Frankevich, V., Zenobi, R., and Baltensperger, U.: Identification of Polymers as Major Components of Atmospheric Organic Aerosols, Science, 303, 1659–1662, doi:10.1126/science.1092185, 2004.

Kanakidou, M., Seinfeld, J. H., Pandis, S. N., Barnes, I., Dentener, F. J., Facchini, M. C., Van Dingenen, R., Ervens, B., Nenes, A., Nielsen, C. J., Swietlicki, E., Putaud, J. P., Balkanski, Y., Fuzzi, S., Horth, J., Moortgat, G. K., Winterhalter, R., Myhre, C. E. L., Tsigaridis, K., Vignati, E., Stephanou, E. G., and Wilson, J.: Organic aerosol and global climate modelling: a review, Atmos. Chem. Phys., 5, 1053–1123, doi:10.5194/acp-5-1053-2005, 2005.

Kim, Y. P., Pun, B. K.-L., Chan, C. K., Flagan, R. C., and Seinfeld, J. H.: Determination of Water Activity in Ammonium Sulfate and Sulfuric Acid Mixtures Using Levitated Single Particles, Aerosol Sci. Technol., 20, 275–284, doi:10.1080/02786829408959683, 1994.

Kirkby, J., Curtius, J., Almeida, J., Dunne, E., Duplissy, J., Ehrhart, S., Franchin, A., Gagné, S., Ickes, L., Kürten, A., Kupc, A., Metzger, A., Riccobono, F., Rondo, L., Schobesberger, S., Tsagkogeorgas, G., Wimmer, D., Amorim, A., F, B., Breitenlechner, M., David, A., Dommen, J., Downard, A., Ehn, M., Flagan, R., Haider, S., Hansel, A., Hauser, D., Jud, W., Junninen, H., Kreissl, F., Kvashin, A., A., L., Lehtipalo, K., Lima, J., Lovejoy, E., Makhmutov, F., Mathot, S., Mikkilä, J., Minginette, P., Mogo, S., Nieminen, T., Onnela, A., Pereira, P., Petäjä, T., Schnitzhofer, R., Seinfeld, S. P., Sipilä, M., Stozhkov, Y., Stratmann, F., Tome, A., Vanhanen, J., Viisanen, Y., Vrtala, A., Wagner, P., Walther, H., Weingartner, E., Wex, H., Winkler, P., Carslaw, K., Worsnop, D., Baltensberger, U., and Kulmala, M.: Role of sulphuric acid, ammonia and galactic cosmic rays in atmospheric aerosol nucleation, Nature, 476, 429–433, 2011.

Koop, T., Bookhold, J., Shiraiwa, M., and Pöschl, U.: Glass transition and phase state of organic compounds: dependency on molecular properties and implications for secondary organic aerosols in the atmosphere, Phys. Chem. Chem. Phys., 13, 19238–19255, doi:10.1039/C1CP22617G, 2011.

Krieger, U. K., Marcolli, C., and Reid, J. P.: Exploring the complexity of aerosol particle properties and processes using single particle techniques, Chem. Soc. Rev., p. Advance article, doi:10.1039/C2CS35082C, 2012.

Kundu, S., Fisseha, R., Putman, A. L., Rahn, T. A., and Mazzoleni, L. R.: High molecular weight SOA formation during limonene ozonolysis: insights from ultrahigh-resolution FT-ICR mass spectrometry characterization, Atmos. Chem. Phys., 12, 5523–5536, doi:10.5194/acp-12-5523-2012, 2012.

Lambe, A. T., Ahern, A. T., Williams, L. R., Slowik, J. G., Wong, J. P. S., Abbatt, J. P. D., Brune, W. H., Ng, N. L., Wright, J. P., Croasdale, D. R., Worsnop, D. R., Davidovits, P., and Onasch, T. B.: Characterization of aerosol photooxidation flow reactors: heterogeneous oxidation, secondary organic aerosol formation and cloud condensation nuclei activity measurements, Atmos. Meas. Tech., 4, 445–461, doi:10.5194/amt-4-445-2011, 2011a.

Lambe, A. T., Onasch, T. B., Massoli, P., Croasdale, D. R., Wright, J. P., Ahern, A. T., Williams, L. R., Worsnop, D. R., Brune, W. H., and Davidovits, P.: Laboratory studies of the chemical composition and cloud condensation nuclei (CCN) activity of secondary organic aerosol (SOA) and oxidized primary organic aerosol (OPOA), Atmos. Chem. Phys., 11, 8913–8928, doi:10.5194/acp-11-8913-2011, 2011b.

Lambe, A. T., Onasch, T. B., Croasdale, D. R., Wright, J. P., Martin, A. T., Franklin, J. P., Massoli, P., Kroll, J. H., Canagaratna, M. R., Brune, W. H., Worsnop, D. R., and Davidovits, P.: Transitions from Functionalization to Fragmentation Reactions of Laboratory Secondary Organic Aerosol (SOA) Generated from the OH Oxidation of Alkane Precursors, Environ. Sci. Technol., 46, 5430–5437, doi:10.1021/es300274t, 2012.

Lance, S., Nenes, A., Medina, J., and Smith, J. N.: Mapping the Operation of the DMT Continuous Flow CCN Counter, Aerosol Science and Technology, 40, 242–254, doi:10.1080/02786820500543290, 2006.

Mao, J., Ren, X., Brune, W. H., Olson, J. R., Crawford, J. H., Fried, A., Huey, L. G., Cohen, R. C., Heikes, B., Singh, H. B., Blake, D. R., Sachse, G. W., Diskin, G. S., Hall, S. R., and Shetter, R. E.: Airborne measurement of OH reactivity during INTEX-B, Atmos. Chem. Phys., 9, 163–173, doi:10.5194/acp-9-163-2009, 2009.

Marcolli, C. and Krieger, U.: Phase changes during hygroscopic cycles of mixed organic/inorganic model systems of tropospheric aerosols, J. Phys. Chem. A, 110, 1881–1893, 2006.

Massoli, P., Lambe, A., Ahern, A., Williams, L., Ehn, M., Mikkilä, J., Canagaratna, M., Brune, W., Onasch, T., Jayne, J., Petäjä, T., Kulmala, M., A., L., Kolb, C. E., Davidovits, P., and Worsnop, D.: Relationship between aerosol oxidation level and hygroscopic properties of laboratory generated secondary organic aerosol (SOA) particles, Geophys. Res. Lett, 37, L24801, doi:10.1029/2010GL045258, 2010.

Mikhailov, E., Vlasenko, S., Martin, S. T., Koop, T., and Pöschl, U.: Amorphous and crystalline aerosol particles interacting with water vapor: conceptual framework and experimental evidence for restructuring, phase transitions and kinetic limitations, Atmos. Chem. Phys., 9, 9491–9522, doi:10.5194/acp-9-9491-2009, 2009.

Murray, B., Wilson, T., Dobbie, S., Cui, Z., Al-Jumur, S., Möhler, O., Schnaiter, M., Wagner, R., Benz, S., Niemand, M., et al.: Heterogeneous nucleation of ice particles on glassy aerosols under cirrus conditions, Nature Geosci., 3, 233–237, 2010.

Murray, B. J.: Inhibition of ice crystallisation in highly viscous aqueous organic acid droplets, Atmos. Chem. Phys., 8, 5423–5433, doi:10.5194/acp-8-5423-2008, 2008.

Ng, N. L., Canagaratna, M. R., Zhang, Q., Jimenez, J. L., Tian, J., Ulbrich, I. M., Kroll, J. H., Docherty, K. S., Chhabra, P. S., Bahreini, R., Murphy, S. M., Seinfeld, J. H., Hildebrandt, L., Donahue, N. M., DeCarlo, P. F., Lanz, V. A., Prévôt, A. S. H., Dinar, E., Rudich, Y., and Worsnop, D. R.: Organic aerosol components observed in Northern Hemispheric datasets from Aerosol Mass Spectrometry, Atmos. Chem. Phys., 10, 4625–4641, doi:10.5194/acp-10-4625-2010, 2010.

Nielsen, L. E.: Cross-Linking-Effect on Physical Properties of Polymers, Journal of Macromolecular Science, Part C: Polymer Reviews, 3, 69–103, doi:10.1080/15583726908545897, 1969.

Pankow, J.: An absorption model of the gas/aerosol partitioning involved in the formation of secondary organic aerosol, Atmos. Environ., 28, 189–193, doi:10.1016/1352-2310(94)90094-9, 1994.

Pedernera, D. A.: Glass formation in upper tropospheric aerosol particles, Ph.D. thesis, Bielefeld University, http://pub.uni-bielefeld.de/publication/2303351, 2008 (in German).

Perraud, V., Bruns, E. A., Ezell, M. J., Johnson, S. N., Yu, Y., Alexander, M. L., Zelenyuk, A., Imre, D., Chang, W. L., Dabdub, D., Pankow, J. F., and Finlayson-Pitts, B. J.: Nonequilibrium atmospheric secondary organic aerosol formation and growth, P. Natl. Acad. Sci., 109, 2836–2841, doi:10.1073/pnas.1119909109, 2012.

Petters, M. D. and Kreidenweis, S. M.: A single parameter representation of hygroscopic growth and cloud condensation nucleus activity, Atmos. Chem. Phys., 7, 1961–1971, doi:10.5194/acp-7-1961-2007, 2007.

Pfrang, C., Shiraiwa, M., and Pöschl, U.: Chemical ageing and transformation of diffusivity in semi-solid multi-component organic aerosol particles, Atmos. Chem. Phys., 11, 7343–7354, doi:10.5194/acp-11-7343-2011, 2011.

Prenni, A., Petters, M., Kreidenweis, S., DeMott, P., and Ziemann, P.: Cloud droplet activation of secondary organic aerosol, J. Geophys. Res., 112, D10223, doi:10.1029/2006JD007963, 2007.

Renbaum, L. H. and Smith, G. D.: Artifacts in measuring aerosol uptake kinetics: the roles of time, concentration and adsorption, Atmos. Chem. Phys., 11, 6881–6893, doi:10.5194/acp-11-6881-2011, 2011.

Rietsch, F., Daveloose, D., and Froelich, D.: Glass transition temperature of ideal polymeric networks, Polymer, 17, 859–863, doi:10.1016/0032-3861(76)90251-2, 1976.

Roberts, G. and Nenes, A.: A continuous-flow streamwise thermal-gradient CCN chamber for atmospheric measurements, Aerosol Sci. Technol., 39, 206–221, 2005.

Saukko, E., Kuuluvainen, H., and Virtanen, A.: A method to resolve the phase state of aerosol particles, Atmos. Meas. Tech., 5, 259–265, doi:10.5194/amt-5-259-2012, 2012.

Seinfeld, J. and Pandis, S.: Atmospheric chemistry and physics: from air pollution to climate change, Wiley New York, 2nd edn., 1998.

Shiraiwa, M., Ammann, M., Koop, T., and Pöschl, U.: Gas uptake and chemical aging of semisolid organic aerosol particles, Proceedings of the National Academy of Sciences, 108, 11003–11008, doi:10.1073/pnas.1103045108, 2011.

Sipilä, M., Berndt, T., Petäjä, T., Brus, D., Vanhanen, J., Stratmann, F., Patokoski, J., Mauldin, R. L., Hyvärinen, A.-P., Lihavainen, H., and Kulmala, M.: The Role of Sulfuric Acid in Atmospheric Nucleation, Science, 327, 1243–1246, doi:10.1126/science.1180315, 2010.

Song, M., Marcolli, C., Krieger, U. K., Zuend, A., and Peter, T.: Liquid-liquid phase separation and morphology of internally mixed dicarboxylic acids/ammonium sulfate/water particles, Atmos. Chem. Phys., 12, 2691–2712, doi:10.5194/acp-12-2691-2012, 2012.

Tolocka, M. P., Jang, M., Ginter, J. M., Cox, F. J., Kamens, R. M., and Johnston, M. V.: Formation of Oligomers in Secondary Organic Aerosol, Environ. Sci. Technol., 38, 1428–1434, doi:10.1021/es035030r, 2004.

Vaden, T. D., Imre, D., Beránek, J., Shrivastava, M., and Zelenyuk, A.: Evaporation kinetics and phase of laboratory and ambient secondary organic aerosol, P. Natl. Acad. Sci., 108, 2190–2195, doi:10.1073/pnas.1013391108, 2011.

Varutbangkul, V., Brechtel, F. J., Bahreini, R., Ng, N. L., Keywood, M. D., Kroll, J. H., Flagan, R. C., Seinfeld, J. H., Lee, A., and Goldstein, A. H.: Hygroscopicity of secondary organic aerosols formed by oxidation of cycloalkenes, monoterpenes, sesquiterpenes, and related compounds, Atmos. Chem. Phys., 6, 2367–2388, doi:10.5194/acp-6-2367-2006, 2006.

Virtanen, A., Joutsensaari, J., Koop, T., Kannosto, J., Yli-Pirilä, P., Leskinen, J., Mäkelä, J., Holopainen, J., Pöschl, U., Kulmala, M., Worsnop, D. R., and Laaksonen, A.: An amorphous solid state of biogenic secondary organic aerosol particles, Nature, 467, 824–827, 2010.

Virtanen, A., Kannosto, J., Kuuluvainen, H., Arffman, A., Joutsensaari, J., Saukko, E., Hao, L., Yli-Pirilä, P., Tiitta, P., Holopainen, J. K., Keskinen, J., Worsnop, D. R., Smith, J. N., and Laaksonen, A.: Bounce behavior of freshly nucleated biogenic secondary organic aerosol particles, Atmos. Chem. Phys., 11, 8759–8766, doi:10.5194/acp-11-8759-2011, 2011.

Zahardis, J. and Petrucci, G. A.: The oleic acid-ozone heterogeneous reaction system: products, kinetics, secondary chemistry, and atmospheric implications of a model system – a review, Atmos. Chem. Phys., 7, 1237–1274, doi:10.5194/acp-7-1237-2007, 2007.

Ziemann, P.: Atmospheric Chemistry: Phase matters for aerosols, Nature, 467, 797–798, 2010.

Zobrist, B., Marcolli, C., Pedernera, D. A., and Koop, T.: Do atmospheric aerosols form glasses?, Atmos. Chem. Phys., 8, 5221–5244, doi:10.5194/acp-8-5221-2008, 2008.

Zobrist, B., Soonsin, V., Luo, B. P., Krieger, U. K., Marcolli, C., Peter, T., and Koop, T.: Ultra-slow water diffusion in aqueous sucrose glasses, Phys. Chem. Chem. Phys., 13, 3514–3526, doi:10.1039/C0CP01273D, 2011.

Zuend, A. and Seinfeld, J. H.: Modeling the gas-particle partitioning of secondary organic aerosol: the importance of liquid-liquid phase separation, Atmos. Chem. Phys., 12, 3857–3882, doi:10.5194/acp-12-3857-2012, 2012.

Publication V

E Saukko, S Zorn, M Kuwata, J Keskinen, A Virtanen Phase state and deliquescence hysteresis of ammonium sulfate seeded secondary organic aerosol *Aerosol Science and Technology*, 49:531−-537, 2015.

Aerosol Science and Technology, 49:531–537, 2015

ISSN: 0278-6826 print / 1521-7388 online
DOI: 10.1080/02786826.2015.1050085

Phase State and Deliquescence Hysteresis of Ammonium-Sulfate-Seeded Secondary Organic Aerosol

Erkka Saukko,[1] Soeren Zorn,[2] Mikinori Kuwata,[3] Jorma Keskinen,[1] and Annele Virtanen[4]
[1]*Department of Physics, Tampere University of Technology, Tampere, Finland*
[2]*AeroMegt GmbH, Solingen, Germany*
[3]*Earth Observatory of Singapore, Nanyang Technological University, Singapore*
[4]*Department of Applied Physics, University of Eastern Finland, Kuopio, Finland*

The phase state of secondary organic aerosol (SOA) has an impact on its lifetime, composition, and its interaction with water. To better understand the effect of phase state of SOA on climate interactions, we studied the SOA phase state and the effect of its history and report here the phase state and the humidity-induced phase hysteresis of multicomponent-seeded SOA particles produced in a large, continuously stirred tank reactor. We determined the phase state of the particles by their bounced fraction impacting on a smooth substrate in a low-pressure impactor. The particles were composed of ammonium sulfate ($[NH_4]_2SO_4$) seed and a secondary organic matter (SOM) shell formed from oxidized α-pinene or isoprene. The ammonium sulfate (AS) seed dominated the deliquescence of the α-pinene SOM multicomponent particles, whereas their efflorescence was strongly attenuated by the SOM coating. Particles coated with isoprene SOM showed continuous phase transitions with a lesser effect by the AS seed. The results agree with and independently corroborate contemporary research.

1. INTRODUCTION

The effect of aerosols on climate and their associated health issues are of local and global interest. Secondary organic aerosol (SOA) can contribute as much as 50% to the non-refractory submicron aerosol mass in the atmosphere (Jimenez et al. 2009). The cloud condensation nucleus (CCN) properties of SOA are crucial for the total radiative forcing effect of aerosol. Factors affecting the probability of particles participating in cloud formation are the hygroscopicity of the material and the size and lifetime of the particulate matter. The phase of the particles may greatly affect the atmospheric lifetime of SOA; variation in ambient humidity can change the viscosity of the particulate matter by several orders of magnitude and accordingly change the atmospheric chemical lifetime by more than an order of magnitude (Shiraiwa et al. 2011).

Solid-phase SOA was first observed at a boreal forest measurement station and in a controlled laboratory smog chamber study on SOA produced from α-pinene and pine emitted precursors via ozonolysis (Virtanen et al. 2010, 2011). The observation constrained the upper relative humidity (RH) limit of the solid phase to be above 20% RH. The observation of solid phase was extended from α-pinene SOA to SOA produced from other common biogenic precursors (Saukko et al. 2012b), and experiments with three different biogenic precursors produced particles with a solid or semi-solid phase even at 60% RH or higher. Cappa and Wilson (2011) and Perraud et al. (2012) studied the non-equilibrium nature of the interaction between the gaseous and condensed phases of SOA, emphasizing the importance of the phase state for the chemistry of the condensed phase of SOA. Studying further the evaporation kinetics of SOA, Vaden et al. (2011) concluded that the transport from condensed phase to gas phase is two orders of magnitude slower than that expected with fast equilibrium evaporation models. They showed with direct evaporation aging experiments that the flux of material from the condensed part of SOA is constrained by a low diffusion constant for the bulk of the particulate matter. A further study with a multicomponent system showed that SOM from two different precursors forms at least partial shell structures. Different shell orders exhibited different evaporation behavior, implying that at least one component had a semi-solid phase (Loza et al. 2013).

Bones et al. (2012) studied the uptake into and release of water from organic material and concluded that uptake is limited by the diffusion of dissolving SOA material in the aqueous surface layer. However, evaporation is limited by the diffusion of water through a solid SOA layer. Another effect was discovered by Kidd et al. (2014), who reported that RH during SOA formation also affects the phase state of the SOA produced.

A further complication arises from the multicomponent nature of seeded SOA particles. If SOA particles are formed

Received 14 February 2015; accepted 4 May 2015.
Address correspondence to Erkka Saukko, Department of Physics, Tampere University of Technology, P.O. Box 589, Tampere 33101, Finland. E-mail: erkka.saukko@tut.fi

through condensation on a seed such as ammonium sulfate (AS), the different particle components may have different water affinities. This affects cloud processing and further changes the morphology en route to cloud droplet formation. This is observed in different hysteresis phenomena in the wetting behavior of the particles (Smith et al. 2012, 2013). The differences in the components of secondary organic material give rise also to an additional type of phase change, phase separation of the liquid phases. Liquid–liquid phase separation (LLPS) can be parameterized for the organic-to-sulfate ratio of SOA and the oxygen-to-carbon (O/C) ratio (Bertram et al. 2011 and further elaborated by Song et al. 2012), as recently reviewed by You et al. (2014).

The evolution of SOM in the atmosphere is a complex phenomenon, and research is now seeking to constrain the parameters that describe the formation, processing, and removal of SOA in the atmosphere. These parameters are crucial for global assessment of the effect of SOA on the climate.

We report the phase of ammonium-sulfate-seeded SOA produced in a continually stirred reaction chamber and the related phase hysteresis to humidity-induced phase transitions for particle sizes in the range of 115 to 145 nm. The SOM coating AS seeds was produced by oxidizing α-pinene and isoprene precursors in a continuously mixed chamber reactor. The seed greatly affects the bounce behavior of particles when SOM is solid, even at relatively high relative humidities. Deliquescence hysteresis, LLPS, and mixing effects affect the water uptake and chemical reactivity of the particles.

2. METHODS AND MATERIALS

The aerosol particles for the experiments were produced in the Harvard Environmental Chamber (HEC; Shilling et al. 2008; King et al. 2009). The system uses a 5-m^3, continuously stirred Teflon bag with UVC lamps in a thermally controlled enclosure. Some important inputs to the chamber include a seed injection system (Collison atomizer, silica gel drier, and a TSI nanoDMA, TSI Inc., Shoreview, MN, USA) and a system for injecting volatile organic compounds (VOC). In the case of isoprene, VOC comes from a gas cylinder and in the case of α-pinene from a syringe pump whose effluent passes through a heated glass bulb. The humidity in the HEC is controlled with a prehumidified airflow of 20 L/min.

An O_3 generator housing a UV lamp was used to produce ozone, which was added to a separate input air flow. With dark ozonolysis oxidation experiments, the chamber UV lights were off, ozone remaining thus the main oxidizing agent. The UVC lamps inside the HEC where used to dissociate injected H_2O_2 to produce a hydroxyl radical (*OH) for photo-oxidation experiments. All injected air flows came from a zero-air generator.

The AS seed particles used for SOM condensation were dried and size-selected with a Vienna type differential mobility analyzer (DMA) to produce a known seed aerosol size distribution with a median diameter of 70 nm (and accompanying doubly charged particles of 103 nm and negligible triply and further charged particles of 130 nm and larger). In the reaction chamber, the oxidized precursor was condensed onto the seed particles, resulting in a size distribution characteristic of a continuous reactor (Kuwata and Martin 2012). After a period of about 12 h to allow the smog chamber and aerosol production to stabilize, measurements were started. The aerosol was sampled continuously via a sampling manifold for transfer to the various instruments.

The multicomponent composition of the particles, the RH cycling, and the low-pressure impactor system used for bounced fraction measurements added some complexity to interpreting the results. The differences in the hystereses of the substances had to be taken into account when relevant RH was determined. The humidity history of the particles in the measurement system and its effects on interpreting the results are discussed in Section 2.2.

2.1. Aerosol Size, Mass, and Composition

An aerodyne high resolution time of flight aerosol mass spectrometer (HR-ToF AMS, Aerodyne Research Inc., Billerica, MA, USA) was used to monitor chemical composition and particle mass size distribution. The particle size distribution was measured with a TSI scanning mobility particle sizer (SMPS, TSI Inc., Shoreview, MN, USA).

2.2. SOA Particle Phase Measurement

The phase state of the particles was measured using a single stage low-pressure impactor and a TSI ultrafine water condensation particle counter (UWCPC, TSI Inc.; method described in detail in Saukko et al. 2012a). The particles were size-selected with a Vienna type DMA, and the sizes studied in the experiments described below were between 115 nm and 145 nm for particles grown on 70-nm singly charged seed particles.

In the deliquescence branch, particles were humidified with a Nafion dryer to an RH of 20 to 90% RH and equilibrated for 3 s in a residence time tube. This RH is defined as the Humidifier RH. The aerosol was brought to the impactor pressure (69 kPa) with a needle valve and a pinhole. A pressure drop reduced the RH proportionally to the pressure. The particles had about 0.9 s for equilibration at this lower humidity before they impacted on a polished steel plate (Saukko et al. 2012a). The bounced fraction was calculated by comparing the inlet concentration measured with the UWCPC before the impactor to that after the impactor. After traveling through the impactor, the sample passed into a separate sampling chamber where it was kept at 38.7 kPa until the system stabilized. After stabilization, the sample flow was cut, and clean air was used to bring the sample to ambient pressure and subsequent measurement with a CPC.

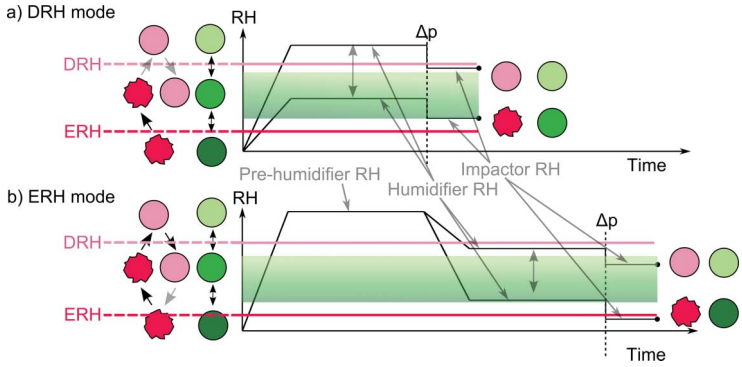

FIG. 1. Schematic of the humidity cycles of bounce hysteresis measurements. The left panel shows the differences in RH cycling of amorphous (green) and crystalline salt (pink) particles. The corresponding phase transition limits are shown in lines for crystalline particles. Likewise, a continuous deliquescence band for amorphous particles is shown in green. The dashed line stands for a pressure and corresponding humidity drop at the impactor entrance. Because of differences in particle hysteresis behavior, the final phase state depends on particles' RH history.

In the efflorescence branch, an additional prehumidifier at 90% RH and with a 3-s laminar flow residence time tube was added before the adjustable humidifier, which in this case was used as a drier. The humidity processes for hydration (DRH) and the efflorescence (ERH) branches are schematized in Figure 1.

Determining the deliquescence relative humidity (DRH) with the impaction method depends on the maximum RH and the subsequent minimum RH that the particle experiences during the cycle. If the seeds have been humidified to above the DRH, they remain liquid even if the humidity in the impactor drops as long as the impactor RH remains above the

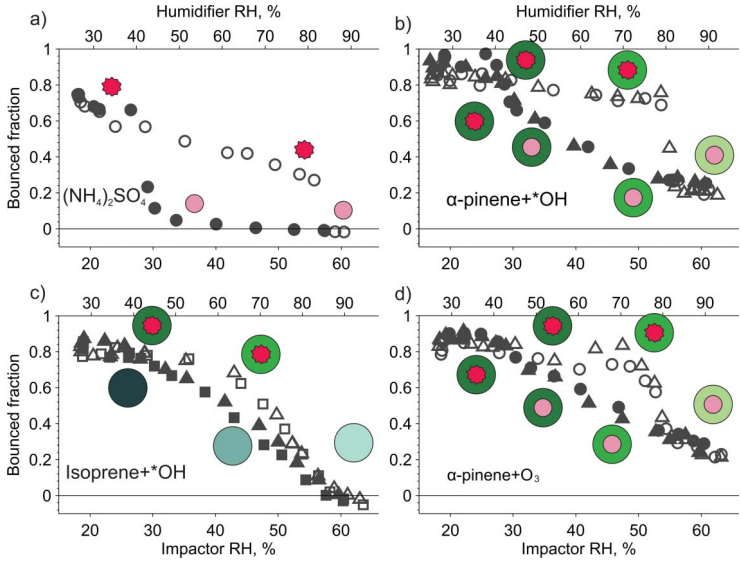

FIG. 2. Bounce hysteresis results for (a) pure ammonium sulfate particles, (b) AS seed coated with photo-oxidized α-pinene SOM, (c) AS seed coated with photo-oxidized isoprene SOM, and (d) AS seed coated with α-pinene SOM produced via dark ozonolysis. Suggested particle morphologies are represented as drawings close to data points. The green part in the drawing is SOM and the red the AS core. Green becoming lighter denotes decreasing viscosity for both SOM and mixed cases. With AS, light color denotes the deliquesced phase. For the data points, open symbols denote the hydration cycle of the experiment, whereas closed symbols denote the hydration-dehydration cycle. Ideal particle core-shell morphology is not confirmed but assumed for the illustration.

efflorescence relative humidity (ERH). Based on this phase hysteresis, the relevant humidity for DRH measurements of crystalline particles is the Humidifier RH. Hysteretic behavior is very typical of pure crystalline compounds.

With crystalline compounds, the DRH can be determined even if the impactor humidity is lower than the DRH, as can be seen in the bounced fraction of pure AS particles shown in Figure 2a. The continuous decrease in the bounced fraction with an increasing RH is linked to water adsorption onto the particles (Romakkaniemi et al. 2001; Biskos et al. 2006; Mikhailov et al. 2009; Saukko et al. 2012a). The SOM coating attenuates this trend markedly, as further discussed below in Section 3. This behavior agrees with Bateman et al. (2014), who studied computationally and experimentally the bounce of particles in an impactor and confirmed a decreasing bounce of AS upon a high RH. The decreasing bounce resulted from an increasing capillary force due to increased water between particles and the impaction substrate.

A SOM coating, however, consists of a mixture of numerous compounds (Hallquist et al. 2009) likely to have high molar masses. These compounds and especially their mixtures are typically amorphous and not expected to exhibit clear deliquescence and efflorescence steps or hysteresis (excluding kinetic effects) in their phase changes (Mikhailov et al. 2009; Koop et al. 2011; Zobrist et al. 2011). Thus the relevant RH defining the phase at the moment of impaction for SOM-coated particles is the reduced RH, referred to as the Impactor RH. The behavior of pure crystalline and single component amorphous particles in bounce measurements is described in detail in Saukko et al. (2012a).

The bounce probability of a particle is mainly affected by change in viscosity, elasticity, and adhesion to the substrate, impactor pressure and flow being constant. Viscosity is inversely related to bounce, since low viscosity in the highly dynamic situation of a particle impact means better conservation of kinetic energy. Renbaum-Wolff et al. (2013) studied the viscosity of α-pinene SOM with a mechanical poke-flow technique and derived a lower limit of 378 Pa·s and an upper limit of 9.92×10^4 to 4.53×10^7 Pa·s while altering RH from 70 to 40% RH. A corresponding method of particle coalescence gave an estimate for SOA viscosity derived from Scots pine -VOC (a terpene mixture mostly comprising α-pinene, β-pinene, Myrcene, β-phellandrene, limonene, and Δ^3-carene) and an SO_2 of approximately 10^{12} Pa·s (Hao et al. 2009; Pajunoja et al. 2014).

When the bounced fraction is high, particles are considered solid or semi-solid (for example, dry AS shows a bounced fraction of 0.78). When particles do not bounce, they are considered liquid-like. The intermediate bounced fraction values of 0 and 0.78 represent a gradual change in the mechanical properties, such as viscosity, adhesion, and elastic modulus, of particulate matter.

Seeds and final coated particles are of sufficiently large size to contain a significant fraction of doubly charged particles after diffusion charging in size-selection processes. Appropriate corrections to the impaction efficiency in the impactor must be taken into account by correcting for particles not reaching the impactor substrate. Since the size distributions of seed particles, coated particles, and the collection efficiency curve of the impactor are known, impaction efficiency can be corrected.

3. RESULTS AND DISCUSSION

The bounced fraction of pure AS seeds is given in Figure 2a. Notable points of reference are the deliquescence and efflorescence points at 80 ± 3% Humidifier RH and 28 ± 3% Impactor RH. There is also a gradual drop in the bounced fraction with increasing humidity, as described in Section 2.2 above.

The bounce behavior of AS particles coated with SOM from *OH-oxidized α-pinene is shown in Figure 2b while the O/C ratio, shell thicknesses, and seed sizes are given in Table 1. At low humidities, the particle bounced fraction is above 0.8 and decreases gradually to 0.75 ± 0.05 until it reaches 80 ± 3% Humidifier RH. Compared to pure AS

TABLE 1
Oxygen-to-carbon (O/C) ratio and organic volume fraction for singly charged seed and total particle

Experiment	O/C ratio ± STD	Organic volume fraction (for singly charged) ± HWHM	Particles size (nm) ± HWHM/seed size (nm) ± HWHM	Coating thickness (nm) ± HWHM
α-pinene+*OH Δ	0.31 ± 0.01	0.89 ± 0.03	145 ± 15/70 ± 6	38 ± 16
α-pinene+*OH ◯	0.31 ± 0.01	0.82 ± 0.05	125 ± 13/70 ± 6	28 ± 14
α-pinene+O_3 Δ	N/A	0.82 ± 0.05	125 ± 13/70 ± 6	28 ± 14
α-pinene+O_3 ◯	0.33 ± 0.01	0.86 ± 0.04	135 ± 14/70 ± 6	33 ± 15
Isoprene+*OH □	0.70 ± 0.01	0.82 ± 0.05	125 ± 13/70 ± 6	28 ± 14
Isoprene+*OH Δ	0.71 ± 0.01	0.77 ± 0.06	115 ± 12/70 ± 6	22 ± 13

The error in O/C was estimated from the standard deviation of the value during the measurement. The error for the primary particle size is the half width at half maximum (HWHM) of the singly charged seed size distribution and the differential mobility analyzer (DMA) transfer function of the SOA selection, respectively. The error for coating thickness is estimated as the geometric sum of the seed and total particle size errors, and the error for the organic volume fraction is calculated as the standard error calculated from the seed and coated particle sizes and respective errors.

particles, adding a SOM layer attenuates the slow decrease in bounce. For SOM-coated AS particles, the decrease is smaller. Bateman et al. (2014) explain this as being due to different surface energy and thus different capillary adhesion forces induced between impaction plate and particles. This humidity-dependent bounce behavior of pure α-pinene SOM coating agrees with previous measurements of α-pinene SOA particles (Saukko et al. 2012b).

The bounced fraction drops steeply at 80 $\pm$ 3% RH, as observed at the DRH of AS in a growth factor hysteresis study, for example, by Mikhailov et al. (2009). The SOA was produced at rather large organic volume fractions of 0.82 and 0.89 (for singly charged seeds), corresponding to spherical shell coating thicknesses of 23.5 and 32.5 nm, respectively. At 80 $\pm$ 3% RH, the bounced fraction did not drop all the way to zero but remained at about 0.2 $\pm$ 0.05 even at the highest RH obtainable in the system. Although the exact morphology of the particles cannot be determined from these experiments, this result indicates that some particles had a solid, at least partially enclosing SOM shell and that they could bounce from the impaction plate even if the AS seed was liquid. Whether the particles had an intact core-shell structure is interesting for discussion on water permeability and diffusion kinetics through the SOM layer and should be further studied. If the SOM shell was intact in these experiments, a high permeability could be expected. However, based on previous studies, a glassy state of SOM could inhibit or delay the deliquescence of the seed if the SOM shell is intact (Shiraiwa et al. 2011; Tong et al. 2011).

The dehydration branch displays an ERH step at 30 $\pm$ 3% Impactor RH, where the ERH of AS is expected. Compared to the pure AS reference in Figure 2a, however, a gradual but substantial increase occurs in the bounced fraction to between 0.6 and 0.7 with decreasing RH before the final, steeper change in efflorescence. This behavior can be explained by a phase separation of particles into an AS-rich core and a SOM-rich shell (Bertram et al. 2011). The SOM shell leads to an increased bounce upon drying even if the AS core is still a deliquesced liquid.

Different SOM shell thicknesses have only a minor effect on bounce behavior, as seen in Figure 2, where different SOM fractions are denoted by different symbols. For α-pinene experiments, the SOM shell thickness was between 27.5 and 37.5 nm, whereas the isoprene shell thicknesses were 22.5 and 27.5 nm (Table 1). Even a low-volume fraction of deliquesced AS is enough to reduce the bounce of particles at high humidities. Because SOM is expected to have a similar response in both DRH and ERH branches, any difference results from either seed behavior or mixing effects. There are indications that photo-oxidized α-pinene SOM is solid even at an Impactor RH above 50% (Saukko et al. 2012b); thus the bounce behavior effect of the seed is more likely. Separation of the two chemical phases – AS and SOM – is evident from the changes in the observable characteristic physical phase in Figure 2b at the DRH and ERH of pure AS. This agrees with the results of Bertram et al. (2011), who give an LLPS limit of 0.7 for the O/C, whereas in our experiments the O/C was 0.31 $\pm$ 0.01 (Table 1).

The bounce hysteresis of a system with similar seeds and precursor but with dark ozonolysis oxidation is shown in Figure 2d. The general features of the DRH are the same, but there is no clear evidence of efflorescence. The bounced fraction increases gradually with decreasing RH to 0.80 $\pm$ 0.05 with no step-like transitions. The prominent deliquescence behavior typical of crystalline AS indicates separate phases until DRH is reached.

The lack of a pronounced efflorescence differs from the photolysis experiment in Figure 2b. We cannot rule out that the AS seed and the SOM mixed to form a single phase, and existing studies support a case for separated phases (Anttila et al. 2007; Smith et al. 2011). Apart from a mixed seed α-pinene SOM, another explanation may be the lower water affinity of the α-pinene SOM, produced by dark ozonolysis as opposed to SOM produced by photolysis. The symbols for the efflorescence branch shown in Figure 2d indicate separate phases, which we consider more likely than a single mixed phase. This is also supported by the measured O/C ratio of 0.33 $\pm$ 0.01, which is well below the LLPS O/C threshold (Bertram et al. 2011). No O/C ratio is available for the experiment with the slightly lower organic fraction, but since the reactor ran continuously throughout the two experiments, the O/C ratio is expected to be relatively constant. Furthermore, we would like to point out that the bounce behavior of particles consisting of AS and α-pinene SOM produced by dark ozonolysis was strikingly similar to the calculated deliquescence and efflorescence behavior in a recent study by Shiraiwa et al. (2013).

Isoprene SOM lacked the characteristic deliquescence and efflorescence behavior even though some hysteresis was visible between the hydration and dehydration experiments (Figure 2c). The absence of a sharp deliquescence signal suggests that isoprene SOM takes up water gradually, as expected of a well-mixed amorphous substance. Since the DRH for $(NH_4)_2SO_4$ is 80%, isoprene SOM is likely to soften sufficiently by taking up water to stop bounce. Compared to α-pinene, the bounced fraction also drops very low, suggesting a total deliquescence of the particle. The deliquescence of isoprene at an RH lower than that of α-pinene SOM is in line with Saukko et al. (2012b). In the dehydration experiments, a similar smooth change in the bounced fraction was observed, which suggests that the two particle phases are either dominated by the low RH limits of the isoprene SOM or that they are homogeneously mixed. The latter conclusion agrees with Bertram et al. (2011), where the O/C of oxidized isoprene SOM (0.69–0.71) was at the limit of 0.7. Above this value, the phases are expected to be completely mixed even in dry conditions (Bertram et al. 2011).

The bounced fraction of isoprene SOA at 40% RH is the same or higher than the bounced fraction of α-pinene SOA, suggesting either a strong response to a change in humidity (Saukko et al. 2012b) or that the mixed system has a higher viscosity due to a reduced water uptake hysteresis than separated SOM and pure AS seed. Furthermore, recent model calculations support the finding that at the same humidity the viscosity of isoprene SOA is lower than that of α-pinene SOA (Berkemeier et al. 2014).

4. CONCLUSIONS

Bounced fraction measurements with separate deliquescence and efflorescence branches can be used to define the history of two-component particles. Our results with AS seed particles and either isoprene or α-pinene SOM have led us to the following two main conclusions.

First, as to the phase separation of AS seed and SOM material, SOM forms a semi-solid layer on top of the deliquesced seed. This leads to a clearly visible and reversible response to changes in RH. This is the case for α-pinene SOM. Our finding shows that with a phase-separated inorganic core and an organic shell, the organic shell can form a semi-solid layer on the deliquesced core. Depending on the thickness and viscosity of the layer, the semi-solid organic layer may "isolate" the deliquesced core from the surrounding molecules because with solid surfaces reactants are essentially confined to the surface, as discussed in Shiraiwa et al. (2011). Song et al. (2015) estimated the timescale of mixing for 200 nm, isoprene-derived SOM particles to be between 0.4 ms (at 85% RH) and 0.1 h (at 0% RH). For a shelled structure with a shell thickness of 30 nm, the range is comparable to conclude that the coating cannot prevent the deliquescence of the seed, but it can increase the timescale of efflorescence from that of the seed alone. This delay in response to changes in RH can prevent the particle reaching a size large enough to become a cloud droplet when a competing condensation sink for water is available.

Second, our results show that if the phases are mixed, the properties of the mixture determine the bounce behavior, and the effect of the AS seed cannot be distinguished, as corroborated by previous studies (Bertram et al. 2011; Smith et al. 2012). It should be noted that the organic fraction was high (0.77–0.82), and that the bounce behavior of isoprene SOA was comparable to that of pure isoprene SOA presented in Saukko et al. (2012b). This indicates that the viscosity of mixed particles at certain ambient RH is close to the viscosities of pure isoprene SOA particles.

The phase state of SOM depends on the state of the mixing of the particle components and on the history of the phase state. The main factor to determine the phase state of the studied particles was RH, though chemical composition and the oxidation state of the SOM have an impact as well (Bertram et al. 2011; Virtanen et al. 2011; Saukko et al. 2012b).

ACKNOWLEDGMENTS

The Environmental Chemistry group at Harvard is acknowledged for their permission to use their facilities and instrumentation. Dr. Mackenzie Smith is acknowledged for his assistance with the experiments.

FUNDING

Erkka Saukko acknowledges the support of the Maj and Tor Nessling foundation [2011323].

REFERENCES

Anttila, T., Kiendler-Scharr, A., Mentel, T. F., and Tillmann, R. (2007). Size Dependent Partitioning of Organic Material: Evidence for the Formation of Organic Coatings on Aqueous Aerosols. *J. Atmos. Chem.*, 57(3):215–237.

Bateman, A. P., Belassein, H., and Martin, S. T. (2014). Impactor Apparatus for the Study of Particle Rebound: Relative Humidity and Capillary Forces. *Aerosol Sci. Technol.*, 48(1):42–52.

Berkemeier, T., Shiraiwa, M., Pöschl, U., and Koop, T. (2014). Competition between Water Uptake and Ice Nucleation by Glassy Organic Aerosol Particles. *Atmos. Chem. Phys.,* 14(22):12513–12531.

Bertram, A., Martin, S., Hanna, S., Smith, M., Bodsworth, A., Chen, Q., et al. (2011). Predicting the Relative Humidities of Liquid-Liquid Phase Separation, Efflorescence, and Deliquescence of Mixed Particles of Ammonium Sulfate, Organic Material, and Water Using the Organic-to-Sulfate Mass Ratio of the Particle and the Oxygen-to-Carbon Elemental Ratio of the Organic Component. *Atmos. Chem. Phys.*, 11(21):10995–11006.

Biskos, G., Paulsen, D., Russell, L. M., Buseck, P. R., and Martin, S. T. (2006). Prompt Deliquescence and Efflorescence of Aerosol Nanoparticles. *Atmos. Chem. Phys.,* 6(12):4633–4642.

Bones, D. L., Reid, J. P., Lienhard, D. M., and Krieger, U. K. (2012). Comparing the Mechanism of Water Condensation and Evaporation in Glassy Aerosol. *Proc. Natl. Acad. Sci.*, 109(29):11613–11618.

Cappa, C. D., and Wilson, K. R. (2011). Evolution of Organic Aerosol Mass Spectra Upon Heating: Implications for OA Phase and Partitioning Behavior. *Atmos. Chem. Phys.*, 11(5):1895–1911.

Hallquist, M., Wenger, J. C., Baltensperger, U., Rudich, Y., Simpson, D., Claeys, M., et al. (2009). The Formation, Properties and Impact of Secondary Organic Aerosol: Current and Emerging Issues. *Atmos. Chem. Phys.*, 9(14):5155–5236.

Hao, L. Q., Yli-Pirilä, P., Tiitta, P., Romakkaniemi, S., Vaattovaara, P., Kajos, M. K., et al. (2009). New Particle Formation from the Oxidation of Direct Emissions of Pine Seedlings. *Atmos. Chem. Phys.,* 9:8121–8137.

Jimenez, J. L., Canagaratna, M. R., Donahue, N. M., Prevot, A. S. H., Zhang, Q., Kroll, J. H., et al. (2009). Evolution of Organic Aerosols in the Atmosphere. *Science*, 326(5959):1525–1529.

Kidd, C., Perraud, V., Wingen, L. M., and Finlayson-Pitts, B. J. (2014). Integrating Phase and Composition of Secondary Organic Aerosol from the Ozonolysis of α-Pinene. *Proc. Natl. Acad. Sci.*, 111(21):7552–7557.

King, S. M., Rosenoern, T., Shilling, J. E., Chen, Q., and Martin, S. T. (2009). Increased Cloud Activation Potential of Secondary Organic Aerosol for Atmospheric Mass Loadings. *Atmos. Chem. Phys.*, 9(9):2959–2971.

Koop, T., Bookhold, J., Shiraiwa, M., and Pöschl, U. (2011). Glass Transition and Phase State of Organic Compounds: Dependency on Molecular Properties and Implications for Secondary Organic Aerosols in the Atmosphere. *Phys. Chem. Chem. Phys.,* 13(43):19238–19255.

Kuwata, M., and Martin, S. T. (2012). Particle Size Distributions Following Condensational Growth in Continuous Flow Aerosol Reactors as Derived from Residence Time Distributions: Theoretical Development and Application to Secondary Organic Aerosol. *Aerosol Sci. Technol.*, 46(8): 937–949.

Loza, C. L., Coggon, M. M., Nguyen, T. B., Zuend, A., Flagan, R. C., and Seinfeld, J. H. (2013). On the Mixing and Evaporation of Secondary Organic Aerosol Components. *Env. Sci. Technol.*, 47(12):6173–6180.

Mikhailov, E., Vlasenko, S., Martin, S., Koop, T., and Pöschl, U. (2009). Amorphous and Crystalline Aerosol Particles Interacting with Water Vapor: Conceptual Framework and Experimental Evidence for Restructuring, Phase Transitions and Kinetic Limitations. *Atmos. Chem. Phys.,* 9(24):9491–9522.

Pajunoja, A., Malila, J., Hao, L., Joutsensaari, J., Lehtinen, K. E., and Virtanen, A. (2014). Estimating the Viscosity Range of SOA Particles Based on Their Coalescence Time. *Aerosol Sci. Technol.,* 48(2):i–iv.

Perraud, V., Bruns, E. A., Ezell, M. J., Johnson, S. N., Yu, Y., Alexander, M. L., et al. (2012). Nonequilibrium Atmospheric Secondary Organic Aerosol Formation and Growth. *Proc. Natl. Acad. Sci.,* 109(8):2836–2841.

Renbaum-Wolff, L., Grayson, J. W., Bateman, A. P., Kuwata, M., Sellier, M., Murray, B. J., et al. (2013). Viscosity of α-Pinene Secondary Organic Material and Implications for Particle Growth and Reactivity. *Proc. Natl. Acad. Sci.*, 110(20):8014–8019.

Romakkaniemi, S., Hämeri, K., Väkevä, M., and Laaksonen, A. (2001). Adsorption of Water on 8–15 nm NaCl and $(NH_4)_2SO_4$ Aerosols Measured Using an Ultrafine Tandem Differential Mobility Analyzer. *J. Phys. Chem. A,* 105(35):8183–8188.

Saukko, E., Kuuluvainen, H., and Virtanen, A. (2012a). A Method to Resolve the Phase State of Aerosol Particles. *Atmos. Measur. Techn.,* 5(1):259–265.

Saukko, E., Lambe, A. T., Massoli, P., Koop, T., Wright, J. P., Croasdale, D. R., et al. (2012b). Humidity-Dependent Phase State of SOA Particles from Biogenic and Anthropogenic Precursors. *Atmos. Chem. Phys.,* 12 (16):7517–7529.

Shilling, J. E., Chen, Q., King, S. M., Rosenoern, T., Kroll, J. H., Worsnop, D. R., et al. (2008). Particle Mass Yield in Secondary Organic Aerosol Formed by the Dark Ozonolysis of α-Pinene. *Atmos. Chem. Phys.,* 8 (7):2073–2088.

Shiraiwa, M., Ammann, M., Koop, T., and Pöschl, U. (2011). Gas Uptake and Chemical Aging of Semisolid Organic Aerosol Particles. *Proc. Natl. Acad. Sci.*, 108(27):11003–11008.

Shiraiwa, M., Zuend, A., Bertram, A., and Seinfeld, J. H. (2013). Gas-Particle Partitioning of Atmospheric Aerosols: Interplay of Physical State, Non-Ideal Mixing and Morphology. *Phys. Chem. Chem. Phys.,* 15(27):11441–11453.

Smith, M. L., Bertram, A., and Martin, S. (2012). Deliquescence, Efflorescence, and Phase Miscibility of Mixed Particles of Ammonium Sulfate and Isoprene-Derived Secondary Organic Material. *Atmos. Chem. Phys.,* 12(20):9613–9628.

Smith, M. L., Kuwata, M., and Martin, S. T. (2011). Secondary Organic Material Produced by the Dark Ozonolysis of α-Pinene Minimally Affects the Deliquescence and Efflorescence of Ammonium Sulfate. *Aerosol Sci. Technol.,* 45(2):244–261.

Smith, M. L., You, Y., Kuwata, M., Bertram, A. K., and Martin, S. T. (2013). Phase Transitions and Phase Miscibility of Mixed Particles of Ammonium Sulfate, Toluene-Derived Secondary Organic Material, and Water. *J. Phys. Chem. A*, 117(36):8895–8906.

Song, M., Liu, P. F., Hanna, S. J., Martin, S. T., and Bertram, A. K. (2015). Relative Humidity-Dependent Viscosities of Isoprene-Derived Secondary Organic Material and Atmospheric Implications for Isoprene-Dominant Forests. *Atmos. Chem. Phys. Discussions,* 15(1):1131–1169.

Song, M., Marcolli, C., Krieger, U. K., Zuend, A., and Peter, T. (2012). Liquid-Liquid Phase Separation and Morphology of Internally Mixed Dicarboxylic Acids/Ammonium Sulfate/Water Particles. *Atmos. Chem. Phys.,* 12 (5):2691–2712.

Tong, H.-J., Reid, J. P., Bones, D. L., Luo, B. P., and Krieger, U. K. (2011). Measurements of the Timescales for the Mass Transfer of Water in Glassy Aerosol at Low Relative Humidity and Ambient Temperature. *Atmos. Chem. Phys.,* 11(10):4739–4754.

Vaden, T. D., Imre, D., Beránek, J., Shrivastava, M., and Zelenyuk, A. (2011). Evaporation Kinetics and Phase of Laboratory and Ambient Secondary Organic Aerosol. *Proc. Natl. Acad. Sci.,* 108(6):2190–2195.

Virtanen, A., Joutsensaari, J., Koop, T., Kannosto, J., Yli-Pirilä, P., Leskinen, J., et al. (2010). An Amorphous Solid State of Biogenic Secondary Organic Aerosol Particles. *Nature,* 467(7317):824–827.

Virtanen, A., Kannosto, J., Arffman, A., Joutsensaari, J., Kuuluvainen, H., Saukko, E., et al. (2011). Bounce Behavior of Freshly Nucleated Secondary Organic Aerosol. *Atmos. Chem. Phys.,* 11:8759–8766.

You, Y., Smith, M. L., Song, M., Martin, S. T., and Bertram, A. K. (2014). Liquid–Liquid Phase Separation in Atmospherically Relevant Particles Consisting of Organic Species and Inorganic Salts. *Int. Rev. Phys. Chem.,* 33(1):43–77.

Zobrist, B., Soonsin, V., Luo, B. P., Krieger, U. K., Marcolli, C., Peter, T., et al. (2011). Ultra-Slow Water Diffusion in Aqueous Sucrose Glasses. *Phys. Chem. Chem. Phys.,* 13(8):3514–3526.

Tampereen teknillinen yliopisto
PL 527
33101 Tampere

Tampere University of Technology
P.O.B. 527
FI-33101 Tampere, Finland

ISBN 978-952-15-3544-4
ISSN 1459-2045